# JOURNAL OF CONDENSED MATTER NUCLEAR SCIENCE

## Experiments and Methods in Cold Fusion

**VOLUME 22, February 2017**

# JOURNAL OF CONDENSED MATTER NUCLEAR SCIENCE

Experiments and Methods in Cold Fusion

# JOURNAL OF CONDENSED MATTER NUCLEAR SCIENCE

## Volume 22, February 2017

**ISSN 2227-3123**



**Orders, claims, author inquiries and journal inquiries**

Please contact the Editor in Chief, CMNSEditor@iscmns.org or webmaster@iscmns.org

J. Condensed Matter Nucl. Sci. 22 (2017) 1–73
 ISSN 2227-3123


# JOURNAL OF CONDENSED MATTER NUCLEAR SCIENCE

Volume 22 2017

## CONTENTS

# Preface

This Volume 22 marks the tenth anniversary of the publication of the first volume of the *Journal of Condensed Matter Nuclear Science*. This journal was created to fill a void in the scientific world. Since the beginning, in 1989, the subject of Cold Fusion, discovered by Martin Fleischmann and Stanley Pons, has been, and is still, rejected by the scientific community. There was a need to go beyond the International Conferences on Cold Fusion proceedings to publish papers. It was necessary to have an internal way of communicating between scientists working together, just like in any other field of science. From the very start, it was decided that the journal would be peer reviewed. Also, since ICCF16, the Journal publishes the proceedings of the conferences and workshops dedicated to Condensed Matter Nuclear Science. A total of 312 papers have been published, 93 of them being conference proceedings.

I would like to thank all the anonymous referees those who have spent lot of time and effort to make the papers of high quality. I have been pleasantly surprised to find that some of them do such a great job in improving the papers, they almost deserve to be listed as co-authors! I would like to thank Jed Rothwell for the great work which he is doing to improve the quality of the English of papers written by non-English speaking authors. It is also a pleasure to thank our Indian colleague Dr. Kumar who is doing an excellent job in the typesetting of the papers.

Please enjoy in reading this new volume.

Sincerely,

*Dr. Jean-Paul Biberian*
( *Editor-in-Chief* )
*February 2017*

J. Condensed Matter Nucl. Sci. 22 (2017) 1–6

Research Article

# CR-39 Detector Track Characterization in Experiments with Pd/D Co-deposition

Andriy Savrasov* and Viktor Prokopenko
*Institute for nuclear research NAS of Ukraine, 47 Science ave., Kiev 03680, Ukraine*

Eugene Andreev
*Institute of physics NAS of Ukraine, 46 Science ave., Kiev 03680, Ukraine*

**Abstract**

Four experiments replicating the GALILEO Project were performed. In two of them, excess $\alpha$-particle track density was observed in the CR-39 detectors in comparison with background CR-39 detectors.
 ISSN 2227-3123

*Keywords:* $\alpha$-Particle, Co-deposition, CR-39 Detector, Electrolysis

## 1. Introduction

In LENR, the excess enthalpy production is followed in some cases by the generation of helium-4 [1] and neutrons [2]. However reliable replication of successful results has been a serious problem. In 2007 a group of researchers from San Diego [3] reported what they called the GALILEO project, in which they obtained anomalous tracks with a method they were able to replicate exactly.

The GALILEO project developers prepared for the experiment two cells made of plastic – one experimental and the other a control cell. The control cell was similar to the experimental cell in all characteristics, timing and processes with the sole exception that it used $CuCl_2$ instead of $PdCl_2$. The purpose of the controls was to show that the observed pitting was not due to chemical damage. In each cell electrolysis was conducted with 0.03 M $PdCl_2$ and 0.3 M LiCl solutions in heavy water with a platinum anode and Pd, Ag, Ni or Au cathodes. The CR-39 track detector was in contact with the cathode. In the process electrolysis current was gradually increased from 0.1 to 0.5 mA. The solution became completely transparent and all Pd accumulated on the cathode (plating phase) to (1–100 mA) – the charging phase. During the last phase the nuclear events (presumably) occur. After the charging phase was finished the CR-39 chips were taken from the solutions of both cells and were etched in etch solution (6.5 M NaOH in regular water) at

*E-mail: asavrasov@kinr.kiev.ua.

 ISSN 2227-3123

**Table 1.** Current quantity and duration during the experiments.

| | | | | | | | | |
|---|---|---|---|---|---|---|---|---|
| Experiment N1 | | | | | | | | |
| $I$(mA) | 0.3 | 1 | 5 | 10 | | | | |
| $t$ (h) | 15[a] | 10 | 14 | 17[b] | | | | |
| Experiment N2 | | | | | | | | |
| $I$ (mA) | 0.07 | 0.17 | 0.5 | 1 | 80 | 95 | 95 | |
| $t$ (h) | 11.5 | 2 | 15 | 6.5[c] | 2.5 | 4[d] | 6 | |
| Experiment N3 | | | | | | | | |
| $I$ (mA) | 0.05 | 0.1 | 0.15 | 0.05 | 3 | 10 | 30 | 90 |
| $t$ (h) | 26 | 18 | 24 | 65[e] | 22 | 24 | 24 | 10.5 |
| Experiment N4 | | | | | | | | |
| $I$ (mA) | 0.1 | 2 | 5 | 10 | 2.5 | 80 | 80 | 85 |
| $t$ (h) | 74.5 | 17[f] | 6 | 23 | 43 | 11[g] | 8[h] | 50 |

[a]Solution became completely transparent.
[b]Current decreased till 2.8 mA and did not increase any more. We have finished the experiment.
[c]Solution became completely transparent.
[d]Pause – 11 h.
[e]Solution became completely transparent.
[f]Solution became completely transparent.
[g]Pause – 64 h.
[h]Pause – 20 h.

a temperature of 68°C for 6 h. Next the track detectors were analyzed for the presence of pits similar to the tracks of alpha particles. There was a much higher number of tracks in the CR-39 chip in the experimental cell than in the control cell. The control cell CR-39 chip had approximately the same number of tracks as the background CR-39 chip. Additional verification was carried out after irradiation of the track detector by a source of alpha particles of known energy and intensity.

As of today only eight groups of researchers [4] in the world have tried to replicate the reported results and only a few of them have obtained positive results. These first results reported at the conference of four groups in March 2007 [5]. Other groups for various reasons have not been able to carry out the experiment. At the time of the conference there was a problem with the interpretation of tracks. Some believed that the tracks were due to the chemical damage caused by oxygen and chlorine or even corona discharge [6]. All the teams brought CR-39 detector outside the cell close to it (a dry experiment). After that pits were not observed in the detector, but that can be caused both lower energy of alpha particles and not taking into account water layers of varying thickness [7].

Based on what is described above, the purpose of this study was to replicate the GALILEO Project [3] in a wet configuration, which has the detector immersed in the cell and to obtain the $\alpha$-particles tracks using a silver cathode.

## 2. Materials and Methods

During electrolysis, one cell was used, and the cell with $CuCl_2$ solution was not used. Four experiments were done. In all the experiments the same $D_2O$, $PdCl_2$, LiCl substances and anodes were used.

The cell was made from Quartz glass (outer size 1.1 × 2.4 × 4 cm, inner size 0.5 × 1.8 × 3.7 cm, wall thickness 0.3 cm, volume 3.3 $cm^3$). We bought this cell from the vender of chemical reactants in Kiev, called "Isotope." Our assembled cell in experiment N1 was the same as in the GALILEO project (except for the size), which was shown in photo on page 16 of Ref. [3]. Heavy water, $PdCl_2$ and LiCl salts, silver and platinum wires were bought from the same vendor. The Ag cathode placed in the electrolyte in this experiment was 0.1 mm thick and 48 mm long, while the Pt anode in the experiment N1 and in all following ones was 0.3 mm thick and its length was 147 mm in this experiment only.

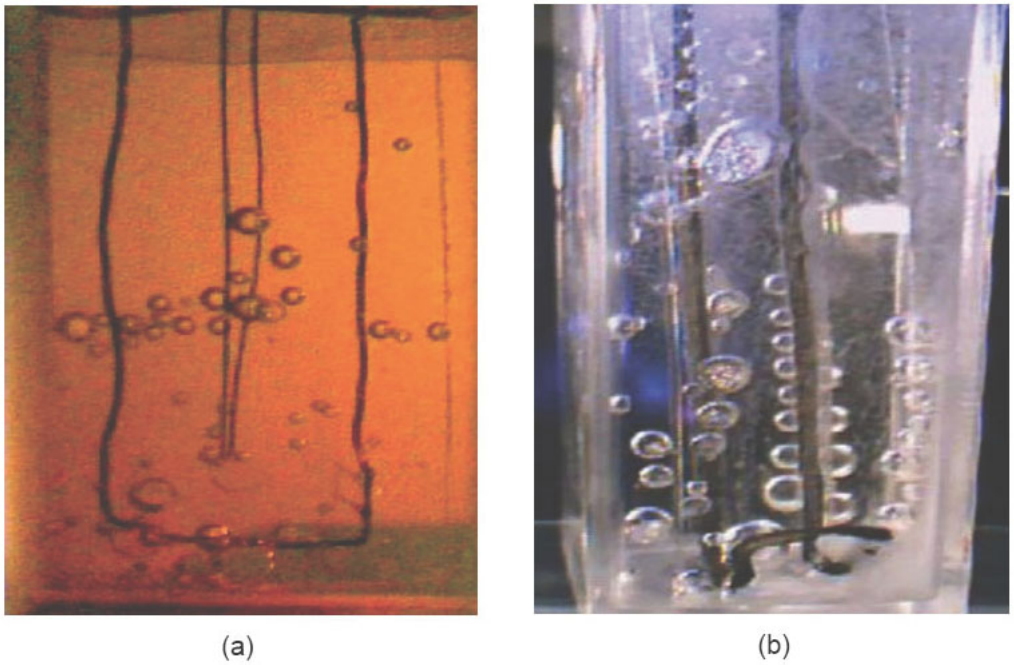


**Figure 1.** Photo of the cell with cathode and anode assembles which used in experiments N2, N3 (a) and N4 (b).

It is necessary to note that the initial current was 300 $\mu$A during experiment N1. At lower current the cell had a negative potential. As a result of the initial current being too high, the plating was done non-uniformly on the surface of the cathode. The maximum current was only 10 mA (see Table 1), current density was $J = 80$ mA/cm$^2$, cathode area = 0.125 cm$^2$ in experiment N1 and it did not increase any more. These circumstances became the possible reason for the insignificant number of excess tracks in the CR-39 chip in the solution in experiment N1, compared to the number of tracks in the background chip.

In experiments N2 and N3 cathode and anode assembles were used in which both the shapes and a spatial arrangement differed from ones described in Galileo protocol [3] (see Fig. 1(a)).

In these experiments the polyethylene base was absent. Both the cathode and anode were mounted on the same CR-39 chip. In the chip openings were bored through and a silver wire (diameter – 0.1 mm, length – 42 mm) passed through them (in Fig. 1(a) this wire is more thin and is located in the middle of the CR-39 chip). Platinum anode (length – 62 mm) also was passed through the additional openings made in CR-39 and folded around the cathode from three sides (on the left, on the right and from below as shown in Fig. 1(a)). In experiments N2 and N3 both the anode and cathode were located on one plane.

In experiment N4 the cathode with a bigger diameter ($d = 0.3$ mm, length – 72 mm) was used (see Fig. 1(b)), which was fastened on the CR-39 chip. The anode was mounted from the cell opposite side in the form of a wire with length 31 mm (see Fig. 1(b)). In this experiment both cathode and anode were located in different planes, as opposed to the experiments N2 and N3. We used 15 mg of $PdCl_2$ and 36 mg of LiCl on 2.8 ml of heavy water and this solution was poured in our cell. We added heavy water to the cell during the experiments. On average we added nearly 1.5 ml of heavy water per experiment.

The CR-39 track detectors were fabricated in the Radium institute of V.G. Hlopina. They were wrapped in a polyethylene film the entire time, and stored in the freezer chamber of a refrigerator. The thickness of the CR-39 chips is 300 $\mu$m and the velocity of etching – 1 $\mu$m/h. Dimensions of the track detectors were in the first experiment (Height $\times$ width) – 1.5 $\times$ 1.0 cm, in the second and third ones – 3.3 $\times$ 1.5 cm, and in the fourth experiment – 3.6 $\times$ 0.8 cm.

We made a custom-built current source with power 3 W, made from the following components: transistor KP931A (range of values of a direct current on the exit: 20 $\mu$A – 95 mA) and transformer, which is switched in the alternating current network with $U = 220$ V (range of values of a direct voltage on an exit: 0–40 V). The resistance of the source on the exit is $R \geq 1$ M$\Omega$.

When the experiments were terminated, the cell was disassembled and the CR-39 detectors were etched in an aqueous 6 M sodium hydroxide solution at 68–70°C for 7.5 h. Microscopic examination of the etched CR-39 detectors was done using an MTKF-1 microscope.

## 3. Results and Discussion

After etching, the number of excess tracks on the CR-39 detectors placed in electrolytic cell was compared to the CR-39 blanks. Extra tracks were observed in experiments N1 and N4. We used blank detectors which were exposed for a week in the room in air near the experimental cell. The calculation of the number of pits was made by manual procedures with the consecutive passage of the frames by MTKF-1 microscope. In experiment N1 on CR-39 in a cell, the track density 167 tr cm$^{-2}$ was measured (blanks 97 tr cm$^{-2}$), and in experiment N4 – 545 tr cm$^{-2}$ (back side – 292 tr cm$^{-2}$).

We could best satisfy the condition of the GALILEO Project [3] only in experiment N4. We have carefully analyzed this recent experiment.

Figure 2(a) and (b) shows two images taken at two different focal depths, at the surface (Fig. 2(a)) and bottom of the tracks (Fig. 2(b)) of the same CR-39 detector. This sample was in the electrolytic cell during experiment N4. To determine whether the pits are due to energetic particles or to chemical damage, we compared the pits obtained from the Pd/D co-deposition experiment with those obtained when CR-39 was exposed to an alpha particle source [8]. The CR-39 detector was irradiated by $^{238}$Pu, 35 kBk activity for 3 s. The $^{238}$Pu nuclei decay on $^{234}$U irradiating alpha particles with the following energy (intensity): 5.499 MeV (70.9%), 5.456 MeV (29.0%), 5.358 MeV (0.1%). Tracks are created by $\alpha$-particles have the conic form. Figures 2(c) and (d) show two images taken at two different focal depths (surface (Fig. 2(c)) and bottom of the tracks (Fig. 2(d))) of the same CR-39 detector, which was irradiated by the $\alpha$-particles. We used the microscope Axioscop 2 MAT mot (Carl Zeiss, Germany) with the digital chamber AxioCam MRc Rev 2 at high resolution to photograph the CR-39 chips shown in Fig. 2. This microscope is located in the diagnostic centre for collective use at V. Lashkaryov Institute of Semiconductor Physics of NAS of Ukraine.

These tracks have a round form and dark color. When the microscope is focused more deeply in CR-39 than in the track centre a bright spot is observed (see Fig. 2(d)). This is caused by the bottom part of a conic track. The tracks also have beautiful optical contrast range. These signs: the optical contrast range, the form and the bright spot in the track centre are important factors which help to distinguish the present $\alpha$-particle tracks from chemical damage. By comparing Fig. 2(a) and (b) with Fig. 2(c) and (d) which are the $\alpha$-particles tracks after $^{238}$Pu decay it is possible to see that they are similar, but the track diameters of the $\alpha$-particles are twice as large, as shown in Fig. 2(a) and (b). We do not have the calibration curve for a given CR-39 detector type, nevertheless the increase in diameter can be caused by both the longer etching times (7.5 h in comparison with 6 h for the CR-39 detector irradiated by $\alpha$-particles from $^{238}$Pu source), and possible smaller value of $\alpha$-particle residual energy which are generated in the solution.

The photomicrographs were obtained using a magnification of 640$\times$.

On the entire surface of the CR-39 detector which was in the cell, the pits are distributed nonhomogeneously in area

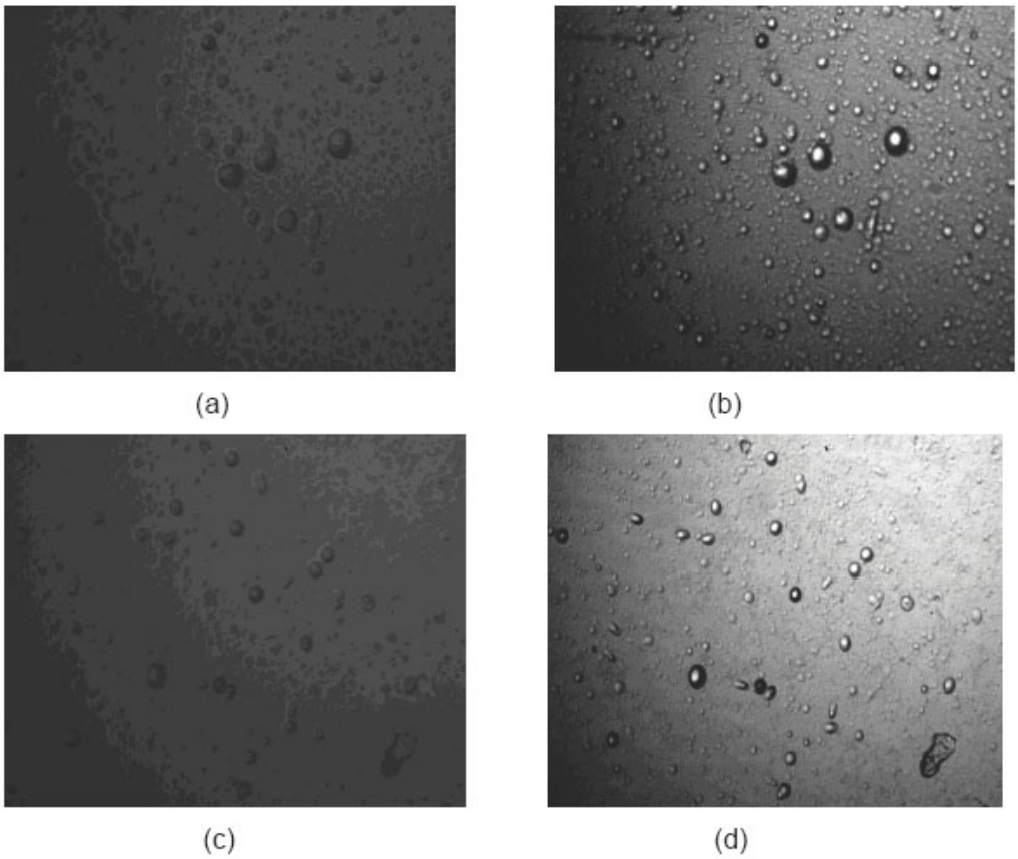


**Figure 2.** Images of pits in the CR-39 detector surface (Fig. 2(a)), and bottom (Fig. 2(b)) taken at two different focal depths of the same CR-39 detector. This sample was in electrolytic cell during experiment N4. The similar images created by exposure to $^{238}$Pu source (Fig. 2(c) and (d) using a magnification of 640×.

extent. Figure 3 shows the spatial distribution of the pits along the CR-39 surface. The count on the axis of abscises is measured from the upper part of the CR-39 detector to the depth of the cell. The thickness of the row is 0.22 mm. The quantity of pits increases in the lower part of the CR-39 detector, but they are distributed regularly along the surface. There is no higher concentration of the pits near the cathode.

Unsuccessful experiments N2 and N3 prove that pits formed during Pd/D co-deposition are not due to radioactive contamination of substances used in the experiments nor are they caused by impingement of gas bubbles on the surface of the CR-39, nor by chemical reactions of the surface of CR-39 with $D_2$, $O_2$ or $Cl_2$ present in electrolyte. The maximum current in experiment N4 was 85 mA, and its density $J = 220$ mA/cm$^2$.

Based on the evidence presented above, it is possible to draw the following conclusions:

(1) The tracks on the CR-39 detector which were observed at their arrangement in electrolytic cells during experiments N1 and N4 had a nuclear origin.
(2) The source of the charged particles was in the solution volume adjacent to the CR-39 detector, and correlates

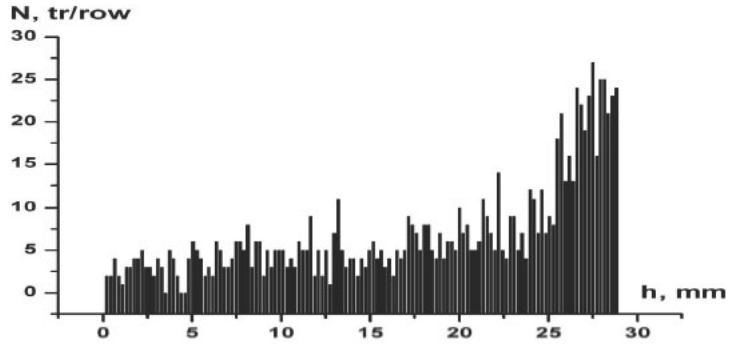


**Figure 3.** Pits quantity on the row (N) in comparison with the depth of the immersion of CR-39 – detector in the solution (h).

with the Pd deposit.

## References

[1] B.F. Bush, J.J. Lagowski, M.M. Miles and G.S. Ostrom, Helium production during the electrolysis of $D_2O$ in cold fusion experiments, *J. Electroanal. Chem.* **304** (1991) 271–278.

[2] A. Battaglia, L. Daddi, S. Focardi, V. Gabbani, V. Montalbano, F. Piantelli, P.G. Sona and S. Veronesi, Neutron emission in Ni–H systems, *IL. Nuovo Cimento.* 112 (9) (1999) 921–931.

[3] S. Szpak, P. Mosier-Boss and P. Gordon, The Galileo Project – Phase 1, 2007.
Available from http://newenergytimes.com/v2/projects/tgp/2007TGP/2007GalileoProjectReport.pdf.

[4] S.B. Krivit, Galileo Project Report, 2007. Available from http://newenergytimes.com/projects/tgp/2007TGP/2007TGP-Report.shtml

[5] APS Mitting March 5, 2007, Colorado Convention Center.

[6] P.A. Mosier-Boss, S. Szpak, F.E. Gordon and L.P.G. Forsley, Reply to comment on the use of CR-39 in Pd/D co-deposition experiments: a response to Kowalski, *Euro. Phys. J. Appl. Phys.* **44** (2008) 291–295.

[7] P.A. Mosier-Boss, S. Szpak, F.E. Gordon and L.P.G. Forsley, Characterization of tracks in CR-39 detectors obtained as a result of Pd/D co-deposition, *Euor. Phys. J. Appl. Phys.* **46** (2009) 30901.

[8] P.A. Mosier-Boss, S. Szpak, F.E. Gordon and L.P.G. Forsley, Use of CR-39 in Pd/D co-deposition experiments, *Euro. Phys. J. Appl. Phys.* **40** (2007) 293–303.

J. Condensed Matter Nucl. Sci. 22 (2017) 7–26

Research Article

# Basic Design Considerations for Industrial LENR Reactors

Jacques Ruer*

**Abstract**

LENR reactors able to deliver heat at a high temperature can be coupled with heat engines to generate electric power. The conditions of temperature and COP to achieve self-sustaining operation are given. According to the literature, the heat generation rate of some LENR processes increases rapidly with the temperature. This phenomenon dictates the cooling criteria to maintain a stable reactor operation. Power control can be obtained through appropriate temperature regulation. Several types of heat engines can be coupled to LENR reactors with appropriate power control. Heat losses must be minimized with sufficient thermal insulation. The insulation enclosure is also useful to recover the leaks of light gas, if any are present in the system.
 ISSN 2227-3123

*Keywords:* Gas leakage, Heat engines, Power control, Runaway, Self-sustaining, Stability, Thermal insulation

## 1. Introduction

Even if it is presently difficult to predict a precise timeframe, it can now be reasonably predicted that LENR reactors will one day produce a sizeable source of power [1]. We focus in this paper on the particular class of LENR systems that produce excess heat at a temperature level sufficient to envisage the conversion of the heat into mechanical and electrical energy.

Future progress in the field will form the basis of the technology applied for industrialization. Although it is not yet possible to describe the precise technology that will be utilized, some features that must be integrated in future reactors can already be listed:

- Unless the reactor directly transforms the LENR phenomena into electricity, the reactors will produce heat that will be converted into power via conventional heat engines.
- Because heat engines can only work with heat sources at a temperature above ambient, LENR reactors will preferably operate at high temperature levels.
- LENR reactors require some form of excitation (in general in an electrical form), at least for the start-up phase. It is assumed here that the generation of LENR energy can be controlled to some extent via the regulation of the excitation input.
- It has now been reported by several authors that the energy generation increases with the temperature. The design of the reactor must take this positive feedback into account.

*E-mail: jsr.ruer@orange.fr.

 ISSN 2227-3123

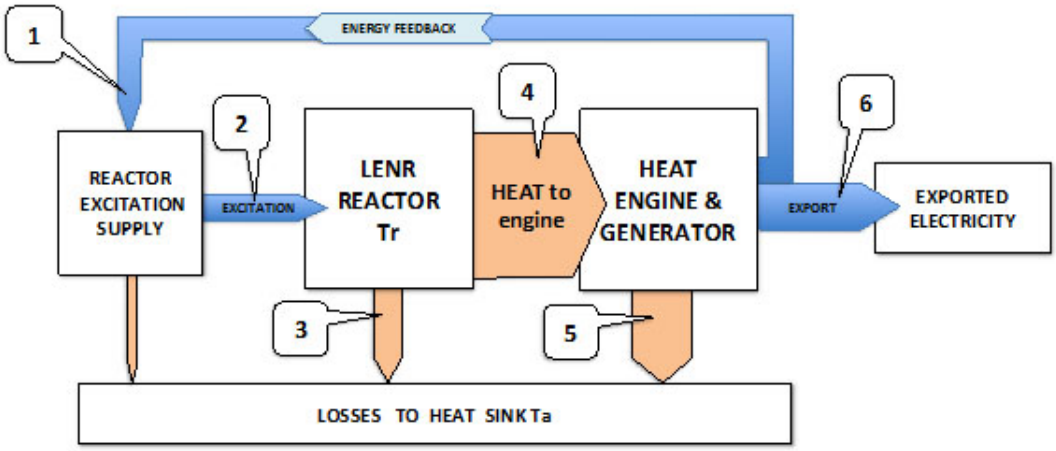


**Figure 1.** Schematic diagram of an LENR generator including a reactor coupled with a heat engine. Electrical energies (power) are shown in blue, heat fluxes in orange. The sketch shows the following inputs/outputs. 1: Power input to the excitation supply, $E_0$. 2: Excitation input to the reactor, $E_1 = \alpha E_0$ ($\alpha < 1$). 3: Reactor heat loss: $H_1$. 4: Heat input to the engine at temperature $T_r$: $H_2$. 5: Heat rejected by the engine at temperature $T_a$, $H_3$. 6: Electricity exported, $E_2$. Note that the engine produces the electrical power $E_{out} = E + E_2$

.

This paper is a discussion of the above points.

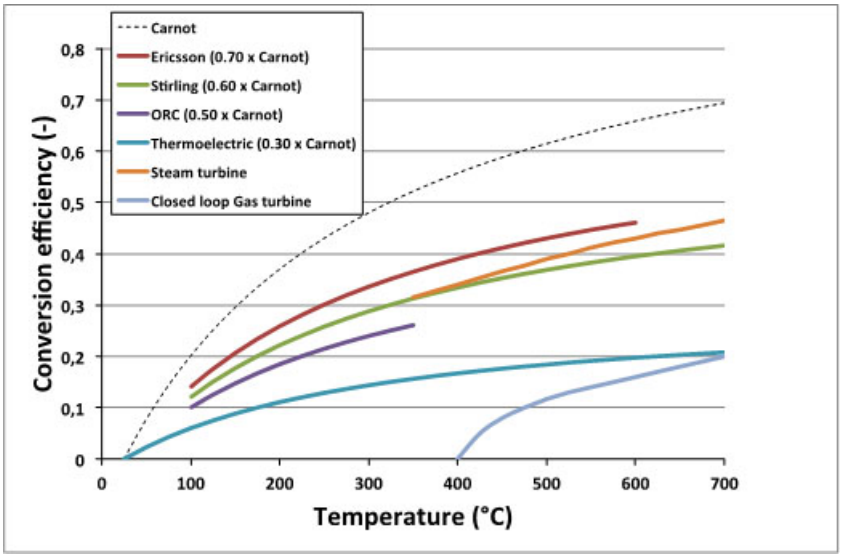


**Figure 2.** Relationship between the temperature of the heat source ($T_{hot}$) and the typical efficiency of various thermal engines, $T_{cold} = 25°C$. Compilation of various data by the author.

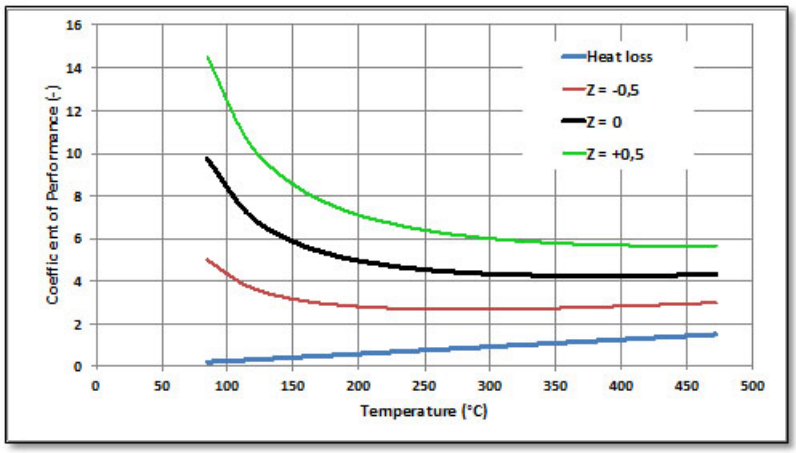


**Figure 3.** Relationship between the temperature and the COP for different $Z$ values, $\eta_{\mathrm{m}} = 0.7$, $f = 1$, $T_{\mathrm{cold}} = 25°\mathrm{C}$.

## 2. Self-sustaining Operation

An LENR reactor consumes some energy to sustain its operation. If the quantity of electricity produced by the generator exceeds the need of the power supply, there is a surplus of electricity that can be exported. This is the definition of autonomous or self-sustaining operation. The parameters required to make such an operation possible are presented in [2] and reproduced here.

Different types of heat engines have been developed [3]. The thermodynamics teaches that such engines must take heat ($H_{\mathrm{in}}$) from a source at a high temperature ($T_{\mathrm{hot}}$) and reject a fraction to a heat sink at a lower temperature ($T_{\mathrm{cold}}$) [4]. They are characterized by their efficiency:

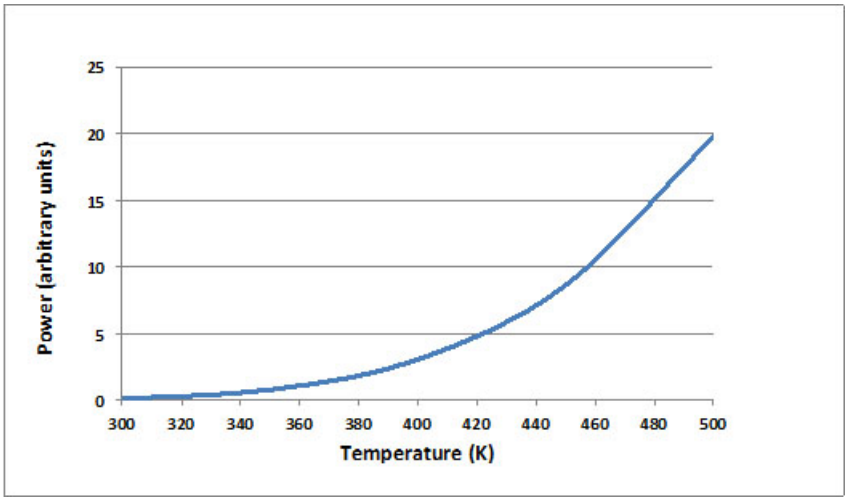


**Figure 4.** Plot of Eq. (16) between 300 and 500 K. The power is given in arbitrary units.

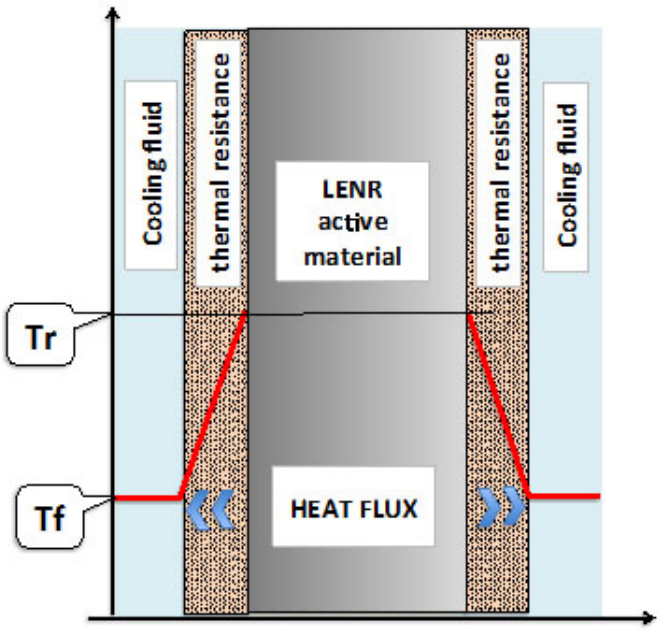


**Figure 5.** Schematic temperature profile of an LENR reactor separated from the cooling medium by a heat resistance layer.

$$\eta = E_{\text{out}}/H_{\text{in}}. \tag{1}$$

The efficiency is limited by the Carnot formula:

$$\eta_{\text{c}} = 1 - T_{\text{cold}}/T_{\text{hot}}. \tag{2}$$

The engines are not perfect, so that the effective efficiency is lower than the theoretical one:

$$\eta = \eta_{\text{c}}\,\eta_{\text{m}}, \tag{3}$$

where $\eta_{\text{m}}$ is the relative machine efficiency.

The machine efficiency includes all losses, e.g. the energy lost during the transformation of the mechanical energy into electricity, or the energy required to drive ancillary components like pumps, fans, control system, etc. Figure 2 shows the typical efficiencies attained by different types of thermal engines.

These equations can be utilized to determine the coefficient of performance (COP) required from the LENR reactor to obtain a self-sustained operation. The nomenclature of the energy fluxes is listed in Fig. 1. We write:

$$E_1 = \alpha E_0, \tag{4}$$

$$\lambda = T_{\text{r}}/T_{\text{a}}. \tag{5}$$

The heat loss $H_1$ is written as a ratio of $E$ using a dimensionless heat loss factor $f$:

$$H_1 = f\,(\lambda - 1)\,E_0. \tag{6}$$

The efficiency is

$$\eta = \eta_{\rm m}(\lambda - 1)/\lambda. \tag{7}$$

The electrical power produced by the engine is

$$E_{\rm out} = E_0 + E_2 = \eta H_2. \tag{8}$$

We introduce the energy gain $Z$ defined by

$$Z = \frac{E_{\rm out}}{E_0} - 1 = \frac{E_2}{E_0}. \tag{9}$$

A self-sustained operation is characterized by $Z > 0$

$$E_{\rm out} = E_0 + E_2 = (1 + Z)E_0 = \eta H_2, \tag{10}$$

$$H_2 = (1 + Z)E_0/\eta, \tag{11}$$

$$\text{COP}\,\alpha E_0 = H_1 + H_2, \tag{12}$$

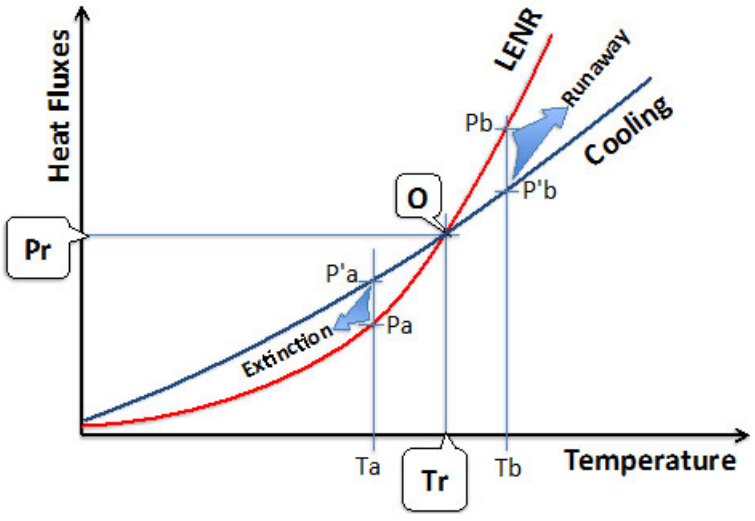


**Figure 6.** Cooling of an LENR reactor across a heat resistance. Any deviation of the temperature develops an instability.

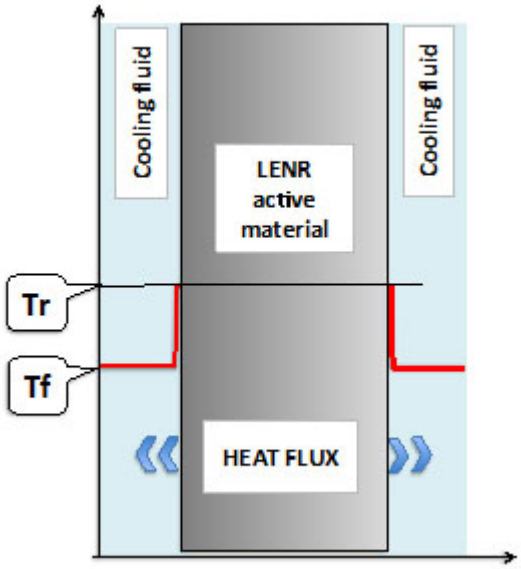


**Figure 7.** Cooling of an LENR reactor by a convective fluid flow. The temperature profile exhibits a pinch $T_r - T_f$ on the surface.

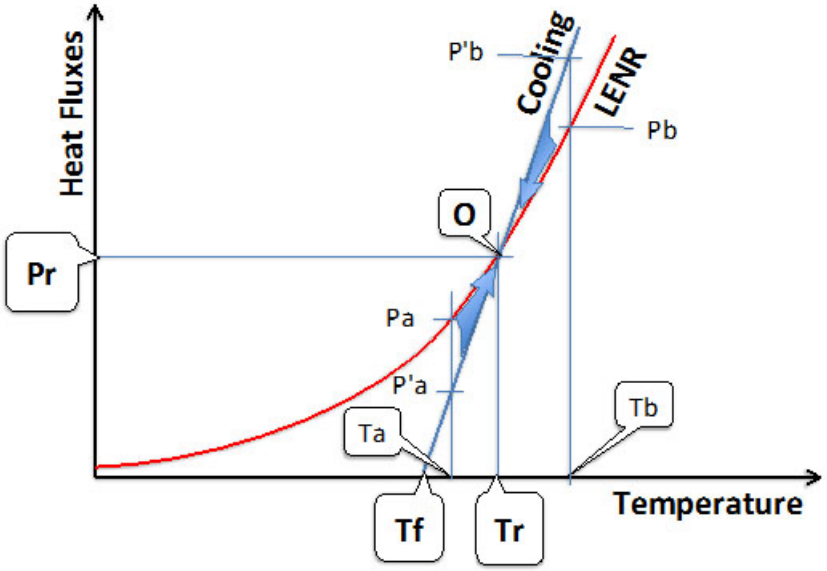


**Figure 8.** Cooling of an LENR reactor by a convective fluid flow. Any deviation of temperature is compensated by the system, the operation is stable.

$$\text{COP}\,\alpha E_0 = f(\lambda - 1)E_0 + (1 + Z)E_0/\eta. \tag{13}$$

This yields

$$\text{COP} = \frac{f(\lambda - 1)}{\alpha} + \frac{(1 + Z)\,\lambda}{\alpha\eta_{\text{m}}(\lambda - 1)}. \tag{14}$$

Equation (14) allows the calculation of the COP required for a given heat loss factor and a desired $Z$ value. Figure 3 presents an example of results for an arbitrary set of parameters.

Figure 3 shows that the reactor temperature is a very important parameter to obtain self-sustaining operation. It also shows that the heat loss through the insulation is obviously a detrimental factor that must be controlled as much as possible.

## 3. Reactor Stability

### 3.1. Influence of the temperature

Several authors report that the LENR power measured in the experiments increases with the temperature [5–8].

Arrhenius' theory teaches that the rate of a process, for instance heat-producing reactions, is a function of an activation energy $E$ and the fuel temperature $T$ [9].

$$W = A\text{e}^{-E/kT}, \tag{15}$$

where $W$ is the heat-production power, $A$, the pre-exponential factor, $E$, the activation energy, $k$, the Boltzmann's constant, and $T$ the absolute temperature of the reactive medium.

If an experiment performed at different temperatures $T_1$ and $T_2$ yields the heat power levels $W_1$ and $W_2$, the above equation makes it possible to determine the activation energy:

$$\log(W_1) = \log(A) - \frac{E}{kT_1}, \tag{16}$$

$$\log(W_2) = \log(A) - \frac{E}{kT_2}, \tag{17}$$

$$\log(W_1/W_2) = \frac{E}{k}\left(\frac{1}{T_2} - \frac{1}{T_1}\right), \tag{18}$$

$$E = k\log(W_1/W_2)\,\frac{T_1T_2}{T_1 - T_2}. \tag{19}$$

In a recent paper [8], Storms reports a heat power curve well approximated by the equation:

$$\log W = 4.54 - 1621/T. \tag{20}$$

The corresponding activation energy is 1.8 kJ/mol. This value is close to the activation energy for deuterium diffusion in the lattice (1.9 kJ/mol). According to Storms, it is an indication that the role of the temperature is related to its influence on the hydrogen diffusion coefficient.

Equation (20) is equivalent to

$$W = 34\,600\,\text{e}^{-3732/T}. \tag{21}$$

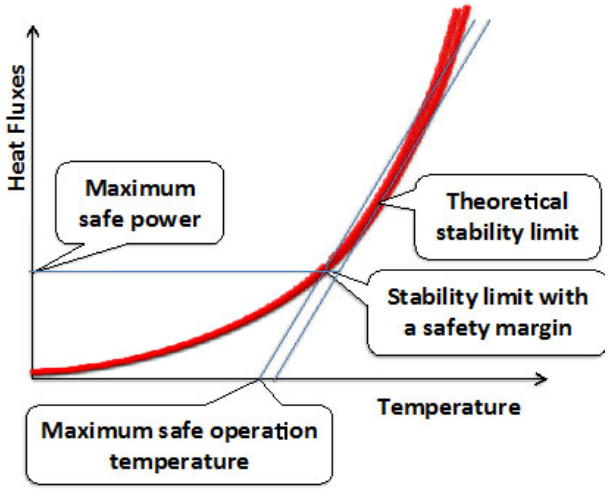


**Figure 9.** Schematic evaluation of the safe power limit. The LENR heat output involves bursts and fluctuations that must be taken into account to determine the safe conditions of operation.

Figure 4 shows the corresponding curve for temperatures up to 500 K, although this is beyond the actual experiments presented in [8].

The influence of the temperature must be taken into account in the design of the future reactors for the reasons that are discussed in the following.

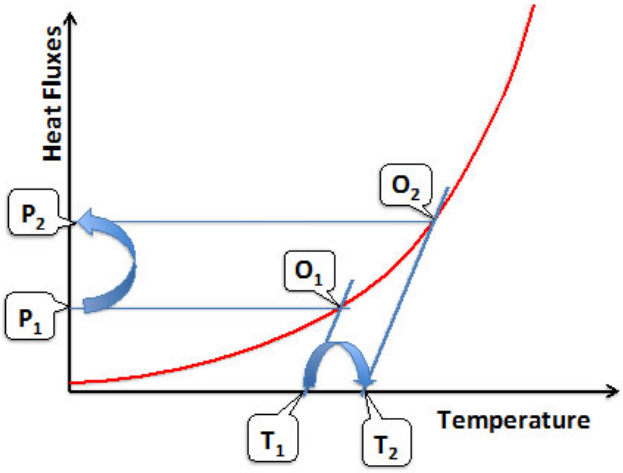


**Figure 10.** Power control increase. The fluid temperature is increased from $T_1$ to $T_2$. The power is raised from $P_1$ to $P_2$.

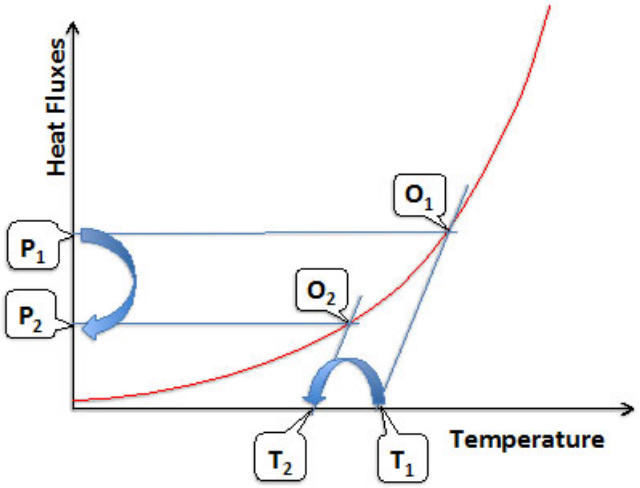


**Figure 11.** Power control decrease. The fluid temperature is decreased from $T_1$ to $T_2$. The power is reduced from $P_1$ to $P_2$.

### 3.2. Thermal stability

Let us first consider Fig. 5. The reactor is separated from the cooling fluid by a thermal resistance layer. This configuration is found in many experimental setups. The heat flux is basically proportional to the difference between the reactor temperature $T_\mathrm{r}$ and the fluid temperature $T_\mathrm{f}$.

Figure 6 compares the relationships between the temperature, the heat flux to the cooling fluid and the LENR heat output The theoretical operating point is located at point O, intersection of the two curves. The temperature at the interface of the reactive material and the resistance layer is $T_\mathrm{r}$, the heat power of the reactor is $P_\mathrm{r}$. If the temperature for any reason is changed to $T_\mathrm{a} < T_\mathrm{r}$, the LENR power decreases to $P_\mathrm{a}$, while the cooling heat exchange becomes $P'_\mathrm{a}$. Figure 6 shows that $P_\mathrm{a} < P'_\mathrm{a}$. This means that in such a case, the temperature can only drop further. The reaction slows down and the reactor stops.

Conversely, if the temperature is higher than $T_\mathrm{r}$, the LENR power $P_\mathrm{b}$ is larger than the cooling capacity $P'_\mathrm{b}$. The temperature increases continuously. The reactor goes out of control. Cooling the reactor through a heat resistance layer leads therefore to an unstable configuration. The occurrence of an LENR excess heat may easily result in a runaway reaction.

Another configuration is shown in Fig. 7. The reactor is directly cooled by the fluid with a bulk temperature of $T_\mathrm{f}$. The heat exchange between the reactor and the fluid can be described by the equation:

$$P_\mathrm{cooling} = h\ (T_\mathrm{r} - T_\mathrm{f})\,, \tag{22}$$

where $h$ is the heat exchange coefficient, measured in $\mathrm{W\,m^{-2}K^{-1}}$.

The superposition of the LENR power curve and a cooling curve according to Eq. (22) is shown in Fig. 8. It is supposed that $T_\mathrm{f}$ and the heat exchange coefficient $h$ are such that the cooling curve intersects the power curve at point O. If the temperature becomes $T_\mathrm{a} < T_\mathrm{r}$, the power $P_\mathrm{a}$ exceeds the cooling flux $P'_\mathrm{a}$, so that the reactor returns to the operating point. Inversely, if the temperature is higher than $T_\mathrm{r}$, the cooling exceeds the LENR power, and the temperature returns to $T_\mathrm{r}$. We see that the intersection point O is stable.

The configuration shown in Fig. 7 allows stable operation. The reactor heat must be evacuated by a flow of fluid organized in order to achieve a satisfactory exchange coefficient. The condition to be satisfied is given by the

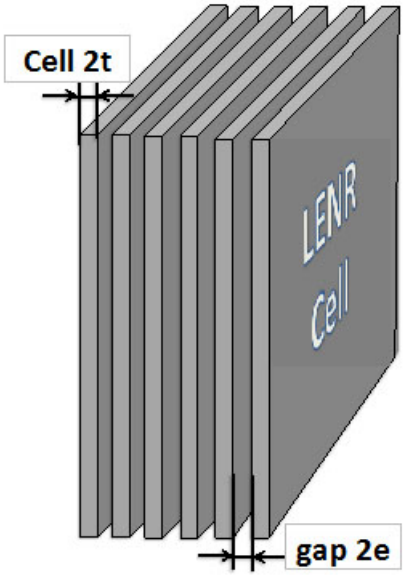


**Figure 12.** Schematic layout of an hypothetical LENR reactor. The thickness of the LENR cells is 2*t*. The cells are separated by gaps filled by the cooling fluid. Gap thickness is 2*e*.

relationship between the heat exchange coefficient and the slope of the power curve as given by the derivative of the power curve equation:

$$h > \mathrm{d}P_{\mathrm{LENR}}/\mathrm{d}T. \tag{23}$$

This condition must be obeyed in the system at any moment and any location. In fact, it is known that LENR sometimes occur as local bursts of heat. The LENR power curve drawn in the above figure is therefore a simplification of the actual phenomena. Figure 9 presents a more realistic picture. The power curve is blurred, to illustrate that the local heat flux fluctuates even for a given temperature. In order to avoid instability, it is advisable to control the fluid temperature and the power under safe limits.

### 3.3. Control of the reactor power

The power of LENR reactors can be controlled to some extent via the excitation energy input. However, some LENR devices produce heat after death, meaning that the reaction proceeds even in the absence of excitation [5,6]. In such cases, it is necessary to develop another method to control the energy output. The sensitivity of LENR to the temperature can advantageously provide this additional mode of power control.

Figure 10 illustrates an LENR power curve and two different cooling lines. Let us suppose that the reactor is initially operated at point $\mathrm{O}_1$. The cooling fluid temperature is then $T_1$. Now, let us slightly increase the fluid temperature. The reactor temperature increases. The power rises to $P_2$. This can be easily obtained via a temporary decrease of the fluid flow rate. This can also be accomplished by an external reheating of the fluid, especially during the startup phase, when the whole reactor system must be warmed up. This mode of control is called Power Control Increase or PCI.

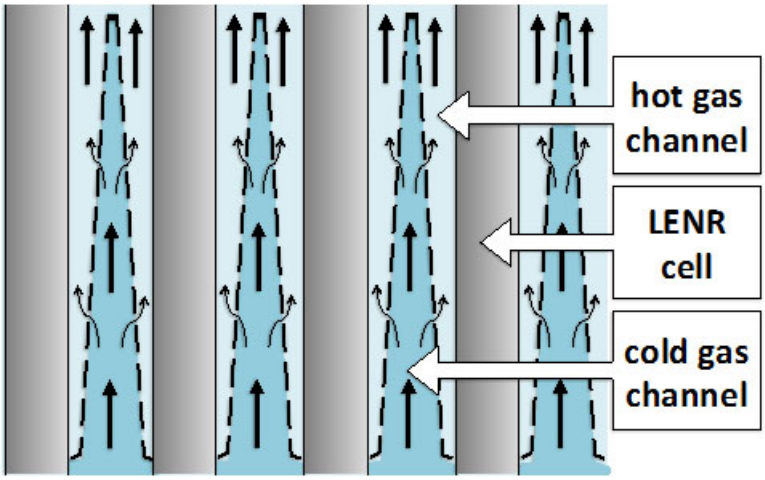


**Figure 13.** Schematic LENR reactor with gas cooling. The gas is distributed to obtain an uniform temperature $T_f$ all over the surface of the cells.

Similarly, the power can be reduced at will. Figure 11 shows that if the fluid temperature is lowered from $T_1$ to $T_2$, the reactor power is decreased from $P_1$ to $P_2$. This can be obtained via an additional cooling of the fluid before it enters the reactor. This mode of control is called Power Control Decrease or PCD.

If it is desired to stop the reactor, it is possible to quench it by circulating cold fluid for a sufficient time.

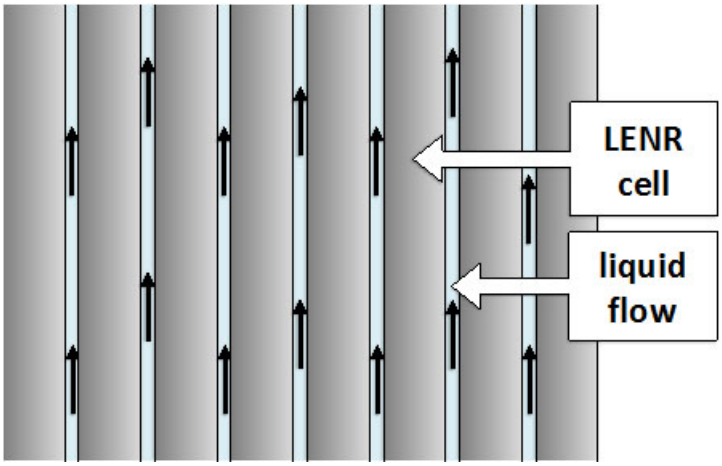


**Figure 14.** Schematic arrangement of an LENR reactor cooled by a forced flow of liquid (oil, molten salt or liquid metal) between the cells.

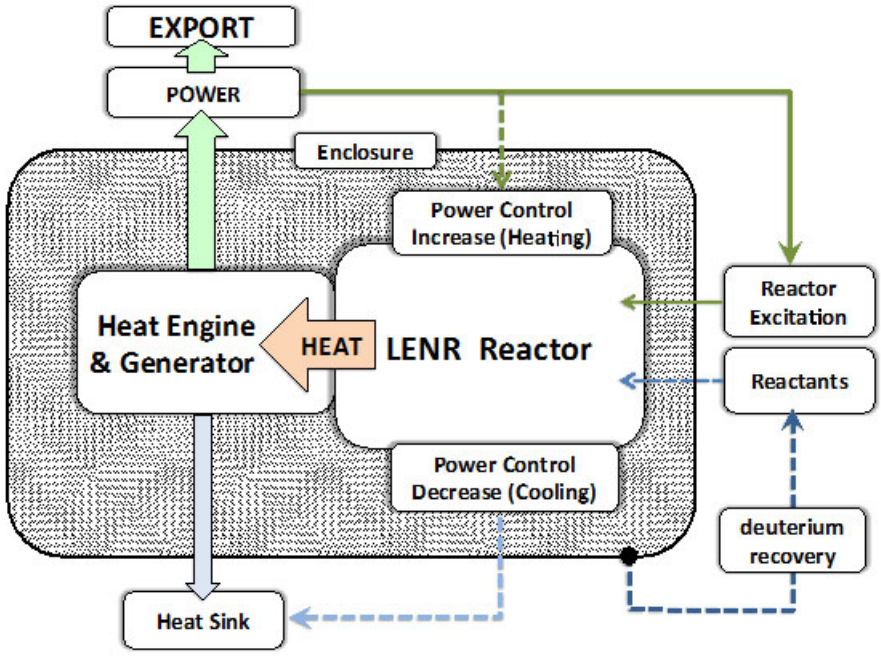


**Figure 15.** Schematic block diagram of an LENR power generator.

## 4. Potential Design of LENR Generators

### 4.1. Basic cooling methods

The above discussion leads to the basic design of an industrial LENR reactor. The LENR reactor must be cooled so that the criteria of Eq. (23) is satisfied. The cooling fluid (gas or liquid) is hot, at a temperature slightly below $T_r$. To

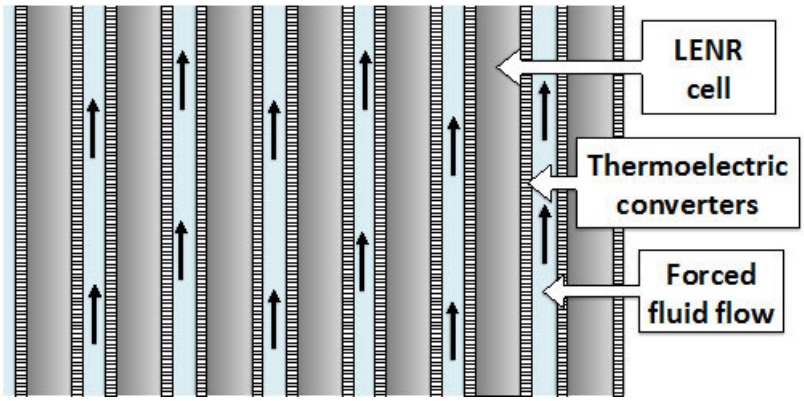


**Figure 16.** Schematic configuration of an LENR reactor with thermoelectric converters (TEC). The TEC elements are intercalated between the LENR cells and the cooling fluid.

make the heat flow out of the LENR active material possible, this material is confined in multiple cells. The shape of the cells is prismatic, planar or tubular. The gap between adjacent cells is filled by the forced flow of cooling fluid. The sizing of the cell thickness is governed by the heat flow capacity across the active material, and by the heat flux exchanged with the fluid.

In order to clarify the above, let us consider a theoretical example (see Fig. 12). We imagine a hypothetical LENR system characterized by a power density of 1 W cm $^{-3}$, or 1 MW m $^{-3}$. The supposed operating temperature is 600°C or 873 K. The LENR cells are square slabs 1 m $\times$ 1 m with a thickness $2t = 20$ mm. They are cooled on both sides, and the heat flux on each face is 10 kW. The fluid circulates in the gaps between adjacent cells upwards along the whole height. Two different cases are examined in Table 1, cooling by a forced gas flow and a forced flow of liquid.

**Table 1.** Comparison of the cooling of an hypothetical LENR reactor by a gas or a liquid.

| | Gas cooling | Liquid cooling |
|---|---|---|
| Heat flux at interface | $10^4$ W m$^{-2}$ | $10^4$ W m$^{-2}$ |
| Typical fluid heat capacity | $10^3$ J N m$^{-3}$K$^{-1}$ | $10^6$ J m$^{-3}$K$^{-1}$ |
| Fluid flow rate | 0.1 N m$^3$s$^{-1}$ (atmospheric pressure) | $10^{-3}$ m$^3$s$^{-1}$ |
| Gap thickness: $2e$ | 20 mm | 5 mm |
| Fluid velocity | 32 m s$^{-1}$(atmospheric pressure) | 0.4 m s$^{-1}$ |
| Typical exchange coefficient (9) | $10^2$ W m$^{-2}$K$^{-1}$ | $10^3$ W m$^{-2}$K$^{-1}$ |
| Delta $T$ solid–fluid | 100 K | 10 K |
| Temperature inlet | 400°C | 580°C |
| Temperature outlet | 500°C | 590°C |

In the case of gas cooling, the temperature difference adopted between the gas inlet and the gas outlet is 100 K. A typical gas heat capacity is 103 J N m$^{-3}$K$^{-1}$. The evacuation of the heat requires a flow of 0.1 N m$^3$s$^{-1}$. We suppose that the gap thickness is 20 mm. If the pressure is atmospheric, the gas velocity is 32 m s$^{-1}$. This is acceptable. However, the velocity is lower if a higher pressure is used. The heat exchange coefficient *h* between the cell and a gas flow is typically 100 W m$^{-2}$K$^{-1}$ [10]. The gas enters at 400°C and leaves at 500°C. The engine performance must take these values into account, rather than $T_{\mathrm{r}}$. Figure 13 presents a potential configuration with gas cooling. Because the LENR power is sensitive to the temperature, the gas circulation is organized to obtain a progressive mixing of the cold and the hot gas, so that the value of $T_{\mathrm{f}}$ remains constant over the whole cells surface.

In the case of liquid cooling, the temperature difference adopted between the liquid inlet and outlet is 10 K. A typical heat capacity for a liquid medium is 106 J m$^{-3}$K$^{-1}$. The evacuation of the heat requires a flow of 103 m$^3$s$^{-1}$, or 1 l.s$^{-1}$. We suppose that the gap thickness is 5 mm. The velocity of the liquid in the gap is 0.4 m s$^{-1}$.

The heat exchange coefficient h between the cell and a forced flow of liquid is typically 103 W m$^{-2}$K$^{-1}$ [9]. The temperature difference according to Eq. (22) is then 1 K. The liquid enters at 580°C and leaves at 590°C. These values are very close to $T_{\mathrm{r}}$. Figure 14 presents a potential configuration with cooling by a liquid fluid. A simple film flow is suitable. The fluid flow rate is low and a narrow gap is sufficient. Another option is to immerse the cells in a boiling liquid. Heat exchange between a hot surface and a boiling fluid is very high [10]. This type of cooling is, for example, adopted in nuclear boiling water reactors (BWR). Boiling cooling may represent the best option for reactors with a large LENR power density.

### 4.2. LENR generators generic configuration

Figure 15 presents a schematic block diagram of a complete LENR power generator. The LENR reactor is linked to an excitation system and a supply of reactants. The heat is transferred to a heat engine by direct contact or via a circulating loop of hot fluid.

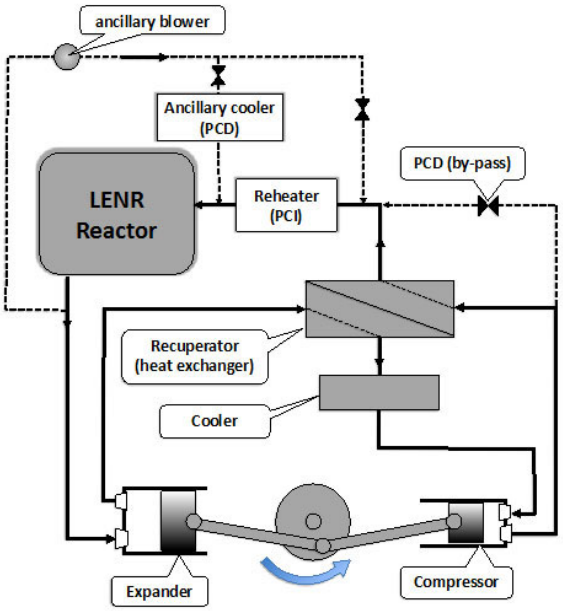


**Figure 17.** Coupling with an Ericsson engine.

The engine transforms the heat into mechanical power. The engine is coupled to an electrical generator that produces electricity. A fraction of the electrical energy is used to energize the excitation supply and the other control systems. The surplus is exported. The power is controlled via the level of excitation. Additional control is provided with PCI and PCD functions. An enclosure confines the whole assembly. The roles of the enclosure are discussed below.

This general description must be adapted following the exact type of reactor and engine used. In order to explain how these principles can be translated into design features, some examples are detailed in the following.

## 4.3. Coupling with various heat converters

### 4.3.1. *Thermoelectric converters*

Figure 16 shows a LENR reactor made of reactive cells covered by thermoelectric heat converters (TEC) [11]. The backsides of these panels are cooled to remove the heat. Initial warming can be obtained by applying a DC current in the TECs to use them temporarily as heaters during the startup phase. The level of power extracted from the reactive cells can be regulated through the amount of electrical current exported. This makes fine PCI or PCD possible. Forced PCD cooling can be obtained with the help of an external DC source to enhance the heat removal. To date, the thermal efficiency of TECs is too low to make this solution viable. The situation may change when new TEC devices become available [12,13]. This type of LENR generator would be attractive because of the absence of moving parts other than the cooling fluid pump.

#### 4.3.2. *Ericsson engine generator*

Figure 17 shows an Ericsson engine, which includes expansion and compression cylinders, fitted with admission and exhaust valves. A heat exchanger recuperates a large part of the heat not transformed into mechanical energy, so that the efficiency is good [14].

The recuperator and the cooler may have large sizes. This reduces the gas pressure drops, and the associated energy losses. The pressure drops are also dramatically reduced if the gas loop is pressurized. The metallurgical heat resistance of the hot parts limits the working temperature of an Ericsson engine to approximately 600°C.

PCI takes the form of an ancillary gas re-heater arranged on the gas line entering the reactor. This re-heater allows the reactor warming for the startup phase. During that period, the engine does not yet produce power. An ancillary blower must provide the gas circulation. Alternatively, the gas is circulated by the engine itself, driven by the generator used temporarily as a motor. PCD can be finely tuned during operation via a by-pass of the recuperator, as shown in the picture. PCD forced cooling is also feasible with another cooler combined with the ancillary blower.

The PCD can be finely tuned during operation via a by-pass of the recuperator, as shown on the picture. The PCD forced cooling is also feasible with another cooler combined with the ancillary blower.

#### 4.3.3. *Brayton gas turbine*

A closed loop gas turbine with the Brayton cycle is a suitable heat engine if the temperature exceeds about 700°C (see Fig. 2) [15]. Figure 18 shows the configuration. It is quite similar to the Ericsson system, except that rotating

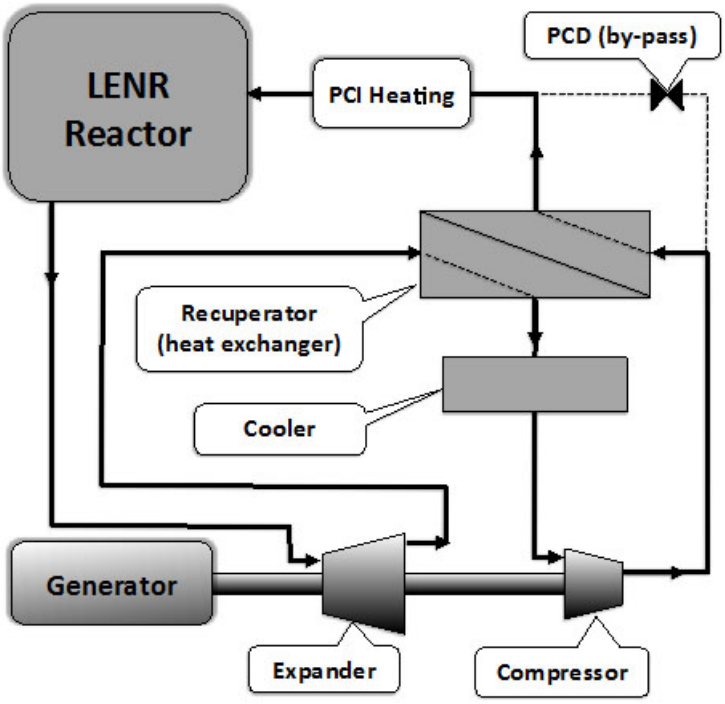


**Figure 18.** Coupling with a closed cycle gas turbine.

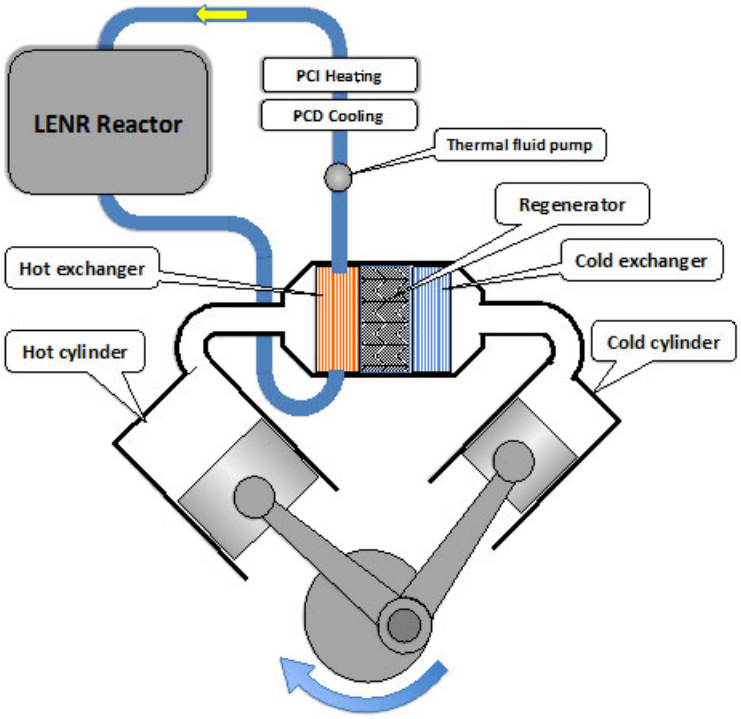


**Figure 19.** Coupling with a Stirling engine (two pistons type). The heat is transferred from the reactor to the engine hot exchanger by a hot fluid loop.

equipment replaces the volumetric machines. During startup, the generator is used temporarily as a motor. The PCI is included as a gas re-heater before the reactor. A recuperator by-pass line provides the PCD function.

#### 4.3.4. *Stirling engine*

Figure 19 schematizes the coupling of an LENR reactor with a Stirling engine. In this type of engine, a confined mass of gas is alternatively transferred between a cold and a hot cylinder, while being heated or cooled. A heat regenerator greatly improves the thermal efficiency. There are no gas valves. Several types of Stirling engines exist, with different arrangements of the cylinders [16].

The gas volume enclosed in the exchangers and regenerator must be commensurate with the volume swept by the cylinders. The size of the exchangers is therefore limited, and this gives a limit to the actual efficiency and power density of the Stirling engines. The working gas is preferably of high conductivity ($H_2$ or He). In order to control the effect of the viscous pressure drops, the gas circuit is pressurized The temperature in the hot exchanger is limited below about 700°C to withstand the high pressure. Because of the limited size of the hot exchanger, it is beneficial to input the heat by a fluid (gas or liquid) heat transfer circuit, as shown in Fig. 19. A pump drives the heating fluid circulation. A re-heater installed in the fluid loop provides the PCI function. The PCD is obtained via a cooler also inserted in the circuit. The heating fluid loop is started before and independently from the Stirling engine.

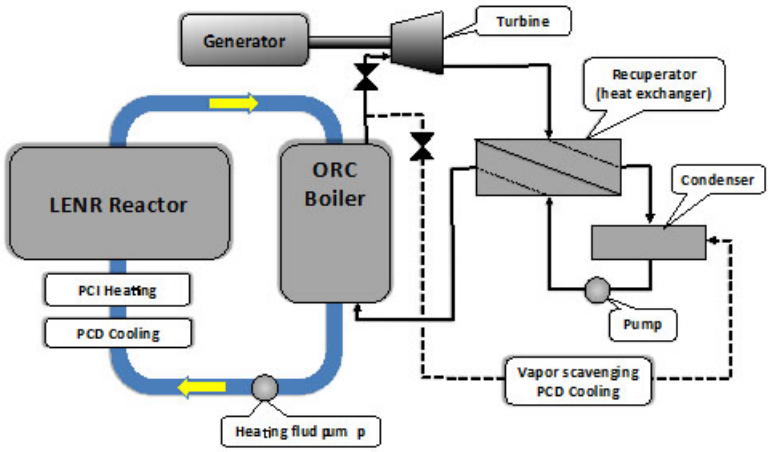


**Figure 20.** Coupling with an ORC turbine.

### 4.3.5. *Organic Rankine cycle*

Figure 20 shows the principle of an Organic Rankine Cycle (ORC) turbine coupled with an LENR reactor. An organic fluid is vaporized under pressure in the boiler. The vapor is expanded in the turbine. The residual heat of the low pressure vapor is recovered in the heat exchanger. The vapor is condensed, and the liquid is pumped back to the boiler [17].

This description seems similar to a steam turbine. The use of an organic compound simplifies the overall design, because for a given temperature the pressure level can be much lower than for steam. In most cases, the turbine

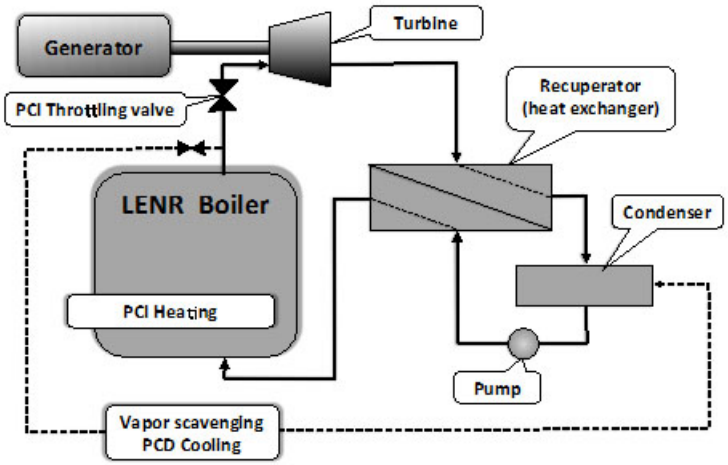


**Figure 21.** Boiling LENR reactor. The fluid boils between the cell gaps. PCI: The re-heating of the reactor is provided by an ancillary heater immersed in the boiler. PCD: A vapor scavenging line allows the cooling of the boiling fluid.

includes only one or two stages of blades. Contrary to steam, the expansion of the organic vapor does not result in partial condensation. The absence of liquid droplets in the vapor stream eliminates the potential erosion of the turbine blades. Many different compounds are available following the temperature, between 100°C and 350°C [18].

The heat transfer fluid can be oil, a liquid salt or metal. It may also be a diphasic circuit, for example pressurized steam vaporized in the LENR reactor and condensed in the ORC boiler. This last option is interesting if the LENR reactor is a high temperature electrolytic system, provided the COP of the process is sufficient. To increase the power, the LENR reactor is re-heated by a PCI unit arranged on the hot fluid loop or inside the reactor When the operation temperature increases, the vapor pressure in the boiler increases as well. A throttling valve regulates the vapor flow rate admitted in the turbine.

The PCD may be a cooler installed on the fluid loop. A vapor line directly linked between the boiler and the condenser can provide additional cooling. Scavenging vapor results in a fast cooling of the fluid contained in the ORC boiler.

#### 4.3.6. *Boiling reactor*

Figure 21 shows a boiler heated by LENR cells, coupled to a turbine. Future large reactors operated between 200°C and 300°C may use a technology similar to BWR, with water as a cooling fluid and condensing steam turbines [19]. However, as LENR does not suffer of the same constraints as fission reactors in terms of materials and neutron flux, organic fluids or other chemicals may replace water. This will make it possible to operate with modest pressures. Small units are also feasible.

#### 4.3.7. *Classification of the potential techniques*

The different techniques for heat transfer and heat engines are summarized in Fig. 22 according to their typical temperature domain. The range of possibilities is very large and this sketch is only indicative.

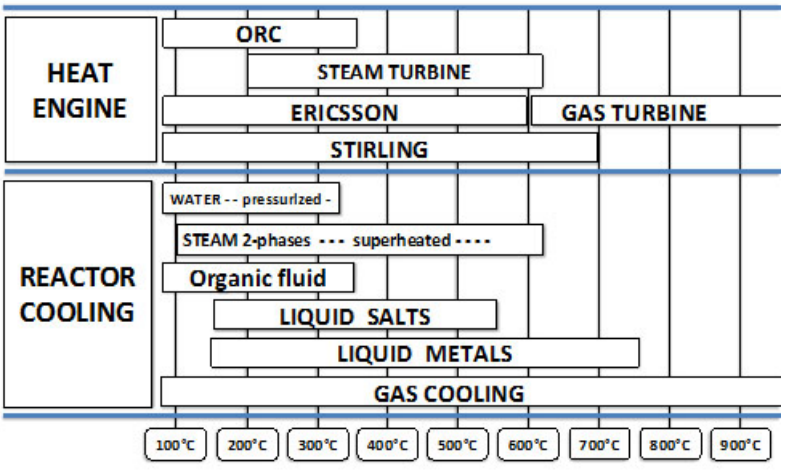


**Figure 22.** Typical temperature domains for reactor cooling and heat engine types.

### 4.4. Enclosure design

The last item visible in Fig. 15 is the enclosure that surrounds the whole generator assembly. The enclosure serves a dual purpose:

- Limits the thermal losses to the environment.
- Avoids the hydrogen (deuterium) loss to the atmosphere.

Heat losses originate at the LENR reactor walls, the hot parts of the heat engine, the heating fluid piping. These pieces must be adequately insulated in order to limit heat transfer to the environment by conduction, convection and radiation.

Some LENR processes require the presence of hydrogen ($H_2$) or deuterium ($D_2$) to drive the reactions. It is supposed that the LENR cells are inserted in metallic containers. The walls of these containers are hot during operation. At high temperature, $H_2$ or $D_2$ diffuse through the metals. This is a problem in the case of $D_2$, because this expensive gas must be conserved as much as possible.

The light gases leak out of the cells and accumulate in the cooling fluid, gaseous or liquid. The cooling fluid loop must be designed to accommodate their presence. Because the partial pressure of the light gas in the cooling fluid is nonzero, from there, it can diffuse further within the atmosphere of the thermal insulation material. It is supposed that the temperature of the enclosure wall is close to the ambient, and that all passages through the wall are gas tight, so that the enclosure does not leak any $H_2$ or $D_2$. The light gas accumulates within the insulation lagging. From there, it may be recovered by a gas separation unit.

The presence of light gases in the insulation increases the gas thermal conductivity and adversely influences the insulation performance. The higher conductivity must be taken into account.

## 5. Conclusion

The LENR reactors able to deliver heat at a high temperature can be coupled with heat engines to generate electrical power. If the temperature and the COP are sufficient, the power covers the needs for the reactor excitation and surplus electricity is available for external use

According to the literature, the heat generation rate of some LENR processes increases rapidly with the temperature. It is desirable that the R&D related to all LENR processes includes the study of the influence of the temperature. The future industrial reactors will have to be designed in order to guarantee a safe and stable operation. Cooling is achieved by a fluid in direct contact with the reactive cells. Power control can be obtained through an appropriate temperature regulation. Several types of heat engines can be coupled to LENR reactors to generate electricity.

Heat losses must be minimized thanks to a sufficient thermal insulation. The insulation enclosure is also useful to recover the leaks of light gas if any. This may be an important economical factor if deuterium is utilized in high temperature reactors.

## Acknowledgments

The author acknowledges and thanks the referee for his editorial assistance and very helpful comments and suggestions.

## References

[1] M. Srinivasan and A. Meulenberg (Guest Editors), Current Science, Special section, *Low Energy Nuclear Reactions* **108**(4) (2015).

[2] J. Ruer, Characterization of energy fluxes in LENR reactors, excess heat, coefficient of performance and conditions for self-sustained operation, *J. Condensed Matter Nucl. Sci.* **21** (2016) 18–30.

[3] Heat engine, https://en.wikipedia.org/wiki/Heat_engine.
[4] Thermal efficiency, https://en.wikipedia.org/wiki/Thermal_efficiency.
[5] M. Fleischmann and S. Pons, Calorimetry of the PdD–$D_2O$ system: from simplicity via complications to simplicity *The Third Int. Conf. on Cold Fusion,* 1992, Nagoya, Japan, Universal Academy Press, Tokyo, p. 47.
[6] E. Storms, *The Explanation of Low Energby Nuclear Reaction*, Infinite Energy Press, 2014, p. 216.
[7] J.-P. Biberian, G. Lonchampt, L. Bonnetain and J. Delepine, Electrolysis of $LaAlO_3$ single crystals and ceramics in a deuteriated atmosphere, *The Seventh Int. Conf. on Cold Fusion,* 1998, Vancouver, Canada, ENECO Inc., Salt Lake City, UT, p. 27.
[8] E.K. Storms, How basic behavior of LENR can guide a search for an explanation, *J. Condensed Matter Nucl. Sci.* **20** (2016) 105–143.
[9] Arrhenius equation, Wikipedia, https://en.wikipedia.org/wiki/Arrhenius_equation.
[10] Thermopedia, Heat Transfer Coefficient, www.thermopedia.com/content/841/ .
[11] Thermoelectric generator ], Wikipedia, https://en.wikipedia.org/wiki/Thermoelectric_generator.
[12] Thermoelectric materials , Website of the TU-Chemnitz, https://www.tu-chemnitz.de/physik/OFGF/research/thermoelectrics.php.
[13] H. Schock, G. Brereton, E. Case, J. D'Angelo, T. Hogan, M. Lyle, R. Maloney, K. Moran, J. Novak, C. Nelson, A. Panayi, T. Ruckle, J. Sakamoto, T. Shih, E. Timm, L. Zhang, and George Zhu, Prospects for implementation of thermoelectric generators as waste heat recovery systems in class 8 truck applications, *J. Energy Resour. Technol.* **135** (2013) 022001.
[14] ] Wikipedia, Ericsson engine, https://en.wikipedia.org/wiki/Ericsson_cycle.
[15] Wikipedia, Closed-cycle gas turbine, https://en.wikipedia.org/wiki/Closed-cycle_gas_turbine.
[16] Wikipedia, Stirling engine https://en.wikipedia.org/wiki/Stirling_engine.
[17] Wikipedia, Organic Rankine cycle. https://en.wikipedia.org/wiki/Organic_Rankine_cycle.
[18] Ngoc Anh Lai, Martin Wendland and Johann Fischer, Working fluids for high-temperature organic Rankine cycles, *Energy* **36** (2011) 199–211.
[19] Wikipedia, Boiling water reactor, https://en.wikipedia.org/wiki/Boiling_water_reactor.

J. Condensed Matter Nucl. Sci. 22 (2017) 27–34

Research Article

# On Plausible Role of Classical Electromagnetic Theory and Submicroscopic Physics to understand and Enhance Low Energy Nuclear Reaction: A Preliminary Review

Victor Christianto*, †,‡

*Malang Institute of Agriculture (IPM), Jl. Soekarno-Hatta, Malang, Indonesia*

Yunita Umniyati §,¶

*Head of Physics Laboratory, Swiss-German University, BSD City, Tangerang, Indonesia*

Volodymyr Krasnoholovets‖

*Institute of Physics, Kyiv, Ukraine*

**Abstract**

In this paper, we discussed how we can study some effects associated with LENR/CMNS from the principles of classical electromagnetic theory, and also from a very new approach based on a submicroscopic concept of physics. Perhaps our considerations have their own risks because the majority of mainstream physicists consider nuclear fusion rather as a phenomenon associated with tunneling through a Coulomb barrier, which is a pure quantum effect. We will discuss that there are some aspects of classical electromagnetic theories which may have impact on our understanding on LENR/CMNS phenomena, including: (a) nonlinear electrostatic potential as proposed by Eugen Andreev, (b) vortex sound theory of Tsutomu Kambe, (c) nonlinear ponderomotive force, and (d) submicroscopic consideration.
 ISSN 2227-3123

*Keywords:* Classical electromagnetic theory, Coulomb barrier suppression, Electronuclear potential, Nuclear Van der Waals force, Ponderomotive force, Subdeuterium, Submicroscopic physics, Vortex sound theory

*E-mail for correspondence: VictorChristianto@gmail.com.
†Founder and CEO of www.Ketindo.com.
‡URL: http://www.researchgate.net/profile/Victor_Christianto.
§E-mail: Yunita.Umniyati@sgu.ac.id.
¶Research & E-learning Development Director of www.Ketindo.com.
‖E-mail: krasnoh@iop.kiev.ua.

 ISSN 2227-3123

## 1. Introduction

Since Pons and Fleischmann reported their experiments in 1989, many labs in the world tried to replicate their results, but many failed. Thereafter, there was a wave of rejection to their claim of table-top nuclear fusion at room temperature. Some establishment physicists even called "cold fusion" *pathological science*. But many nonmainstream physicists and chemists continued their works in an underground manner. Also some eminent physicists have taken risks to join this underground movement, including Prof. Peter Hagelstein from MIT.

But the rejection of mainstream physics towards cold fusion/LENR remains strong. Even the famous Prof. Brian Josephson from Cavendish Lab. in Cambridge University was denied access from arXiv server because of his endorsement to E. Storms' works. He went on to write a paper suggesting that such a denial of many successful experiments related to cold fusion/LENR can be called "*pathological disbelief*."

In this context, allow us to recall a story that was told to the first author (VC) several times by Dr. Iwan Kurniawan, a nuclear engineer from Indonesia.[a] When he was a doctoral student in a University in Japan in the 1990s, his professor invited him to do an experiment related to cold fusion in the physics lab. After setting all the apparatus properly, they went home. In the morning, they were surprised that all the apparatus was blown up and it damaged the window glasses in lab. Dr. Iwan told me that since then he concluded that cold fusion does not work as claimed by Pons and Fleischmann.

He has been one of our good friends for a long time, and he and VC often discussed many things. But we have a different opinion regarding his cold fusion experiment: the fact that the apparatus blew the entire lab indicates that there was huge energy release in the device, so huge that it damaged the window glass. The problems appear to come from at least two aspects: (a) poorly understood mechanism of the reaction and (b) the reactor failed to work properly. So, it is basically similar to reactor meltdown in a usual fission reactor. We need to learn what makes their cold fusion reactor failed. It is not because there is no energy inside the system, but because there was a huge energy release. Reactor shutdown has recently been admitted as one of the real problems in many LENR reactors, and this is a challenge for experimenters and companies who want to design commercial LENR reactors [8–10].

However, in this paper we will not repeat such debates that have been discussed many times elsewhere. Instead we will discuss how we can study some effects associated with LENR from the principles of classical electromagnetic theory. We are aware that this approach has its own risks, because many physicists consider that nuclear fusion should be associated with tunneling through Coulomb barrier, and this kind of tunneling is a pure quantum effect. But is that true?

We will discuss the possibility there are some aspects of Classical electromagnetic theories which may have an impact on our understanding on LENR phenomena, including: (a) nonlinear electrostatic potential as proposed by Eugen Andreev, (b) vortex sound theory of Tsutomu Kambe, and (c) nonlinear ponderomotive force. The latter aspect has been proposed recently by Lundin and Lidgren in order to understand the mechanism of LENR [13,14].

It is our hope that this paper will motivate young electrical engineers to study LENR phenomena from new perspectives starting from classical electromagnetic theories. In short, classical electromagnetic theories still offer many surprises to those who are willing to dig deeper into the hidden mysteries of nature.

## 2. Nonlinear Electrostatic Potential of Eugen Andreev

In modern physics, there is a firm conviction based on the vast empirical material that:

- The electromagnetic and nuclear interactions are of a different nature.
- The field of electric charge (proton, electron) is spherically symmetric.

[a] Special thanks to Dr. Iwan Kurniawan for telling his first-hand experiment with cold fusion. Wishing you will recover soon, brother!

- The nucleon–nucleon forces depend on the direction.

In his paper, Andreev [1] suggested a hypothesis that the notion of the nuclear interaction could be interpreted as a nonlinear distribution of the electrostatic potential, which manifests itself on the Fermi scale. An analytical form of the potential of the proton is proposed, which coincides with conventional forms used in the nuclear physics at a short scale, but becomes the usual Coulomb potential at a large scale.

The model potential possesses a set of properties that could be called "*nuclear van der Waals forces*."

Coulomb's law can be written in integral form as follows [1].

$$\phi(x,y,z) = \frac{k\phi}{R} = -k \iiint\limits_{v} \frac{\mathrm{div}(\nabla\phi(x,y,z))\mathrm{d}V}{\sqrt{(x^2+y^2+z^2)}}. \tag{1}$$

If we replace $R$ with $R_{\mathrm{dd}}$, which is defined as follows:

$$R_{\mathrm{dd}} = \sqrt{x^2+y^2+\beta^2 z^2+r_{\mathrm{o}}^2}. \tag{2}$$

Then we will have a two parameter field potential [1]

$$\varphi(x,y,x,\beta,r_0) = \frac{\varphi}{R+r_0} \tag{3}$$

or

$$\varphi(x,y,z,\beta,r_0) = [\phi]\left(\frac{k_1}{R_{\mathrm{dd}}} + \frac{k_2}{\left|R_{\mathrm{dd}}\right|^2}\right). \tag{4}$$

In Andreev's approach, two new parameters were introduced, namely, a fundamental length of Heisenberg, $r_0$, which has to describe a discreteness of the physical vacuum and a parameter $\beta$ depicting a deformability or polarizability of the physical vacuum. The conventional Coulomb's law appears from Andreev's expressions when $\beta = 1$ and $r_0 = 0$.

As a result, Andreev obtained an explicit analytic form of the *electronuclea*r potential of a proton [1]:

$$\varphi_{(\mathrm{proton})} = \frac{r_0}{\sqrt{(x^2+y^2+2z^2+r_{\mathrm{o}}^2)}} + \frac{\mathrm{d}z\, r_0^2}{(x^2+y^2+2z^2+r_{\mathrm{o}}^2)}. \tag{5}$$

Especially for one of the four orientations in a wide range of distances, the interaction energy Eq. (5) is negative, which indicates the existence of an *attractive* force and the possibility of forming a bound state [1]. Such behavior is similar to the van der Waals interaction (dipole–dipole, dipole-induced dipole, dipole–quadrupole interaction, etc.) which emerges between two nonbonded atoms and can be expressed as a function of internuclear separation, $r$.

This model includes a kind of anisotropy of space, represented by a coefficient "beta" in the direction $Z$ of the nuclear spin, and includes also a parameter $r_0$ to eliminate the infinities in $r = 0$: $r_0$ would be the size of a discrete elementary cell of the physical (quantum) vacuum. This is very interesting, because in particular, it leads without preliminary hypothesis to retrieve the space partitioning into three areas, with a + sign for two external areas and a – sign for an internal one: that could represent the three quarks. Moreover, by computing the total energy of a proton-proton interaction, according to Andreev's potential model and as a function of various relative orientations of the proton, the author finds a mutual orientation providing an attractive interaction.

The above result, in fact, demonstrates the Coulomb barrier suppression starting from classical electromagnetics theory. Furthermore, Andreev has shown that PP potential as described above can be compared with [1]:

- Lennard–Jones potential (resulting from the van der Waals interaction):

$$V_{\mathrm{LJ}} = \frac{0.01}{r^{12}} - \frac{1}{r^5}. \tag{6}$$

- Reed potential

$$V_{\mathrm{Reed}} = -10\frac{\mathrm{e}^{-r}}{r} - 1650\frac{\mathrm{e}^{-4r}}{r} + 6484\frac{\mathrm{e}^{-7r}}{r}. \tag{7}$$

Thus the introduction of the discreteness of space ($r_0$) and its deformability ($\beta$) allows one to resolve the problem of overcoming the Coulomb barrier in nuclear physics.

Although this approach hints at a solution, much work still needs to be done, especially to establish how this model can be compared head-to-head with LENR/CMNS experiments. For more detailed information, the reader is advised to refer [1].

## 3. Vortex Sound Theory of Tsutomu Kambe [2–4]

The above-described electronuclear potential starts with electrostatics/Maxwell equations. It is very interesting to note that Prof. T. Kambe from University of Tokyo has made a connection between the equation of vortex sound and fluid Maxwell equations.

Kambe wrote that it would be no exaggeration to say that any vortex motion excites *acoustic* waves. Kambe considers the equation of vortex sound of the form [2] :

$$\frac{1}{c^2}\partial_{\mathfrak{t}}^2 p - \nabla^2 p = \rho_0 \nabla \cdot L = \rho_0 \,\mathrm{div}(\omega \times v). \tag{8}$$

Also Kambe wrote that dipolar emission by the vortex–body interaction is [3]

$$p_{\mathrm{F}}(x,t) = -\frac{P_0}{4\pi c}\dot{\Pi}_i\left(t - \frac{x}{c}\right)\frac{x_{\mathfrak{c}}}{x^2}. \tag{9}$$

Then he obtained an expression of fluid Maxwell equations as follows [4]:

$$\begin{aligned} &\nabla \cdot H = 0, \\ &\nabla \cdot E = q, \\ &\nabla \times E + \partial_{\mathfrak{t}} H = 0, \\ &a_0^2 \nabla \times H - \partial_{\mathfrak{t}} E = J, \end{aligned} \tag{10}$$

where [4] $a_0$ denotes the sound speed and

$$\begin{aligned} q &= -\partial_{\mathfrak{t}}(\nabla \cdot \upsilon) - \nabla \hbar, \\ J &= \partial_{\mathfrak{t}}^2 v + \nabla \partial_{\mathfrak{t}} h + a_o^2 \nabla \times (\nabla \times \upsilon). \end{aligned} \tag{11}$$

In our opinion, this new expression of fluid Maxwell equations suggests that there is a deep connection between vortex sound and electromagnetic fields. Therefore, it may offer new ways to *alter* the form of electronuclear potential as described in Section 2.

However, it should be noted that the above expressions based on fluid dynamics need to be verified with experiments. We should note also that in Eqs. (10) and (11), the speed of sound $a_0$ is analogous of the speed of light in Maxwell equations, whereas in Eq. (8), the speed of sound is designated "$c$" (as analogous to the light speed in electromagnetic (EM) wave equation).

For octonic formulation of fluid Maxwell equations, see [15]. For alternative hydrodynamics expression of electromagnetic fields, see [16].

## 4. Nonlinear Ponderomotive Force

According to Brechet et al. [6], a ponderomotive force results from the response of inhomogeneous matter fields to the presence of electromagnetic fields. In particular, the Miller ponderomotive force could explain transmutations by thermal capture of neutrons in the context of the classical EM theory.

Ponderomotive forces are generally overlooked since the electromagnetic community is not much concerned with continuum mechanics, and the continuum mechanics community does not usually deal with electromagnetic systems.

The nonrelativistic ponderomotive force as proposed by Miller (1958) is as follows [7] :

$$F = m\ddot{\vec{r}} = -\frac{q^2}{4m\omega^2}\nabla\left|\vec{E}(r,t)\right|^2. \tag{12}$$

Equation (12) can obviously be derived from the ponderomotive potential:

$$\varphi_{(\mathrm{p})}(r,t) = \frac{q^2}{4m\omega^2}\left|\vec{E}(r,t)\right|^2. \tag{13}$$

Other than Miller's force, there are other types of ponderomotive forces, i.e. [5] :

- Abraham force (1903),
- Barlow (1958),
- Lundin and Hultqvist (1989),
- Bolotovsky and Serov (2003).

It can be noted here that the Miller force is independent of wave frequency for $\omega^2 \ll \Omega^2$ and *attractive* for the entire frequency range below resonance. The Miller force is *repulsive* at frequencies above resonance, but decays strongly at higher frequencies. Ponderomotive forcing by electromagnetic waves is capable of causing the attraction of solid bodies.

Brechet et al. [6] discuss the electromagnetic force density of magnetoelectric ponderomotive force, which is different from Miller's force.

In a recent paper, Lundin and Lidgren proposed that Miller ponderomotive force may offer an explanation to nuclear spallation as observed in some LENR experiments [13]. Although their study is not yet conclusive, it opens an entirely new way to discuss LENR based on pure classical electromagnetic theory.

## 5. Submicroscopic Consideration

Monograph [11] presented a detailed structure of physical space (or a vacuum, ether), which is based on pure mathematical principles — set theory, topology and fractal geometry. The study shows that matter appears from a primary substrate that has a structure of a mathematical lattice named the *tessellattice.* Thus, all massive particles as well as electrically charged particles emerge from the tessellattice as local distortions of its cells. In this motion such anamorphosis has to interact with the *tessellattice*, which is neglected in quantum mechanical, quantum field and electromagnetic theories. The bulk fractal deformation of a cell of the tessellattice is associated with the notion of mass; it is thought that the surface deformation of a cell is related to the electric charge.

Hence, two kinds of equations should appear: one system of equations describes the behavior of a massive particle and one more system of equations depicts the behavior of the electric charge. The first system is quite new and presented in a book [11] and it is related to the quantum mechanical formalism; the other system is reduced to the conventional Maxwell equations, which is also illustrated in this book [11].

It has been demonstrated [11] that the interaction of a moving particle with the tessellattice results in the generation of a new kind of quasi-particles named *'inertons'*. These inertons are carriers of massive properties of particles and

they play in some sense the role of hidden variables introduced in physics by de Broglie, Bohm and Vigier. Inertons exchange by mass, speed and hence momentum and kinetic energy with the particle that generates them. A section of space known as the particle's de Broglie wavelength $\lambda$ is the spatial amplitude of the particle. It is a section in which the particle initially generates inertons and passing the whole kinetic energy to the generated cloud of inertons finally stops; then in the next section $\lambda$ inertons guide the particle passing on to it their velocity, mass, momentum and kinetic energy.

The particle's inerton cloud together with the particle, which exist in real space, are projected to the quantum mechanical formalism, which was developed in a phase space, as the particle's wave $\psi$-function. Thus, in a solid each atom is surrounded with its inerton cloud; the same for each free electron, proton or another canonical particle.

In the recent experiment [12], in a chamber filled with a gas, a discharge has been generated. Positive ions of the gas reached the cathode where they interacted with atoms of an electrode made of tungsten. If the gas is hydrogen, discharges produce free protons in it. Reaching the cathode, protons interact with a metal matrix in such a way, that at the resonance conditions, i.e. when the momenta of the interacting atom and proton are coincide by absolute value and have opposite directions, i.e. the proton impacts the tungsten atom being in antiphase oscillating in its site of the crystal lattice, both particles must stop, $m_{\mathrm{p}}\vec{v}_{\mathrm{p}} + m_{\mathrm{W}}\vec{v}_{\mathrm{W}} = 0$. This condition means that the proton knocks out the tungsten's atom inerton cloud.

One of the free electrons available at the surface of the electrode absorbs the tungsten atom's inerton cloud and also traps a proton. The merging of the heavy electron with the proton results in the creation of a super heavy hydrogen atom. In this system the reduced mass of the proton and the electron is almost equal to $m_{\mathrm{p}}$ (indeed $1/m_{\mathrm{p}} + 1/(m_{\mathrm{e}} + m_{\mathrm{W}}) \simeq 1/m_{\mathrm{p}}$). Therefore, the proton starts to rotate around the heavy electron; the Bohr radius for the rotating proton is

$$r_{\mathrm{p-e}} = \frac{4\pi\varepsilon_0\hbar^2 n^2}{\mathrm{e}^2 m_{\mathrm{p}}} = 2.88 \times 10^{-14}\mathrm{m}, \tag{14}$$

where we put $n = 1$. Although the electron orbit (14) deeply penetrates into the middle of the proton, the electron still does not reach the critical distance of $2 \times 10^{-14}$ m that characterizes the quark orbit inside the proton [11]. If we put $n = 2, 3$, the radius (14) will be larger but still in the order of femtometers.

What is interesting, these small atoms named subatoms [12] behave like neutrons, namely, neutron detectors measured the presence of neutrons in the experiment conducted. We [12] were able to generate subatoms, such as subhydrogen and subhelium (in a helium atmosphere), which were perceived by the neutron detector as real neutrons. The intensity of the measured "neutron" radiation was rather significant; the maximum value measured by the detector was $3 \times 10^5$ neutrons/cm$^2$ min. Nevertheless, the real intensity could even be five orders higher. Besides, analyzing our experiments, we came to the conclusion about the existence of other tiny systems: subdeuterium, neutral (deuteron + subhydrogen) pair, and neutral (deuteron + subhelium) pair.

Many other researchers reported similar very small stable atoms, or combined particles, though they were unable to explain their structure and properties.

All these nuclear systems had the size around several units of $10^{-14}$ nm. They can be generated artificially in a chamber filled with a gas. When a discharge is generated in the chamber, positive ions of the gas reaches the cathode where they interact with atoms of the electrode, which is typically made of tungsten.

When we launch the production of subatoms and the above mentioned nuclear pairs, at the high intensity of these entities we are able to anticipate the real transformation of nuclei in the system. Indeed, tiny subatoms and nuclear pairs (with the size $\leq 5 \times 10^{-14}$ m) can easily penetrate the shell of electrons around each atom, which have a size around $10^{-10}$ m. In other words, a subatom or nuclear pair moving to the nucleus of the atom will pierce the electron shell similarly to a spaceship that is travelling in our solar system. Any electron of the electron shell cannot experience this pinhole because of the incommensurability of the sizes of tiny particles and electron orbits.

Note that Andreev's phenomenological approach [1] to the suppression of the Coulomb barrier is consistent with the submicroscopic concept. Andreev points to some minimum size $r_0$. Indeed, scales of sizes of objects that compose the universal tessellattice prescribe an order of sizes of stable structures starting from the minimum, which is the size of the quark (in the lattice, the size is $10^{-10}$ or $10^{-17}$ m) and the size of an atom (in the lattice, the size is $10^{-17}$ or $10^{-21}$ m) [11]. Hence real space has to influence a physical mechanism of interaction. The tessellattice possesses an elasticity and Andreev's parameter $\beta$ takes exactly this fact into account.

Approaching a nucleus, a subatom or nuclear part starts interacting with nuclides: a subatom brings to the nucleus a thermal proton (deuteron or $\alpha$ particle), the inerton cloud and electron. The electron will be getting away from the nucleus because it does not participate in nuclear reactions. But the proton (deuteron or $\alpha$ particle) will bring an additional interaction inside the nucleus, which has to result in its mutation.

In fact, studying samples of iron and samples of water contaminated with Cs-137 we [11] revealed significant mutations in iron (in which emerged such elements, as Co, Ni, Ca, Hf, Cs) and decrease in radioactivity of the water sample up to 30–40% at the application of an inerton field. It seems in those experiments initially subatoms formed that then influenced nuclei of Fe (in samples of iron) and nuclei of Cs-137 (in samples of water contaminated with radioactive cesium).

## 6. Discussion and Concluding Remarks

We have discussed a new expression of electronuclear potential starting from electrostatics law. This explains Coulomb barrier suppression from a purely classical origin, without the use of nuclear potential such as Woods–Saxon potential. The model potential possesses a set of properties that could be called "*nuclear van der Waals forces*." In our opinion, this is a quite surprising result that offers a novel way to explain low energy nuclear reaction (LENR) from Classical Electromagnetic theories.

Moreover, Kambe's new expression of fluid Maxwell equations suggests that there is a deep connection between vortex sound and electromagnetic fields. Therefore, this result may offer a new insight on how to *alter and modify* the form of electronuclear potential using vortex sound equations. This requires further investigations.

In a recent paper, Lundin and Lidgren proposed that Miller ponderomotive force might offer an explanation to nuclear spallation as observed in LENR experiments. Although their study is not yet conclusive, it opens an entirely new way to discuss LENR from purely classical electromagnetic theories.

The electrostatic/electronuclear potentials, fluid Maxwell equations and ponderomotive force have been proposed as an alternative to tunneling effects that could occur as a quantum mechanical consideration of LENR. However, in Section 5, we have shown that the tunneling effect itself can be considered in deeper terms, namely from the submicroscopic point of view. This is a quite new approach to the description of physical phenomena, which however, promises a lot in both our understanding of mysterious phenomena of nature and the modeling of some crucial experiments, such as LENR and similar work.

As follows from the submicroscopic concept, LENR can be possible only in the case when subatoms or nuclear pairs emerge in the system studied. An efficiency of LENR is directly proportional to the quantity of generated subatoms and nuclear pairs. That is why it seems possible that the highest efficiency in LENR can reached under the following two main conditions: (i) in a reaction chamber one has to increase the number of subatoms and nuclear pairs to the value of no less than $10^{12}$; at this quantity of deuterons in a macroscopic sample reactions $\mathrm{d} + \mathrm{d} = \mathrm{He}$ produces heat comparative to room temperature; (ii) we need to invent mechanism(s) that would stimulate collisions of subatoms and nuclear pairs with potential targets and between themselves.

Of course, we do not pretend to have the last word on how to apply Classical Electromagnetic theory to understand LENR, instead we offer some new insights on how to explain and enhance the Coulomb barrier suppression without the usual quantum tunneling paradigm.

It is our hope that some of the proposed new theoretical approaches as described herein will be proved fruitful in the continuing study of CMNS/LENR.

## Acknowledgements

The first author (VC) dedicates this paper to Prof. Liek Wilardjo and Dr. Iwan Kurniawan for all encouraging comments and discussions over many subjects for more than 10 years. Many thanks to Prof. Jean-Paul Biberian who has considered this paper for JCMNS. Special thanks to an anonymous reviewer for his encouraging remarks and correction.

## References

[1] E. Andreev, About the Coulomb barrier in LENR processes (2015). URL: http://www.e-catworld.com/wp-content/uploads/2016/01/Coulomb-barrier-in-LENR.pdf.

[2] T. Kambe, Vortex sound with special reference to vortex rings: theory, computer simulation, and experiments, *Int. J. Aeroacoustics* **9**(1,2) (2010) 52. URL: http://www.purple.dti.ne.jp/kambe/IJA09-Vortex-Sound.pdf.

[3] T. Kambe, Theory of vortex sound with special reference to vortex rings, *Int. Conf. Math. Fluid Dyn.*, Dec. 2004. URL: http://citeseerx.ist.psu.edu/viewdoc/download?doi=10.1.1.571.8078&rep=rep1&type=pdf.

[4] T. Kambe, New formulation of equations of compressible fluids on analogy of Maxwell equations, *Fluid Dyn. Res*. **42** (2010) 4 . URL: http://www.purple.dti.ne.jp/kambe/FDR-IOP-42(2010).pdf.

[5] Rickard Lundin and A. Guglielmi, Ponderomotive force in cosmos, *Space Sci. Rev.* **127** (2006) 1–116.

[6] S.D. Brechet, A. Roulet and J.P. Ansermet, Magnetoelectric ponderomotive force, *Modern Phys. Lett.* B **27**(21) (2013) 1350150 (10 pages).

[7] D. Bauer, Theory of intense matter-laser interaction, 2006. URL: http://www.physik.uni-rostock.de/fileadmin/Physik/Bauer/tilmi.pdf.

[8] D. J. Nagel, Challenges, attractions and possible impacts of commercial generators based on low energy nuclear reactions, *Proc. ILENRS-'12*, Williamsburg, USA, July 1–3, 2012.

[9] D.J. Nagel, Potential advantages and impacts of LENR generators of thermal and electrical power and energy, *Infinite Energy* Issue 103, May/June 2012.

[10] L.F. DeChiaro, Low Energy Nuclear Reactions (LENR) Phenomena and Potential Applications, NAVSEA, Dahlgren Division (2015).

[11] V. Krasnoholovets, *Structure of Space and the Submicroscopic Deterministic Concept of Physics*, Apple Academic Press, Waretown, 2017.

[12] V. Krasnoholovets, Yu. Zabulonov and I. Zolkin, On the nuclear coupling of proton and electron, *Universal J. Phys. Appl.* **10**(3) (2016) 90–103. URL: http://www.hrpub.org/download/20160530/UJPA6-18406680.pdf.

[13] R. Lundin and H. Lidgren, Nuclear spallation and neutron capture induced by Ponderomotive forcing (2015). URL: https://documents.irf.se/get_document.php?group=Administration&docid=1772.

[14] R. Lundin and H. Lidgren, On the attraction of matter by the Ponderomotive Miller force (2010). URL: https://arxiv.org/pdf/1005.4913.pdf.

[15] M.Tanışlı, S. Demir and N. Şahin, Octonic formulations of Maxwell type fluid equations, *J. Math. Phys.* **56** (2015) 091701. URL: http://scitation.aip.org/content/aip/journal/jmp/56/9/10.1063/1.4930805.

[16] M. Liu, Hydrodynamic theory of electromagnetic fields in continuous media, *Phys. Rev. Lett.* **70**(23) (1993) 3580–3583. URL: http://www.uni-tuebingen.de/fileadmin/Uni_Tuebingen/Fakultaeten/MathePhysik/Institute/ITP/Dokumente/liu/phys-rev-lett-70-3580_1993.pdf.

J. Condensed Matter Nucl. Sci. 22 (2017) 35–46

Research Article

# Oscillating Excess Power Gain and Magnetic Domains in NANOR®-type CF/LANR Components

Mitchell R. Swartz*

*Nanortech Inc., Wellesley Hills, MA 02148, USA*

**Abstract**

Post-magnetization effects, both significant and time-variant, were observed in NANOR®-type CF/LANR components. In contrast to previously observed exponential falloffs of sample activity (peak incremental excess power gain), post-magnetization activity demonstrates oscillatory activity. This paper reports an analysis of the force density and expected theoretical frequency for oscillations, which have already been observed to exist between these magnetic domains after magnetization, calculated by using the Maxwell stress tensor.
 ISSN 2227-3123

*Keywords:* LANR, Magnetic domains, Magnetism, NANOR®, Oscillating power gain

## 1. Introduction – NANOR®-type CF/LANR Dry Preloaded Components

A NANOR®-type component is a hermetically sealed CF/LANR (cold fusion/lattice assisted nuclear reaction) nanomaterial, preloaded and arranged as a two-terminal electrical component which can yield significant heat (Figs. 1 and 2). They are designed to avoid leakage, enable stabilization and activation of the contained nanostructured alloyed material. As a result, the NANOR®-type preloaded component [1,2] has been like the proverbial "lab rat" for several papers, and was also the central component in an open demonstration at MIT in 2012 ([3]; which is one of the locations where the "normal" (unexposed to magnetization effects) exponential fall off of CF/LANR activity was followed over months). The papers include investigations of material science [4–6] and radiation physics [5,6,8], which have revealed several electrical transconduction states. Most importantly, of these transconduction states, only one produces the desired trait known as "excess heat" [7]. We begin by considering how the activity of these components is measured, and then how they are affected by the applied magnetic field intensity, and finally what may cause the post-magnetic activity-oscillations.

*Dr. Mitchell R. Swartz ScD, MD, EE, E-mail: nanors@nanortech.com.

 ISSN 2227-3123

## 2. Methods

### 2.1. Determination of activity of NANOR®-type components

The preloaded NANOR®-type components are driven by a high voltage circuit (up to 3000 V peak). In addition to using several types of commercial calibrations, we augment the calibrations using Keithley picoammeters (Types 480 and 486) and Keithley current sources (Type 225). For voltage measurements, Keithley electrometers (610B,610CR,602) and HP5334, HP3490, and Keithley multimeters were used. Voltage sources include HP-Harrisons, Kepco, and VWR. The input voltage was delivered in every run alternatively to the NANOR® and the ohmic control which was at the same location and used to thermally calibrate the system [9–11].

Input power is defined as $V \times I$. There is no thermoneutral correction in the denominator. Therefore, because consideration of loss by possible recombination is not removed, the observed power is a lower limit [12]. The energy calculations are also calibrated by time integration for additional validation. The instantaneous power gain (non-dimensional power amplification factor [10.11,13]) is defined as $P_{\rm out}/P_{\rm in}$. When present, the excess energy is defined as $(P_{\rm output} - P_{\rm input}) \times$ time. Data acquisition is taken from voltage and current sensors, and temperatures and heat flux sensors at multiple sites of the system. Data sampling is at 0.20 – 1 Hz, with 16–$24^{+}$ bit resolution, a voltage accuracy of $0.015^{+/-0.005}$ V, and a temperature accuracy of <0.6 degrees C. The noise power of the Keithley current sources driving the reactions is generally ~10 nW.

After driving the component and the control in each run, their power and energy gain were separately determined both by power-normalized delta-$T$ (d$T$/ $P_{\rm in}$), and input power normalized increase in heat flow (delta-HF/$P_{\rm in}$), and the directly by semiquantitative calorimetry [2,3]. In semiquantitative calorimetry, the amount of output energy is directly determined from the heat release, which is then compared to the input energy. The excess heat-producing activity can be determined by comparing the output of the NANOR® type component to the output of the precisely driven ohmic control, as demonstrated in the middle of Fig. 1.

### 2.2. Magnetization of NANOR®-type components

For what is reported here, the applied magnetization sequence consisted of rapidly repeating pulses of an intense >2 Tesla magnetic field intensity [4]. The applied magnetic field intensity, thus, highly fractionated with 3500 pulses delivered, each with a rise time of <0.1 ms, followed by an intra-pulse delay of one second.

## 3. Results

### 3.1. Response without applied magnetic field

Figure 1 shows the responses of these CF/LANR NANOR®-type components with any applied magnetic field intensity in three graphs of the same experimental run. A determination of the presence of excess heat can be made by comparing the output for NANOR®-type LANR component to the thermal (ohmic) control. The top of Fig. 1 shows the electrical input power and the incremental output temperature rise (defined as "delta-$T$"). The $x$-axis represents time. The $y$-axis on the left-hand side represents electrical input power in watts. The $y$-axis on the right-hand side represents delta-$T$. The calibration pulses, used for accuracy and precisions checks of voltages and currents and time, are also shown. The middle of Fig. 1 includes the same data but the incremental output temperature rise is normalized to the input power by dividing by the input power. This metric has delta-$T/P_{\rm in}$ be a nearly straight horizontal line for the ohmic control; which facilitates semiquantitative measurements by use of a simple ratio. The bottom of Fig. 1 is a full calorimetric presentation showing the input power and energy and output power and heat (energy) from the ohmic control and the NANOR®-type component at several input powers. The $y$-axis on the left-hand side represents electrical input power in watts. The $y$-axis on the right-hand side is the time-integrated amount of energy delivered at

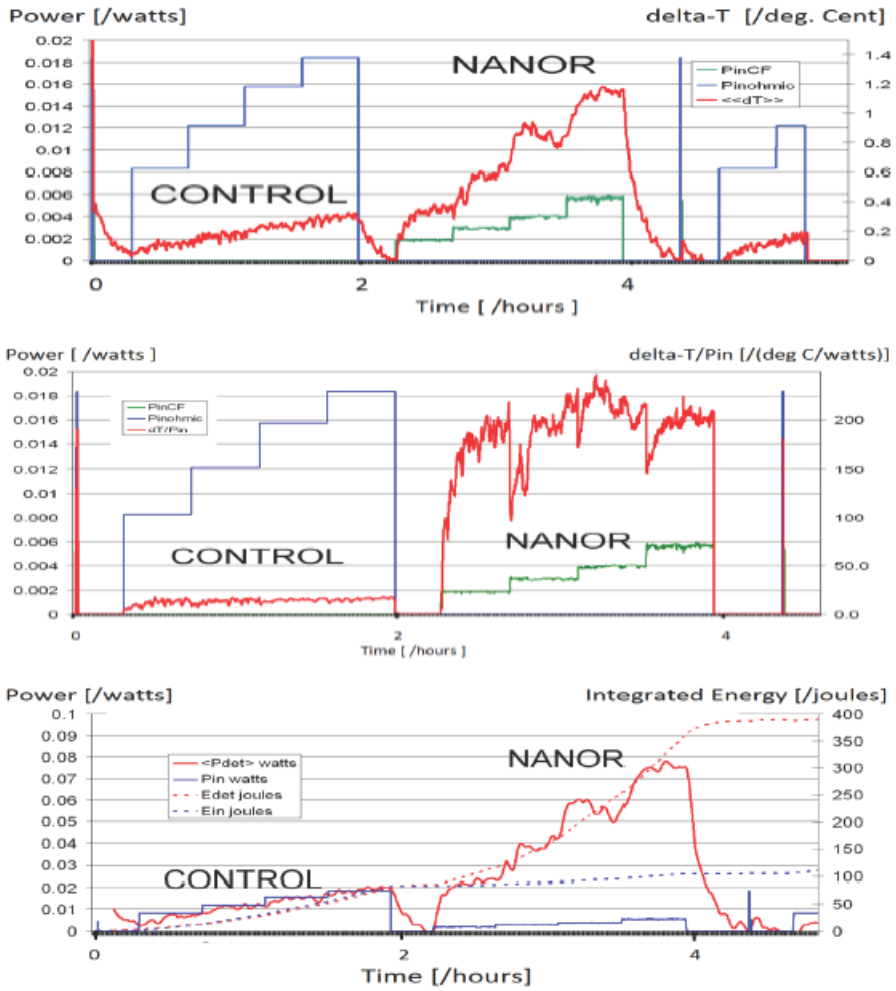


**Figure 1.** Response of a control and NANOR®-type component – No magnetic field. This figure shows three different ways of evaluating the possible presence of excess energy from a single run of an ohmic control and a NANOR®-type component. The ohmic control was driven first and then the component was electrically driven, as marked (*top*). The electrical input power and resultant delta-$T$ for the ohmic control and then the NANOR®-type component are shown (*middle*). The electrical input power and resultant delta-$T$ normalized to the input power (delta-$T/P_{\rm in}$). Importantly, this linearizes the output and enables calculation of power gain. In contrast to the graph on the top, this metric is a nearly straight horizontal line for the ohmic control (*bottom*). Calorimetric presentation of the input power and energy and output power and heat for the ohmic control and the NANOR®-type component.

input, and then released. The lighter energy curves (dots) are read off of the right-hand side $y$-axis, which represents the amount of energy released in joules.

Thus, these calorimetric curves rule out energy storage, chemical sources of the induced heat, possible phase changes, and other sources which might interfere with obtaining semiquantitative results.

Figure 2 shows the calorimetric responses of both the ohmic control and the preloaded NANOR®-type compo-

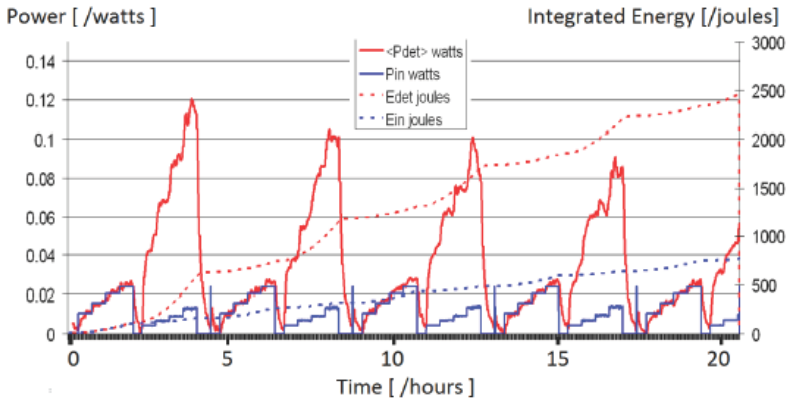


**Figure 2.** Reproducibility of a NANOR®-type component – No Magnetic Field. This is a calorimetric presentation of an experimental run, discontinuous with Fig. 3, with more than four cycles. The electrical input power and energy and output thermal power and heat are shown alternatively both from the ohmic control and the NANOR®-type component at several input powers. This component and control had NOT been driven in the presence of an applied magnetic field intensity, unlike Figs. 3 and 4.

nent over four complete cycles, at four different input electrical power levels. Figures 1 and 2 show that the active preloaded CF/LANR component has significant improvement in thermal output compared to a standard ohmic control (a carbon composition resistor). They also demonstrate that excess heat was produced only during energy transfer to the NANOR®-type LANR component heralding clearly over-unity thermal output power from it. Figure 2 demonstrates the reproducibility of the ohmic control and the near reproducibility of the NANOR®-type component over several cycles. In Fig. 2 the peak power gain of the NANOR®-type component slowly decreases, in a regular way, over time.

Figure 2 also demonstrates an exponential falloff of the peak incremental excess power gain. It is important to note that this component had NOT been driven in the presence of an applied magnetic field intensity, versus what is shown in Fig. 3. Contrast this exponential, slowly decreasing response, which is what was always seen [1–5], to the newly observed irregular, somewhat oscillatory-like, activity which occurred only after the components were exposed to the H-field, and only while an applied E-field was used to activate the CF/LANR component (Figs. 3 and 4).

## 3.2. Unique response after magnetic field

### 3.2.1. *Introduction – Magnetic responses in CF/LANR systems*

Previously, magnetic [14–16] and radiofrequency electromagnetic [17] effects have been reported in aqueous CF/LANR systems. In aqueous CF/LANR systems, steady magnetic fields have a small inhibitory effect on loading electrolysis when the applied H-field is perpendicular to the direction of the electrical currents [16]. In dry, preloaded CF/LANR systems, at higher electrical drive currents to the component, time-varying alternating magnetic fields simultaneously applied, induce small to significant increase gains in the activity [4] and some changes are long-lasting. Therefore, magnetically treated NANOR®-type components are called M-NANOR®-type components by our group to distinguish them and anticipate their unique oscillating-activity behavior and other longer term effects (Figs. 3 and 4).

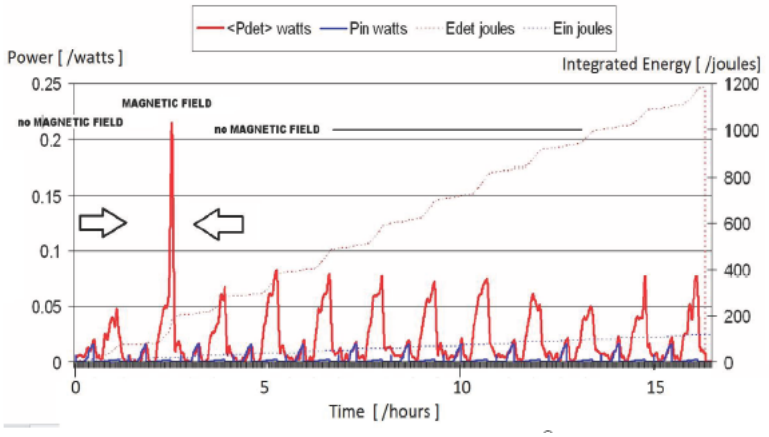


**Figure 3.** Impact of an H-field on the behavior of a NANOR®-type component. This experimental runs shows the impact of an applied H-field on the activity of a NANOR®-type component before, during and after, a single sequence of fractionated high intensity magnetic field application between the arrows. At all other points in time there were NO additional large applied magnetic field intensity. Note the absence of an exponential or linear fall-off of peak activity.

### 3.2.2. *Synchronous magnetically induced increased energy gain*

During the first magnetic-NANOR® run, we were quite surprised by the different responses of the NANOR® component during *and after* d$H$/d$t$ coercing. It was discovered that for magnetic interactions with active nanostructured CF/LANR systems [4], there is enhanced improvement of LANR (which occurs at the same time as the magnetization and therefore is called "synchronous"). As a result of the magnetization sequence, there appeared a significant increase

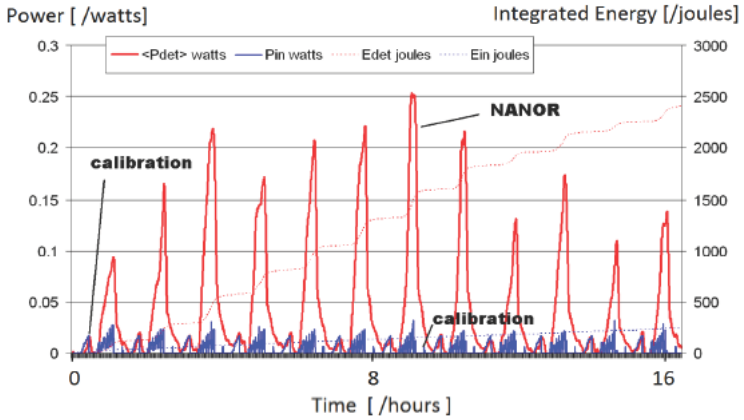


**Figure 4.** Subsequent late-term impact of magnetization on CF/LANR activity. The post-magnetization electrical input power and energy and output power and heat are shown for the ohmic control and the NANOR®-type component. This experimental run of a M-NANOR®-type component was made several hours after a single application sequence of the fractionated magnetic field was delivered. There was no additional H-field applied for this figure. The peak applied voltage was ~125 V. Note the absence of an exponential or linear fall-off of peak activity.

in incremental power gain and excess energy gain, over ordinary CF/LANR. This magnetization sequence created an increase of ca. 4–10 times the peak power gain over conventional LANR with the same system. The peak power gain of such treated NANOR®s ranged from 22 to up to ~80 times input electrical power or more beyond the control, as determined by calorimetry [4,10,11].

There are also subsequent effects (occurring later, or metachronous) and strong evidence for the first ever-observed two (2) optimal operating point (OOP) manifolds [4]. Some of these dramatic changes can be seen in Fig. 3, which shows the first evidence of magnetic rejuvenation of nanostructured CF/LANR material, and even increasing the CF/LANR activity to higher levels than observed initially!

Figure 3 shows a calorimetric presentation of the ohmic control and the NANOR®-type component. It demonstrates the impact of the magnetic field, with no change from the same magnetic field on the background or control. In Fig. 3, the magnetic field intensity was applied only at one point in time which is indicated by the black arrows. At all other points in time, there was NO additional applied magnetic field intensity. Note the synchronous amplification of the M-NANOR® power output induced by the magnetic field. This is not seen in the ohmic control.

#### 3.2.3. *Metachronous magnetically induced increased energy gain*

Other effects were noted. Astonishingly, after the single application of the fractionated large applied magnetic field intensity was delivered at one point in time (between the arrows), there is improvement in the CF/LANR activity which also appears later – long after the initiation of the magnetization [4]. This metachronous impact wrought upon the treated CF/LANR M-NANOR®s, long after the treatment, is heralded as increased power and energy gain as determined by delta-$T/P_{\mathrm{in}}$, delta-HF/$P_{\mathrm{in}}$, and calorimetry. Subsequent, metachronous effects are those physical changes wrought by the applied high intensity fractionated magnetic field *after* the field was applied.

Figure 4 is a calorimetric presentation of a different run later many hours after the single application of the fractionated large applied magnetic field intensity was delivered. In Fig. 4, many cycles are shown which demonstrated clearly that there was more output than the ohmic control, and as astonishingly, there is improved activity which is shown here to be metachronous and long-lasting. Notice that the peak power gain of the M-NANOR®-type component is increased *after* the application of the fractionated large applied magnetic field intensity.

#### 3.2.4. *Magnetically induced activity has an oscillation of activity*

There are other remnant effects long after the application of the H-field. These late-appearing effects include an increased, but variable, activity. The subsequent activity of the magnetized M-NANOR®-type components no longer decreases in a simple regular, evanescent manner over time (as described in previous publications [1–5]); but instead appears irregular with a periodic component, as first seen in Fig. 3 and also shown in Fig. 4. The cyclic component of the activity in in the range of circa $1.3 \times 10^{-4}$ Hz ($0.2–5 \times 10^{-4}$ Hz).

#### 3.2.5. *Magnetically induced unique dual optimal operating manifolds (OOPs)*

Although not covered in detail here, previously, all CF systems and the NANOR®s had shown a single optimal operating point manifold for excess heat operation, $^4$He production, and other products [15,14,4]. Today, that is no longer accurate. Even after a single treatment to a high intensity fractionated magnetic field, there arise two OOP manifolds. The new OOP is elicited at higher input electrical power, and so the new, second, OOP is located to the "right" of the conventional, first, CF/LANR OOP [4]. Although this revelation is far beyond the scope of this paper, its impact is very important because magnetically activating preloaded nanostructured CF/LANR devices is both very useful [4] and instructive [8]. Although cold fusion (LANR) has a first stage mediated by phonons within the loaded

lattice by coherent Phusons [18], there is also a magnetically coerced second stage, which we believe may be mediated by magnons, or interactions of phonons in H-field and included magnetization field.

## 4. Interpretation

### 4.1. Possible implications of magnetized domains

The unique temporal changes, shown in Figs. 3 and 4, and the amplification of CF/LANR excess heat by fractioned magnetic fields effects suggest a new CF/LANR material science/nuclear interaction. The analysis below is thus important because the magnetic domains, magnetic interactions, magnetically increased incremental power gain, might be relevant to other materials and other systems.

### 4.2. Magnetism in $ZrO_2$–Pd/Ni and $ZrO_2$–Pd components

How can palladium become magnetic? Nickel is ferromagnetic and the induction of magnetization is to be expected. So this is expected for the nickel-containing NANOR®s, but it is somewhat surprising for the palladium M-NANOR®s. However, palladium like platinum, has potential capacity as an exchange-enhanced paramagnetic materials to exhibit a strong Stoner enhancement and become ferromagnetic upon tension [19]. When the Stoner criterion is satisfied, in response to external stimuli such as applied E-field, the materials can exhibit unconventional magnetic responses – they become exchanged-enhanced ferromagnetic.

Thus, the solid state metallurgical lattice of Pd can become ferromagnetic or its equivalent post-magnetization. This has now been seen [20] and confirmed in magnetic domain scanning and imaging which will be the subject of an upcoming paper (cf. also Fig. 5).

The magnetization and oscillations may also be consistent with other reports of quantum oscillations in several systems, including metallic triangular-lattice antiferromagnet $PdCrO_2$ [21], and as seen in the (electrically tunable) anomalous Hall effect observed in platinum thin films [22], as seen with both lattice and magnetic oscillations in stacks of Josephson junctions [23], and with reports of excess energy production with high voltage magnetic pulses coerced through nanograined magnetic materials such as strontium ferrites [24]. The coerced magnetization is important and may also be consistent with some of those materials considered theoretically in investigations using DFT calculations of strained ferromagnetic lattices [25].

### 4.3. Interaction forces between magnetized domains

It is important to consider the material science and metallurgy of this new magnetic behavior and material(s) (Fig. 5). From what do the domains arise, and how do they interact. How can the magnetic domains couple and account for the unusual time-variant activity? Magnetic materials can self-interact, as described by the Langevin function [26]. Theoretically, this is supported by density-functional calculations [27]. Most interestingly, this appears to be driven by vacancies in Pd (theoretically, up to 15% calculated using the SCR Korringa–Kohn–Rostoker coherent potential approximation method, which predicts a magnetic moment at ~10% vacancies) [28]. Attention is drawn to the interesting fact that several theories of cold fusion also require vacancies [29].

## 5. New Hypothesis. Is Oscillation of Activity Linked to Magnetized Domains

The continuum electromechanical equations may give a possible new understanding of the just-discovered time-varying activity change that appears in post-magnetized components [4]. This is important because these changes are uniquely different from observations of hundreds of runs on scores of samples. These M-NANOR®-type components have responded markedly differently, requiring this attempt to mathematically analyze, and possibly explain, this

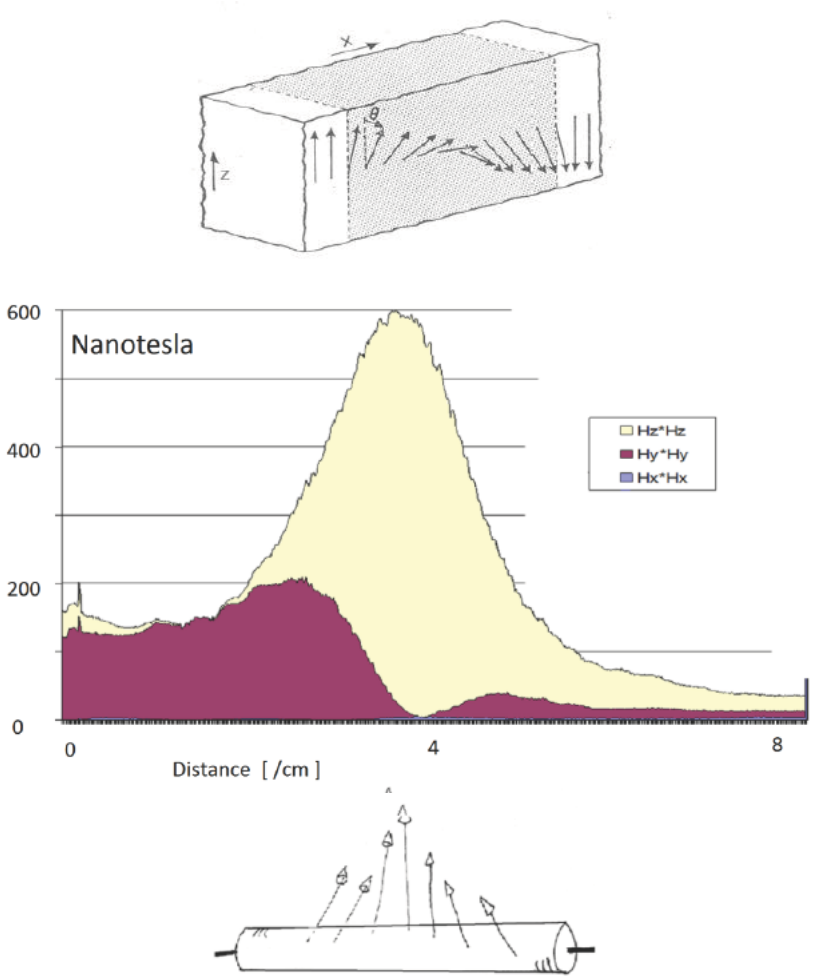


**Figure 5.** Magnetic Domains in NANOR®-type components. (*top*) Schematic showing magnetic domains interacting within a lattice. The magnetization is observed changing over a distance (after John Mara and A.von Hippel [32]. (*bottom*) These magnetic domains have been observed experimentally and their imaging, and possible implications, are the focus of a manuscript [20]. The graph shows the vectorial scanned magnetization from the domain (in nanotesla) as a function of distance along the long axis of the M-NANOR® 7-8 at rest, long after it was previously operated. The square of each of the $x$-, $y$-, and $z$-axis components are shown as a function of $x$-axis. (*bottom inset*) Estimated vectorial magnetization along, and just vicinal to, the body of M-NANOR® 7-8.

new post-magnetization observation. The activity oscillations observed in the output excess power of M-NANOR®-type components long after their magnetic field interaction must result from the applied magnetic field intensity. So what is the impact of the H-field on any magnetic domains there? We have begun to measure them in M-NANOR®s after magnetization [20] as shown in Fig. 5.

In this report, we examine the behavior of the oscillating excess heat activity of magnetized M-NANOR®-type components, and attempt to link that behavior to loco-regional magnetic domains in the treated coerced lattice to

understand the very unique observed responses of these magnetically treated components. Although better models for, and a solution to, this observation are needed, this is a first approximation.

These domains can be modeled as a remnant magnetization of the lattice, and here are taken into account through the forces and tension they incur through the density of the lattice and Poisson's ratio. Specifically, using the findings of strained layer ferromagnetism in transition metal, it is found that tension increases magnetization and simultaneous should decrease density [25], and these may be the conditions that give rise to the activity oscillations.

## 6. New Results. Magnetic Forces and Oscillations from CF/LANR Domains

To model the interactions of two neighboring magnetic domains, we assume that in addition to the normal mechanical restoring forces that there are also electromechanical forces. We begin the analysis with Newton's equation, using a continuum model using a simple spring constant equation for the initial analysis.

$$\frac{\mathrm{d}^2 x}{\mathrm{d}t^2} = \frac{F}{M}. \tag{1}$$

The magnitude of the restoring force is derived using Hooke's law augmented by the Maxwell stress tensor which is integrated over the surface boundary between those two magnetic domains to derive the volume-integrated induced force [30–32].

The force density, in integral and differential forms, thus becomes

$$\int_V \left[ -\frac{1}{2}\mathbf{H}\cdot\mathbf{H}\nabla\mu + \nabla\left(\frac{1}{2}\mathbf{H}\cdot\mathbf{H}\frac{\partial\mu}{\partial\rho}\rho\right) - \mathbf{F}\right]\cdot\delta\xi\,\mathrm{d}V = 0, \tag{2}$$

$$\mathbf{F} = -\frac{1}{2}\mathbf{H}\cdot\mathbf{H}\nabla\mu + \nabla\left(\frac{1}{2}\mathbf{H}\cdot\mathbf{H}\frac{\partial\mu}{\partial\rho}\rho\right). \tag{3}$$

Therefore, the force, and the stress tensor, would there be, and derived as follows:

$$F_{\mathrm{m}} = \frac{\partial T_{mn}}{\partial x_n}, \tag{4}$$

$$T_{mn} = \mu H_n H_m - \frac{1}{2}\delta_{mn} H_k H_k \left(\mu - \frac{\partial\mu}{\partial\rho}\rho\right). \tag{5}$$

Note the magnetoelectric term at the end (reminiscent of electrical dielectrophoresis). Substitution in the original equation, with terms including magnetostriction, gives

$$M\frac{\mathrm{d}^2 x}{\mathrm{d}t^2} = -\left[\mathrm{K}\ \times\ \mathrm{x}\right] - \frac{[Bo]^2}{2\times\mu^2}\left[\Delta\mu + \left[(-\Delta\rho)\left(\frac{\delta\mu}{\delta\rho}\right)\right]\right]. \tag{6}$$

The solution has an amplitude of

$$\frac{[Bo]^2}{2V\rho\mu^2 K\sqrt{(\omega_0^2-\omega^2)}}\left[\Delta\mu + \left[(-\Delta\rho)\left(\frac{\delta\mu}{\delta\rho}\right)\right]\right] \tag{7}$$

and a natural frequency of

$$\omega_0 = \sqrt{\frac{K}{\rho V}}. \tag{8}$$

This might be the resultant natural frequency which we see in the M-Nanor®'s excess energy cyclic activity (cf. Figs. 3 and 4).

## 7. Conclusion. Oscillating Activity and Magnetic Domains

There are two types of NANOR®-type CF/LANR components. They have very different behavior. The post-magnetization effects are significant and time-variant because it has now been discovered that high intensity, dynamic, repeatedly fractionated, magnetic fields have an incremental major, significant and unique, complex, metachronous amplification effect on preloaded M-NANOR®-type LANR devices.

Furthermore, in contrast to previously observed exponential falloffs of sample activity (peak incremental excess power gain), post-magnetization activity demonstrates oscillatory activity, and the Maxwell stress tensor heralds a theoretical frequency for oscillations now observed to exist between these magnetic domains in these magnetized NANOR®-type components. The observed frequencies of activity change observed appear be circa $1.3 \times 10^{-4}$ Hz (range 0.2–5 $\times$ $10^{-4}$ Hz).

This paper's analysis of the force density, calculated by using the Maxwell stress tensor, predicts oscillations now observed to exist between these magnetic domains in these magnetized NANOR®-type components. This analysis indicates that magnetic interactions between domains should augment other restoring forces, and that the frequency should increase with decreasing mass, and increasing applied magnetic field intensity (presumably until coercion effects elicit no further increase). It is important to consider this new material science and metallurgy with surprising new magnetic behavior in future analyses and experiments.

## Acknowledgments

The author acknowledges and thanks Gayle Verner and Alex Frank for their very helpful editorial support. The author is grateful to and thanks the teams who have helped collect the data, support the work, and have helped better understand the physics and materials with their assistance, ideas and suggestions including Richard Goldbaum, Jeffrey Tolleson, Gayle Verner, Leslie Wright, Linda Hammond, Alex Frank, Alan Weinberg, Charles Entenmann, Allen Swartz, Joshua Gyllinsky, Peter Hagelstein, Florian Metzler, Brian Ahern, Jeff Driscoll, Dennis Cravens, Pamela Mosier Boss, Lawrence P.G. Forsley, Frank Gordon, Louis DeChiaro, and Dennis Letts. This effort was supported by JET Energy Inc. and the New Energy Foundation. NANOR® and PHUSOR® are registered trademarks of JET Energy, Incorporated. NANOR®-technology, and PHUSOR®-technology are protected by U.S. Patents D596724, D413659 and several other patents pending.

## References

[1] M.R. Swartz, G. Verner, J. Tolleson and P. Hagelstein, Dry, preloaded NANOR®-type CF/LANR components, *Current Sci.* **108** (4) (2015) 595.

[2] M.R. Swartz and P.L. Hagelstein, Demonstration of energy gain from a preloaded $ZrO_2$–PdD nanostructured CF/LANR quantum electronic device at MIT, *J. Condensed Matter Nucl. Sci.* **13** (2014) 516. www.iscmns.org/CMNS/JCMNS-Vol13.pdf.

[3] M.R. Swartz and P.L. Hagelstein, Demonstration of energy gain from a preloaded $ZrO_2$–PdD nanostructured CF/LANR quantum electronic device at MIT, *J. Condensed Matter Nucl. Sci.* **13** (2014) 516. www.iscmns.org/CMNS/JCMNS-Vol13.pdf.

[4] M.R. Swartz, G.M. Verner, J. Tolleson, L. Wright, R. Goldbaum and P.L. Hagelstein, Amplification and restoration of energy gain using fractionated magnetic fields on $ZrO_2$–PdD nanostructured components, *J. Condensed Matter Nucl. Sci.* **15** (2015) 66. www.iscmns.org/CMNS/JCMNS-VoI15.pdf.

[5] M.R. Swartz, Incremental high energy emission from a $ZrO_2$–PdD nanostructured quantum electronic component CF/LANR, *J. Condensed Matter Nucl. Sci.* **15** (2015) 92. www.iscmns.org/CMNS/JCMNS-Vol15.pdf.

[6] M.R. Swartz, G. Verner, J. Tolleson, L. Wright and R. Goldbaum,, Imaging of an active NANOR®-type LANR component using CR-39, *J. Condensed Matter Nucl. Sci.* **15** (2015) 81. www.iscmns.org/CMNS/JCMNS-Vol15.pdf.

[7] M.R. Swartz, P.L. Hagelstein and G. Verner, Impact of electrical avalanche through a $ZrO_2$–NiD nanostructured component on its incremental excess power gain, ICCF-19, *J. Condensed Matter Nucl. Sci.* **19** (2016) 287–297.

[8] M.R. Swartz, Detection of phonon gain from a NANOR®-type CF component (2016, in preparation and review).

[9] M.R. Swartz and G. Verner, Excess heat from low electrical conductivity heavy water spiral-wound Pd/$D_2O$/Pt and Pd/$D_2O$-$PdCl_2$/Pt devices, *Condensed Matter Nuclear Science, Proc.ICCF-10*, World Scientific, Singapore, ISBN 981-256-564-6, 29-44; 45–54 (2006).

[10] M.R. Swartz, Excess power gain using high impedance and codepositional LANR devices monitored by calorimetry, heat flow, and paired stirling engines, *Proc. ICCF14* **1** (2008) 123; ISBN: 978-0-578-06694-3, 123 (2010). www.iscmns.org/iccf14/ProcICCF14a.pdf.

[11] M.R. Swartz, Survey of the observed excess energy and emissions in lattice assisted nuclear reactions, *J. Scientific Exploration* **23**(4) (2009) 419–436.

[12] J. Marwan, M.C.H. McKubre, F.L. Tanzella, P.L. Hagelstein, M.H. Miles, M.R. Swartz, E. Storms, Y. Iwamura, P.A. Mosier-Boss and L.P.G. Forsley, A new look at low-energy nuclear reaction (LENR) research: a response to Shanahan, *J. Environ. Monit.* **12**(9) (2010) 1765–1770.

[13] M.R. Swartz, G. Verner, A. Frank and H. Fox, Importance of non-dimensional numbers and optimal operating points in cold fusion, *J. New Energy* **4** (2) (1999) 215–217.

[14] D. Cravens, Factors affecting success rate of heat generation in CF cells, *Proc. ICCF-4*, Maui, Hawaii, July 1994, pp. 18-1 through 18-14.

[15] S. Szpak, P.A. Mosier-Boss and F.E. Gordon, Further evidence of nuclear reactions in the Pd/D lattice: emission of charged particles, *Naturwissenschaften* **94** (2007) 511–514.

[16] M.R. Swartz, Impact of an applied magnetic field on the electrical impedance of a LANR device, *JCMNS*, Volume 4, *Proc.,* March 2010, New Energy Technology Symposium held at the 239th American Chemical Society, San Francisco, 2011.

[17] J. O'M. Bockris, R. Sundaresan, D. Letts and Z.S. Minevski, Triggering and structural changes in cold fusion electrodes, *Proc. ICCF4*, Maui, Hawaii, July 1994, 1–46.

[18] M.R. Swartz, **P**husons in nuclear reactions in solids, *Fusion Technol.* **31** (1997) 228–236.

[19] D.L.R. Santos, P. Venezuela, R.B. Muniz and A.T. Costa, Spin pumping and interlayer exchange coupling through palladium, *Phys. Rev*. B **88** (2013) 054423.

[20] M.R. Swartz, Scanning vector magnetometry of NANOR®-type components, in preparation.

[21] J.M. Ok, Y.J. Jo, K. Kim, T. Shishidou, E.S. Choi, H.J. Noh, T. Oguchi, B.I. Min and J.S. Kim, Quantum oscillations of the metallic triangular-lattice antiferromagnet $PdCrO_2$. 3. *Phys Rev Lett.* (2013);111(17):176405 (2013).

[22] Shimizu Sunao, Kei S. Takahashi, Takafumi Hatano, Masashi Kawasaki, Yoshinori Tokura, and Yoshihiro Iwasa, Electrically tunable anomalous hall effect in Pt thin films*, Phys. Rev. Lett*. **111** (2013) 216803.

[23] Lattice configurations and magnetic oscillations in stacks of Josephson junctions, http://mti.msd.anl.gov/homepages/koshelev/projects/mag-osc.htm.

[24] Brian Ahern on the late Arthur Manelas; personal communication (2015).

[25] Louis DeChiaro, L. Forsley and P.A. Mosier-Boss, Strained layer ferromagnetism in transition metals and its impact upon low energy nuclear reactions, *J. Condensed Matter Nucl. Sci.* **17** (2015) 1–26.

[26] Shimizu, Sunao, Kei S. Takahashi, Takafumi Hatano, Masashi Kawasaki, Yoshinori Tokura and Yoshihiro Iwasa, Electrically tunable anomalous Hall effect in Pt thin films, *Phys. Rev. Lett.* **111** (2013) 216803.

[27] Y. Sun, J.D. Burton and E.Y. Tsymbal, Electrically driven magnetism on a Pd thin film, *Phys. Rev.* B **81** (2010) 064413.

[28] N. Takanol, T. Kai, K. Shiiki and F. Terasakil, Effect of copious vacancies on magnetism of Pd, *Solid State Commun.* **97**(2) (1996) 153–156.

[29] M.R. Swartz and P.L. Hagelstein, Transient vacancy phase states in palladium after high dose-rate electron beam irradiation, *J. Condensed Matter Nucl. Sci.* **14** (2014) 50.
[30] J.R. Melcher, *Continuum Electromechanics*, MIT Press, Cambridge, 1981. ISBN-10: 026213165X; ISBN-13: 978-0262131650.
[31] H.H. Woodson and J.R. Melcher, *Electromechanical Dyanamics*, Wiley, New York, 1968.
[32] A.R. von Hippel, *Molecular Science and Molecular Engineering*, MIT Press, Cambridge, 1959.

J. Condensed Matter Nucl. Sci. 22 (2017) 47–52

Research Article

# Development of a Cold Fusion Science and Engineering Course

Gayle M. Verner and Mitchell R. Swartz*

*JET Energy Inc., Wellesley Hills, MA 02148, USA*

Peter L. Hagelstein

*Research Laboratory of Electronics, Massachusetts Institute of Technology, Cambridge, MA 02139, USA*

**Abstract**

For three consecutive years, an introductory non-credit short course was taught on the science and engineering of cold fusion (CF). It reviewed its origin, extent, basis and substantial experimental proof of the observed excess energy (XSE) from active cold fusion (lattice assisted nuclear reactions) systems. The range of CF technologies spanned from early aqueous CF/LANR systems to recent day nanomaterials. While academic officials are slow to recognize cold fusion and its viability, the fact is that the subject and its science have entered the academic domain, and students can learn that the phenomenon is real and reproducible.
 ISSN 2227-3123

*Keywords:* CF academic course, CF curriculum, CF education, CF training, LANR academic course, LANR education, LENR academic course, LENR education

## 1. Introduction

Education plays a critical role in the development of any science and technology, and it is especially significant in an emergent, controversial field like cold fusion. What heightens its difficulty here, however, is that the scientists and others interested in learning more about the field are almost always under an intense barrage of unfair criticism and blistering attacks from competing interests and skeptics. Despite this major obstacle, just as it has been important to have occasional cold fusion open demonstrations, it is important to create (and expand) cold fusion education in the classroom.

This report describes how a complicated and new alternative energy subject-matter was tailored to a college course-work program, and was offered as an introduction to cold fusion during its Independent Activities Period (IAP), designed for students to engage in topics outside-of the-normal-curriculum.

*Dr. Mitchell R. Swartz ScD, MD, EE, E-mail: education@nanortech.com.

 ISSN 2227-3123

## 2. Experimental

The goal has been to increase the number of well-trained cold fusion scientists, researchers and theoreticians by introducing a range of material science, physics and engineering to them with the hope of expanding awareness, educational excellence, and the science and technology needed to develop and proceed with this energy-efficient technology. Enrollment was open with permission from the instructors, Prof. Peter Hagelstein, PhD, MIT Professor of Electrical Engineering and Dr. Mitchell Swartz, ScD, MD, of JET Energy Inc. IAP at MIT, for those not familiar with it, is a special four-week program where students can choose from a vast array of non-credit and for-credit short coursework offered only during the month of January of each year. CF-101 was a non-sign up, non-credit introductory course open, to MIT and non-MIT students, alike, as well as the public. The CF/IAP classes generally extended over two weeks.

A brief summary of the content was published in *Current Science* [1], and this paper goes considerably further to enable and encourage others to adopt and expand the curriculum. Here is the scope of what was covered during January, 2013. Prof. Peter Hagelstein began with an overview of how cold fusion began, its science, the structure, materials and output of the Fleischmann/Pons (F/P) effect, and skeptics' arguments. He reviewed the origin, extent, and basis of the observed excess energy (XSE) from active CF/LANR systems. He spoke about the roles of palladium, palladium hydrides (palladium filled (aka "loaded" with an isotope of hydrogen), and the method/difficulties of metals actually loading with hydrogen. He then clearly detailed some of the exact reasons why F/P succeeded whereas so many "good scientists from good laboratories" could not initially replicate their experiments in the early 1990s. Generally, they were unable to achieve the requisite highly loaded palladium, which is unconditionally required for achieving active, deuterium fusion which is the desired cold fusion effect.

Prof. Hagelstein explained that the big issue was that the experiments were attempted at the "best" labs by very good scientists, and they were not able to confirm it; that the effect itself is unexpected, and in contradiction with what would be expected from condensed matter physics and from nuclear physics. One member of the class pointed out that even the Harwell data clearly demonstrated a 10–15% excess power during the portion of the run shown. Prof. Hagelstein explained that such a small amount was insufficient for them (as were the bursts of excess energy in only the heavy water side of their setup). Like the other famous groups, they too, could not report positive results. This report describes how a complicated and new alternative energy subject-matter was tailored to a college course-work

**Figure 1.** Students and interested researchers develop their science and engineering skills about cold fusion, isotopic loading of metals, and calorimetry during the "Introductory Cold Fusion IAP Course" offered at MIT in 2013 (photocredit: Gayle Verner).

program, and was offered as an introduction to cold fusion during its Independent Activities Period (IAP), designed for students to engage in topics outside-of the-normal-curriculum (Fig. 1).

To understand how success was achieved, Prof. Hagelstein then moved the discussion along to kinetic issues involving the loaded/loading palladium deuteride (PdD) lattice, including its dynamic structure and the roles of lattice expansion. He clarified how deuterium goes in via the Volmer reaction, and out via the Tafel reaction and through cracks. In "good" cathodes, the internal leaks are minimized, which can reduce the level of internal leaks by more than 1000. At ENEA, Frascati, Violante, and his team anneal to samples, so as to get grain sizes on the order of the foil thickness, which, thus, minimizes internal leaks. To further underscore the importance of adequate loading, Hagelstein also referred to the SRI experiments which showed that excess heat *only* appeared when the loading ratio was, at least in, or above, the 0.85–0.9 range. Also supporting the need for high loading, he discussed the results of the Energetics group from Israel, who have used the Dardik-discovered Superwave.

Prof. Hagelstein proposed conditions under which deuterons in the metal are stabilized (or not), and how $^{4}$He* might form for its nanosecond of existence in the metal. Since the electron density is too high, there is no site in the lattice where fusion can occur, except possibly at vacancies, where the electron density is lower. Because vacancies are actually stabilized with H or D addition, at a loading of 0.95 near room temperature, so vacancies then become thermodynamically preferred. Supporting that, since vacancies diffuse very slowly, they are also made on new surfaces, which is done by codeposition, he said. In the codeposition experiments, (going back decades) excess heat turns on within an hour after initiating codeposition. Later, he spoke of activation of CF/LANR and detailed the Dennis Letts' laser "beat frequency" terahertz region experiments which activate the desired reactions.

On Wed., January 23, Prof. Hagelstein explained how the loaded palladium hydride lattice, with sufficient flux and activation energy, is able to highly overcome the Coulomb barrier and then "chop up" the 24 MeV energy of freshly made helium (the so-called excess energy) into smaller energy quanta which the phonons (lattice vibrations) can then deliver coherently, in tandem, to the lattice. This enables the excess heat production in F/P and (variant) CF/LANR experiments.

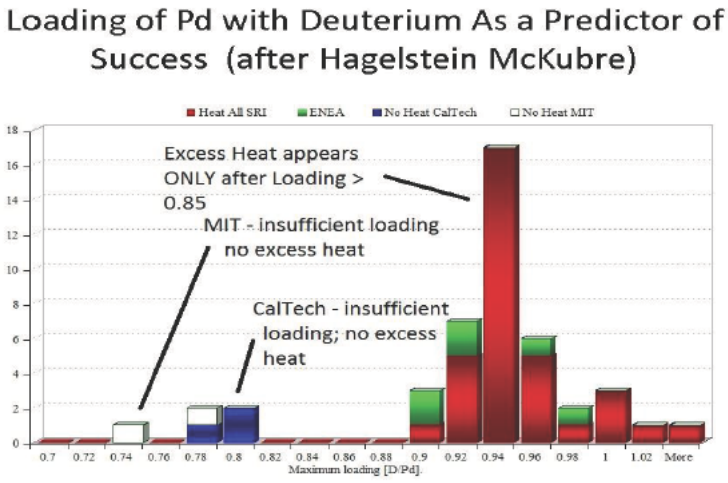


**Figure 2.** The success of cold fusion experiments has generally depended upon the loading achieved of the Group VIII metal. This is because in cold fusion, excess heat *only* appears when the loading ratio is very high. This graph shows that with increased loading (right-hand side of the data) there was historically a much greater likelihood of having seen cold fusion's excess heat.

Dislocations and cracks in the average cathode generate many pathways that include many internal leaks. These can become "superhighways" of hydrogen loss, can appear suddenly, and can end active samples, as they reduce stress internally. Generally, they were unable to achieve the requisite highly loaded palladium, which is unconditionally required for achieving active, deuterium fusion which is the desired cold fusion effect (Fig. 2).

On Thursday, Jan. 24th, Prof. Hagelstein continued about the several meticulous experiments which documented that helium ($^4$He) is made as the product of cold fusion from the deuterium which is loaded at very high levels into the palladium lattice. He showed this for three sets of experimenters including Dr. Mel Miles at the US Navy, and Dr. Len Case (working independently) from N.H., and at SRI in Calif., where it was also measured.

Prof. Hagelstein said that even the rate of helium production is also commensurate with observed excess power of cold fusion experiments, as was reported years ago in Italy by Gozzi. Furthermore, he said, regarding $^4$He measurements that Bush and Miles demonstrated it was there; Gozzi showed that it was correlated in time with the excess power; SRI provided important confirmations, but beyond that they made the best measurement in his view of the $Q$-value. The issue is that some of the He is retained in the PdD (which was obvious from the Gozzi experiment).

One class attendee asked why there were not more of these experiments done. Prof. Hagelstein quickly pointed out that helium measurements are difficult because of both atmospheric contamination and confusion with materials of similar mass (that is $D_2$), and that meticulous efforts are required to shield the experiments from the atmosphere (by metal flasks, for example) and that expensive equipment is required to make the discriminating measurements required.

As a result, this type of work is very hard to do, he said, and expensive, and simply put, there has not been enough funding.

He also talked about the problem of helium occupancy at important choke-points in the lattice which must be empty as required for active, excess heat-producing, cold fusion systems. He proposed that the big advantage that the NANOR®-type CF/LANR components (JET Energy's) have is that the helium does not have to diffuse very far, so that the power level can be much higher.

Prof. Hagelstein discussed the activation energy required to get the desired reactions. He went through the data of several experimenters in the field including Dennis Cravens, who demonstrated observation of heavy water cells increasing output with a temperature rise. Hagelstein then followed that up with corroboration from other experimenters, including early recognition of this effect, an increase in excess power in time following a brief temperature rise (usually due to a calibrating pulse), as was seen by Fleischmann, Storms and Swartz.

Regarding activation energy, Prof. Hagelstein discussed the Dennis Letts laser experiment which activates specifically required, key phonon modes in the lattice – compressional optical phonon modes when the beat frequency is around 8.5 THz, and compressional optical phonon modes when the beat frequency is ~16 THz.

Prof. Hagelstein introduced the cold fusion/LANR Hamiltonian and the role of orbitals of hydrogen. Next, he related to the Hamiltonian he developed to also include the roles of deuteron flux through, and loading into, the palladium citing work by Mitchell Swartz and Akito Takahashi. He then explained how Corkum's mechanism led him to further understand his own, developing spin boson model which was derived from the work of Cohen–Tannoudji, and which explained how the 24 MeV from the $^4$He* is chopped up into tiny amounts, and then delivered to the loaded palladium lattice. This is where there is then the appearance of the "excess heat" as the excited helium ($^4$He*) returns to its own ground state ($^4$He) as the energy is converted to THz phonons, and then thermalized to produce that heat.

Hagelstein's Take Away Message is that the lattice is key, and the physicist's theories are really not inconsistent with cold fusion, after all. He demonstrated exactly where it was insufficient to explain CF/LANR in the absence of his later discovery of the role of destructive interference and other loss and dephasing issues. Those loss mechanisms occur in the real loaded lattice.

On Friday, Prof. Hagelstein focused on the mathematical models and physical models for coherent energy exchange under conditions of fractionation, and on the Karabut collimated X-rays, which appears to show this effect, and expanded his CF/LANR Hamiltonian to now include coupling parameters.

Prof. Hagelstein continued with relativistic physics. Examination of the very strong coupling between the center of mass momentum and internal nuclear degrees of freedom is normally eliminated by a generalized Foldy–Wouthuysen rotation. However, under conditions of destructive interference such as in the lattice filled with lossy bosons, it does not appear appropriate. The Take Away Message was that his corrected condensed matter nuclear science (CMNS) Hamiltonian with all the additions is finally becoming very close to describing accurately what is actually being observed in CF/LANR

After a weekend break, lectures resumed on Mon., Jan. 28, led by Dr. Mitchell Swartz. He continued the talk regarding substantial experimental proof for cold fusion (lattice assisted nuclear reactions). Dr. Swartz presented what many consider the well-researched, evidence for existence (and development) of cold fusion in an understandable four plus hours (two each day) of scientific detail, not only reviewing decades of CF/LANR experiments but also presenting many how-to's of the successful processes.

He then shifted to hot fusion which unfortunately has a long history of technical and engineering failures. By contrast to hot fusion, cold fusion does not make any significant amount of dangerous radiation, he said, nor does it make other materials radioactive. It has zero carbon footprint. It could change everything.

He then discussed yet another reason why CF/LANR is so important – its energy density. He directed the class to the hard facts that the helium ($^4$He) production is in quantitative agreement with the XSE, as Mel Miles, Case, and SRI had measured; and that the rate of He4 production is commensurate with the power, as the Gozzi experiment had demonstrated.

Dr. Swartz continued, talking about the materials involved in CF/LANR. He taught how loading is achieved with either an applied electric field intensity acting upon water, separating out the deuterium, which with palladium, comes from the surrounding heavy water.

In the next session, after Dr. Swartz surveyed the methods of calibration of heat-producing reactions and systems, he detailed how there are now available many types of controls, time-integration, thermal waveform reconstruction, noise measurement and additional techniques, which are used, and is needed, for verification.

He then spoke at great length of the importance of the role of deuteron flow (flux) and explained the differences between flow calorimetry which can be inaccurate under some conditions where it is not calibrated, and the preferred methods of measuring excess energy. Having discussed the materials, and methods of measuring excess energy accurately, he segued to many examples of actual excess heat generated by a variety of CF/LANR systems. He showed graphs that were derived, using aqueous nickel and palladium systems.

Dr. Swartz returned to the concept of deuteron flux. Then using the Navier–Stokes equation, he developed the flow equations for both protons and deuteron flow in "conventional" cold fusion and in its variant, codeposition, where there is also flux of the palladium ions into the cathode which builds up a loaded compartment of active material. The concept of deuteron flux then led to metamaterials, a major improvement of CF systems. He focused on the salient advantages of the LANR metamaterials with the PHUSOR®-type system, stating that it is one prime, extremely useful, example with high output.

Dr. Swartz then shared another of his discoveries – Optimal Operating Point (OOP's) manifolds that organize CF/LANR output by the amount of input power. He explained how he discovered the OOP experimentally and showed how in all CF/LANR systems, no matter what the product (helium4, heat, or tritium production), and no matter what the system (palladium with heavy water, nickel with ordinary water, and nanomaterials) all of these when plotted as a function of input power demonstrate a series of dots which assemble and show a distinct pattern.

He went through the different regions, and showed where the reactions turn on and off, and how by plotting out the experiments this way, one could show consistency and reproducibility, time and time again. He demonstrated that OOP operation has shown the ability to determine the products of CF/LANR, and why OOP manifolds demonstrate that CF is a reproducible phenomenon, applicable to science and engineering. He also said that he had found OOPs in other colleague's experiments where they had not, and showed that their data also fit these curves.

Returning to the experimental results and engineering methods developed to control cold fusion, he then surveyed "heat after death" and its control for several useful applications, including the use of CF/LANR systems to drive motors. The important Take Home Point, he said, was that there is an extraordinary amount of data and information from it that has been collected over the years.

Emissions and energy derived from CF systems is how Dr. Swartz led the lecture on Tues., Jan. 29, 2013. He continued with the discussion of experimental results, now beginning with the near infrared emissions from active LANR devices, and the use of CF/LANR engines to generate electricity.

He finally focused the class from aqueous cold fusion to the nanomaterials in CF/LANR, now holding worldwide intrigue. Of particular interest was his discovery of a new type of dry and preloaded nanomaterials, a CF/LANR material which is producing phenomenal excess heat output.

After discussing these novel characteristics and electrical breakdown (avalanche) issues, which electric drive regions actually generate excess energy, he presented the development of several types of the NANOR®-type CF electronic components. He concluded with introduction to advanced driving circuits that were shown to have excess energy documented by temperature rise, heat flow, and calorimetry; heralding their revolutionary potential to change the energy landscape in circuits, distributed electrical power systems, artificial internal organs, propulsion systems, space travel, and more.

## 3. Results

According to the participants, the course was a success. At the beginning of the two week course, Room 4-153 in the Electrical Engineering building was nearly packed with a blend of about 35–40 students, as well as entrepreneurs, engineers, physicists, and "curious" members of the community, as the class size ebbed and flowed throughout the six-day event. Attendees came from as far away as Spain, China, Germany, and Switzerland. But they also traveled from California, Pennsylvania, New York, and throughout Massachusetts. Many said the course was "great" and reported also they were glad they came. If others disapproved, no one said so publicly.

## 4. Conclusion

While MIT officials still reportedly do not recognize cold fusion or its viability, the fact that it has entered the academic domain, albeit through the less-structured IAP agenda, is certainly noteworthy, both for those scientists working for its public acknowledgement and for the appearance of a place to go and get an education in this field. Twenty-seven years later, one can now walk into an MIT classroom, listen to academic lectures on the subject, and learn that the phenomenon is real and reproducible. And while it is still controversial, cold fusion seems to have found a fit, albeit tight, in the academic world.

## References

[1] G. Verner, M. Swartz and P.L. Hagelstein, Summary report: 'Introduction to Cold Fusion'–IAP course at the Massachusetts Institute of Technology, *Current Science* **108**(4) (2015) 653. http://www.currentscience.ac.in/Volumes/108/04/0653.pdf.

J. Condensed Matter Nucl. Sci. 22 (2017) 53–73

Research Article

# Probabilistic Models for Beam, Spot, and Line Emission for Collimated X-ray Emission in the Karabut Experiment

Peter L. Hagelstein*

*Massachusetts Institute of Technology, Cambridge, MA, USA*

**Abstract**

Collimated X-ray emission near 1.5 keV in the Karabut experiment is an anomaly that cannot be explained by conventional solid state, atomic, or nuclear physics. In order for the X-rays to be collimated, there must either be an X-ray laser present, or else a phased-array collimation effect produced by emitting dipoles that radiate in phase. Although there have been arguments made in support of an X-ray laser origin of the effect, from our perspective this approach suffers from an absence of a plausible mechanism, short excited-state electronic lifetimes, high power requirements, and an incompatibility between the experimental geometry and the need for an elongated laser medium for beam formation. In this work we consider a model for beam formation due to many emitting dipoles randomly positioned within a circle on a mathematically flat surface. When the emitting dipole density is low, a speckle pattern is produced. Above a critical emitting dipole density beam formation occurs. The average intensity of the speckle and beam is estimated from simple statistical models at low and high dipole density, and combined to develop an empirical intensity estimate over the full range of dipole densities which compares well with numerical simulations. Beam formation occurs above a critical number of emitting dipoles, which allows us to develop an estimate for the minimum number of emitting dipoles present in the Karabut experiment. The effect of surface deformations is considered; constant offsets do not impact beam formation, and locally linear offsets direct the beam slightly off of normal. Minor displacements quadratic in the surface coordinates can produce focusing and defocusing effects, leading to a natural explanation for intense spot and line formation observed in the experiments.
 ISSN 2227-3123

*Keywords:* Beam formation, Collimated X-ray emission, Karabut experiment, Phase coherence, Up-conversion

## 1. Introduction

Karabut and his coworkers at the Luch Institute reported the observation of excess heat and other anomalies in glow discharge experiments in the early 1990s [1]. In subsequent experiments Karabut noticed that soft X-rays near 1.5 keV were emitted, and that they were collimated upward in his experiment normal to the cathode surface [2]. This effect was studied for more than a decade [3–10], and was found to be independent of the cathode metal (the effect was seen with Al, and with other metals through W), also to be independent of which discharge gas was used (collimated emission was seen with $H_2$, $D_2$, He, Ne, Ar and Xe).

*E-mail: plh@mit.edu

 ISSN 2227-3123

Collimated X-ray emission in this experiment is a striking anomaly for a variety of reasons. In order to arrange for collimated X-ray emission, either you need an X-ray laser, or else you need coherence among the emitter phases; either option would have deep implications. Karabut was convinced, especially in his later years, that he had made an X-ray laser. In some recent articles Ivlev speculates about the possibility of an X-ray laser mechanism in connection with Karabut's experiment [11,12].

In years past the author spent a decade modeling and designing X-ray lasers [13]; an experience that led to an understanding of just how difficult it is to create a relevant population inversion and to amplify X-rays. The notion of a population inversion at 1.5 keV involving electronic transitions in a solid state environment is unthinkable due to the very short lifetime. And then even if somehow a population inversion could be generated, one would need enough amplifier length to produce a collimated beam (the solid state medium is very lossy), as well as an amplifier geometry consistent with the observed beam formation. The very broad line shape associated with the collimated emission also argues against an X-ray laser mechanism. All of these headaches combine to rule out an X-ray laser mechanism associated with the solid. The primary headache associated with an X-ray laser in the gas phase is the absence of relevant electronic transitions in hydrogen, deuterium, helium and in neon gas. In this case one could contemplate the possibility of a ubiquitous impurity in the discharge gas; however, this leads to an additional headache of coming up with enough inverted atoms, molecules or ions to provide many gain lengths. If somehow one has any optimism left for the approach, a consideration of the relatively long (millisecond) duration of the collimated X-ray emission following the turning off of the discharge current should provide a cure. If the upper state radiative life time is long then the gain is very low; and if the gain is high then the upper state radiative life time is very short and the power requirement becomes prohibitive.

All of these arguments have led us to consider collimated X-ray emission as a result of a phased array emission effect. In this case serious issues remain; such as how excitation is produced (which in this case is much easier since a population inversion is not required); and how phase coherence might be established. From our perspective, both excitation and phase coherence could be developed via the up-conversion of vibrations to produce nuclear excitation in $^{201}$Hg, which is special because it has the lowest energy excited state (at 1565 eV) of any of the stable nuclei. We have reported on our earlier studies of models that describe up-conversion in the lossy spin-boson model, and various extensions and generalizations [14–16].

In this work we consider models for beam formation of the collimated X-ray emission in Karabut's experiment based on the assumption of phase coherent emitting dipoles randomly positioned on a plane, in connection with the "diffuse" X-ray emission effect observed under "normal" high-current operating conditions. The collimated X-rays in this case were observed to be normal to the cathode in a beam essentially the same size as the cathode; we find that beam formation in the high dipole density of the model (where the emission is produced from localized dipoles) works the same way. When the emitting dipole density is low then no beam forms, but a speckle pattern is produced. It might be proposed that the very intense spots seen in the experiments following the turning off of the discharge are connected with the random constructive interference effects that lead to speckle. However, we find that individual spots associated with the speckle pattern are too small to account for this "sharp" emission effect, and that speckle cannot account for lines or curves. Instead we find that spot formation and line formation follow naturally from models that describe surface deformations that are quadratic or higher-order in the transverse surface coordinates.

A weak speckle pattern is generated at low emitting dipole density, and a beam is produced when the emitting dipole density is high. A critical number or density of emitting dipoles can be estimated for the development of a beam. Since beam formation is reported in Karabut's experiment, it is possible to develop a constraint on the number of emitting dipoles consistent with experiment. We have conjectured previously that a small amount of mercury contamination in the chamber might result in some mercury sputtered onto the cathode surface, resulting in a relatively small number of mercury nuclei that emit on a broadened version of the 1565 eV transition in $^{201}$Hg. It is possible to develop a lower

bound on the number of mercury atoms present near the surface, to see whether it is consistent with the proposed picture.

Key features of the model which allows for collimation of the emitted beam normal to the surface are the phase coherence assumed, as well as the surface itself (which in the model is mathematically flat). There is no reason to think that the cathode surface is flat at the atomic scale, since whatever the surface looked like initially is modified in the ion bombardment, and surface loss through sputtering, which occurs during discharge operation at high current density. Mercury atoms in the discharge gas ionized above the cathode fall would be accelerated toward the cathode surface in this picture with an energy of up to a few keV, which means that they would end up randomly positioned in the outer 5–10 nm of the cathode surface. If so, then one would not expect any alignment in a plane, as assumed in the model, unless there were an ordering of the crystal planes so that some fraction of them were aligned with the cathode surface. The expected randomization of the locations of the mercury atoms inside the cathode surface would make beam formation to be impossible, except from the occasional crystal plane accidentally aligned with the surface.

However, it is well known in the literature that substantial deformation of a metal, as occurs during rolling, can result in a substantial alignment of the local crystal planes with the surface [17–19]. It seems likely that the cathodes used by Karabut were from stock that was rolled, so that one would expect the cathodes themselves to provide a source of crystal planes oriented with the surface. During the discharge operation the cathodes undergo additional surface deformation due to local thermal effects and electrostatic forces, which provides a natural mechanism for intense spot and line formation. In this picture the crystal ordering built in during rolling is largely maintained during the deformations that occuring during discharge operation.

## 2. Basic Model

We note that models for random arrays of emitting dipoles have been studied previously; in the case of random linear arrays, see [20–23]; a model for a random distribution of antennas in a two dimensional circle has been studied in [24]; and for a random distribution in a triangle in [25]. Statistical models for the analysis of beam formation from random antenna arrays have also been discussed in [26–28].

Following the discussion above, we turn our attention to a simple model for X-ray emission due to a collection of identical emitting dipoles that are randomly distributed in a plane. We can write for the vector potential in the case of oscillating electric dipoles [29] the summation

$$\mathbf{A}(\mathbf{r}) = -i\sum_j \frac{k\mathbf{p}_j}{|\mathbf{r}-\mathbf{r}_j|}\exp\left\{ik|\mathbf{r}-\mathbf{r}_j|\right\} \rightarrow -i\frac{k\mathbf{p}}{|\mathbf{r}|}\sum_j \exp\left\{ik|\mathbf{r}-\mathbf{r}_j|\right\}, \tag{1}$$

where we have assumed uniform phase, identical dipoles, and we focus on the field that results far away from the plane. The nuclear transition in $^{201}$Hg is a magnetic dipole transition, which provides the motivation to consider the analogous approximation for a set of oscillating magnetic dipoles

$$\mathbf{A}(\mathbf{r}) = i\sum_j \frac{k\hat{\mathbf{n}}_j\times\mathbf{m}_j}{|\mathbf{r}-\mathbf{r}_j|}\exp\left\{ik|\mathbf{r}-\mathbf{r}_j|\right\} \rightarrow i\frac{k\hat{\mathbf{n}}\times\mathbf{m}}{|\mathbf{r}|}\sum_j \exp\left\{ik|\mathbf{r}-\mathbf{r}_j|\right\}. \tag{2}$$

In either case, the resulting intensity is proportional to

$$I(\mathbf{r}) \sim \left|\sum_j \exp\left\{ik|\mathbf{r}-\mathbf{r}_j|\right\}\right|^2 = \sum_j\sum_{j'}\exp\left\{ik(|\mathbf{r}-\mathbf{r}_j|-|\mathbf{r}-\mathbf{r}_{j'}|)\right\}. \tag{3}$$

The dipoles are assumed to lie in the emitting plane defined by $z_j = 0$, and we are interested in the intensity pattern produced at image plane defined by $z = Z$ (a schematic is shown in Fig. 1). In this case we can write

$$I(x,y,Z) \sim \sum_j \sum_{j'} \exp\left\{ik\left(\sqrt{(x-x_j)^2+(y-y_j)^2+Z^2} - \sqrt{(x-x_{j'})^2+(y-y_{j'})^2+Z^2}\right)\right\}. \quad (4)$$

Simulations based on this model predicts beam formation for small areas when the dipole density is high, and spot formation in the case of larger areas or when the dipole density is low.

Since the locations of the dipoles are probabilistic, it will be of interest to estimate the expectation value of the intensity

$$\mathrm{E}[I(\mathbf{r})] \sim \sum_j \sum_{j'} \mathrm{E}\left[\exp\left\{ik(|\mathbf{r}-\mathbf{r}_j| - |\mathbf{r}-\mathbf{r}_{j'}|)\right\}\right]. \quad (5)$$

In what follows we will focus on specific model results for the summation on the right-hand side.

## 3. Beam Formation in the High Density Limit

Beam formation occurs when there are several dipoles that are sufficiently close together so that their contributions can combine coherently. In this regime there is the possibility of making use of a Taylor series expansion according to

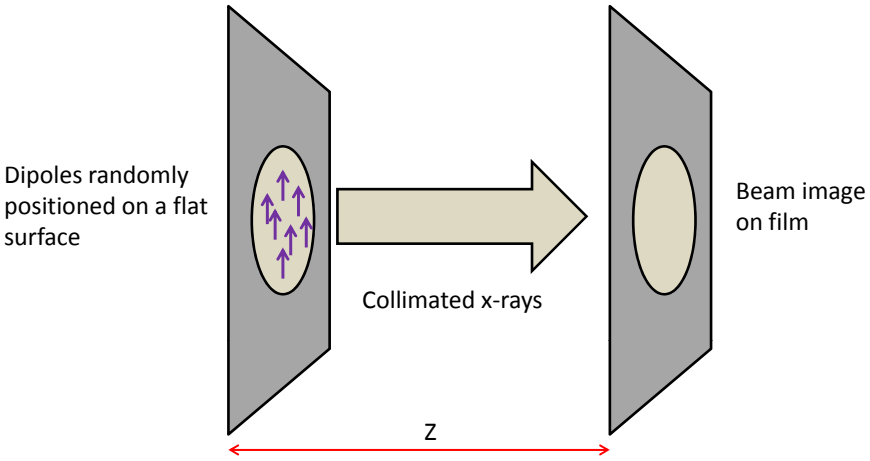


**Figure 1.** Schematic of the model. Phase coherent dipoles are positioned randomly within an emitting area of the cathodes surface, and radiate to form a beam if the emitting dipoles are in phase and have a sufficiently high density.

$$
\begin{aligned}
|\mathbf{r}-\mathbf{r}_j| &= \sqrt{(x-x_j)^2+(y-y_j)^2+Z^2} \\
&= Z\sqrt{1+\frac{(x-x_j)^2}{Z^2}+\frac{(y-y_j)^2}{Z^2}} \\
&= Z\left[1+\frac{(x-x_j)^2}{2Z^2}+\frac{(y-y_j)^2}{2Z^2}+\cdots\right].
\end{aligned} \tag{6}
$$

In this case we can write for the difference

$$
\begin{aligned}
|\mathbf{r}-\mathbf{r}_j|-|\mathbf{r}-\mathbf{r}_{j'}| &= \frac{(x-x_j)^2}{2Z}+\frac{(y-y_j)^2}{2Z}-\frac{(x-x_{j'})^2}{2Z}-\frac{(y-y_{j'})^2}{2Z}+\cdots \\
&= \frac{(x_{j'}-x_j)x+(y_{j'}-y_j)y}{Z}+\frac{x_j^2-x_{j'}^2+y_j^2-y_{j'}^2}{2Z}+\cdots
\end{aligned} \tag{7}
$$

If we assume that beam formation is dominated by contributions from the lowest order terms in the Taylor series expansion, then we can write

$$
I(x,y,Z)\sim\sum_j\sum_{j'}\exp\left\{ik\left(\frac{(x_{j'}-x_j)x+(y_{j'}-y_j)y}{Z}+\frac{x_j^2-x_{j'}^2+y_j^2-y_{j'}^2}{2Z}\right)\right\}. \tag{8}
$$

The locations of the emitting dipoles are random variables, so that the intensity will be random as well. It will be of interest to estimate the expectation value of the intensity which we can write as

$$
\mathrm{E}[I(x,y,Z)]\sim\sum_j\sum_{j'}\mathrm{E}\left[\exp\left\{ik\left(\frac{(x_{j'}-x_j)x+(y_{j'}-y_j)y}{Z}+\frac{x_j^2-x_{j'}^2+y_j^2-y_{j'}^2}{2Z}\right)\right\}\right]. \tag{9}
$$

If we assume that the various $x_j$ and $y_j$ values are independent, then this becomes

$$
\begin{aligned}
\mathrm{E}[I(x,y,Z)]\sim\sum_j\sum_{j'}&\mathrm{E}\left[\exp\left\{ik\left(\frac{-2x_jx+x_j^2}{2Z}\right)\right\}\right]\mathrm{E}\left[\exp\left\{-ik\left(\frac{2x_{j'}x+x_{j'}^2}{2Z}\right)\right\}\right], \\
&\mathrm{E}\left[\exp\left\{ik\left(\frac{-2y_jy+y_j^2}{2Z}\right)\right\}\right]\mathrm{E}\left[\exp\left\{-ik\left(\frac{2y_{j'}y+y_{j'}^2}{2Z}\right)\right\}\right] \\
&= N^2\left|\mathrm{E}\left[\exp\left\{ik\left(\frac{-2x_jx+x_j^2}{2Z}\right)\right\}\right]\mathrm{E}\left[\exp\left\{ik\left(\frac{-2y_jy+y_j^2}{2Z}\right)\right\}\right]\right|^2.
\end{aligned} \tag{10}
$$

For simplicity, let us assume uniform probability distributions for a square emitting region defined by

$$
\begin{aligned}
f_X(x_j) &= \frac{1}{L} \quad (-L/2<x<L/2), \\
f_Y(y_j) &= \frac{1}{L} \quad (-L/2<x<L/2).
\end{aligned} \tag{11}
$$

Also for simplicity let us focus on the origin at the image, so that

$$\mathrm{E}[I(0,0,Z)] \sim N^2 \left| \mathrm{E}\left[\exp\left\{ik\left(\frac{x_j^2}{2Z}\right)\right\}\right] \mathrm{E}\left[\exp\left\{ik\left(\frac{y_j^2}{2Z}\right)\right\}\right]\right|^2 . \tag{12}$$

We can approximate

$$\begin{aligned}\mathrm{E}\left[\exp\left\{ik\left(\frac{x_j^2}{2Z}\right)\right\}\right] &= \int_{-L/2}^{L/2} f_X(x') \exp\left\{ik\left(\frac{x_j^2}{2Z}\right)\right\} \mathrm{d}x' \\ &\to \frac{1}{L}\int_{-\infty}^{\infty} \exp\left\{ik\left(\frac{x_j^2}{2Z}\right)\right\} \mathrm{d}x' = \frac{1}{L}\sqrt{\frac{i2\pi Z}{k}} \\ &= \frac{1}{L}\sqrt{i\lambda Z}. \end{aligned} \tag{13}$$

We end up with

$$\mathrm{E}[I(0,0,Z)] \sim \frac{(\lambda Z)^2}{L^4} N^2. \tag{14}$$

We have verified that the numerical are consistent with this estimate in the limit of high dipole density for a square emitting region. Adapting this formula to emission from a circular area by simply modifying the area appears to work well in comparison with numerical results.

## 4. Average Intensity in the Low Density Limit

We recall that the expectation value of the intensity is proportional to

$$\mathrm{E}[I(\mathbf{r})] \sim \sum_j \sum_{j'} \mathrm{E}\left[\exp\left\{ik(|\mathbf{r}-\mathbf{r}_j| - |\mathbf{r}-\mathbf{r}_{j'}|)\right\}\right]. \tag{15}$$

In the high density limit we took advantage of a Taylor series approximation, as well the separability of the sums in $j$ and in $j'$, to develop an estimate for the expectation value. In the low density limit it is possible to develop an estimate for the expectation value of the intensity by neglecting contributions from dipoles at different locations; at low density there are not nearby emitting dipoles for local phase coherence to contribute significantly. In this case we can write

$$\begin{aligned}\mathrm{E}[I(\mathbf{r})] &\sim \sum_j \mathrm{E}\left[\exp\left\{ik(|\mathbf{r}-\mathbf{r}_j| - |\mathbf{r}-\mathbf{r}_j|)\right\}\right] + \sum_j \sum_{j'\neq j} \mathrm{E}\left[\exp\left\{ik(|\mathbf{r}-\mathbf{r}_j| - |\mathbf{r}-\mathbf{r}_{j'}|)\right\}\right] \\ &= N + \sum_j \sum_{j'\neq j} \mathrm{E}\left[\exp\left\{ik(|\mathbf{r}-\mathbf{r}_j| - |\mathbf{r}-\mathbf{r}_{j'}|)\right\}\right] \to N. \end{aligned} \tag{16}$$

When the dipole density is low then the expectation value of the complex terms can be thought of as involving random phases so that

$$\mathrm{E}\left[\exp\left\{ik(|\mathbf{r}-\mathbf{r}_j|-|\mathbf{r}-\mathbf{r}_{j'}|)\right\}\right] \to \mathrm{E}\left[\mathrm{e}^{i\theta}\right] = \frac{1}{2\pi}\int_0^{2\pi}\mathrm{e}^{i\theta}\mathrm{d}\theta = 0.$$

In this limit there is no beam formation; instead there is a speckle pattern with average intensity proportional to $N$, in the vicinity of where a beam might have formed if $N$ were higher, and also away from where the beam might have formed.

It is possible to develop an empirical approximation that includes both the contribution from the low density limit and from the high density limit according to

$$\mathrm{E}[I(\mathbf{r})] \sim \left|\sum_j \exp\left\{ik|\mathbf{r}-\mathbf{r}_j|\right\}\right|^2 = \begin{cases} N + \left(\dfrac{\lambda Z}{L^2}\right)^2 N^2, & \text{within beam pattern,} \\ N, & \text{outside of beam.} \end{cases} \tag{17}$$

This result is closely related to the exact formal result for the expectation value in [27,31].

## 5. Numerical Results

We have carried out simulations with randomly located dipoles in a square corresponding to the models described above, and have found good agreement with the simple probabilistic models outlined above. The exposed surface of the cathodes in the Karabut experiment are circular, which motivates us to consider the generalization

$$\mathrm{E}[I(\mathbf{r})] \sim \mathrm{E}\left[\left|\sum_j \exp\left\{ik|\mathbf{r}-\mathbf{r}_j|\right\}\right|^2\right] = \begin{cases} N + \left(\dfrac{\lambda Z}{\pi R^2}\right)^2 N^2, & \text{within beam pattern,} \\ N, & \text{outside of beam} \end{cases} \tag{18}$$

appropriate to emitting dipoles within a circular region of radius $R$.

An example of beam formation is illustrated in Fig. 2, where we see that dipoles randomly localized on a plane within a circle of radius 100 $\mu$m results in a circular beam with a radius 100 $\mu$m. Diffraction rings are apparent in the image which are a result of the discontinuity in the dipole density near the edge of the circular emitting area. One also sees a speckle pattern which results from the limited number of dipoles present in the calculation.

In Fig. 3 is shown the average intensity (from many simulations) in the case of a 100 $\mu$m radius circle containing random emitting dipoles and a 100 $\mu$m radius circle on the image plane displaced 25 cm in $z$. One can see that at low dipole density the average intensity is that of a spot pattern, and at high intensity the average intensity matches the analytic estimate. The empirical formula of Eq. (18) is seen to be a good match over the whole range of dipole densities.

## 6. Beam Formation in the Karabut Experiment

Although we have no published photographic record of beam formation in Karabut's experiment, there are two photographs that show the damage done to a Be window and a plastic window in [30]. It might have been possible to discern the amount of speckle present from an X-ray photographic image of the beam, which based on the analysis above would have provided us with information about how many emitting dipoles are present. In some of the photographic spectra taken in the bent mica crystal spectrometer configuration of Ref. [8] there is obvious speckle present,

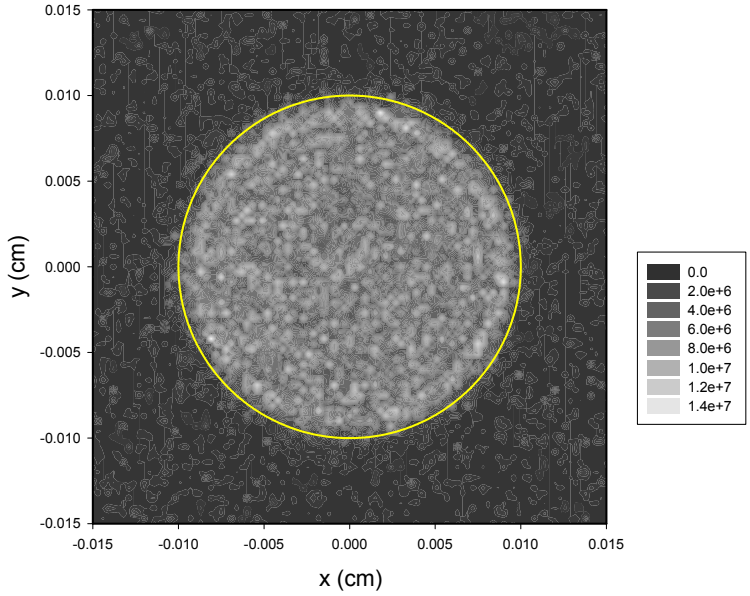


**Figure 2.** Beam at image plane located at $Z = 25$ cm in the case of a dipole density of $10^9$ cm$^{-2}$ localized in a circle of radius 100 $\mu$m. Marked in yellow is a circle of radius 100 $\mu$m.

which tells us that the quadratic beam contribution to the intensity is not so many orders of magnitude greater than the linear speckle contribution.

From the empirical model described above we can define a critical number of dipoles $N_0$ at which the linear and quadratic contributions match

$$N_0 = \left(\frac{\lambda Z}{\pi R^2}\right)^2 N_0^2. \tag{19}$$

We can evaluate

$$N_0 = \left(\frac{\pi R^2}{\lambda Z}\right)^2. \tag{20}$$

If we assume that phase coherence among the emitting dipoles is established over the entire surface of the cathode, then we can develop a numerical estimate for the critical number of dipoles. For this estimate we take

$$R = 0.5 \text{ cm}, \quad \lambda = 8 \text{ nm}, \quad Z = 25 \text{ cm}. \tag{21}$$

The corresponding critical number in this case is

$$N_0 = 1.5 \times 10^{11}. \tag{22}$$

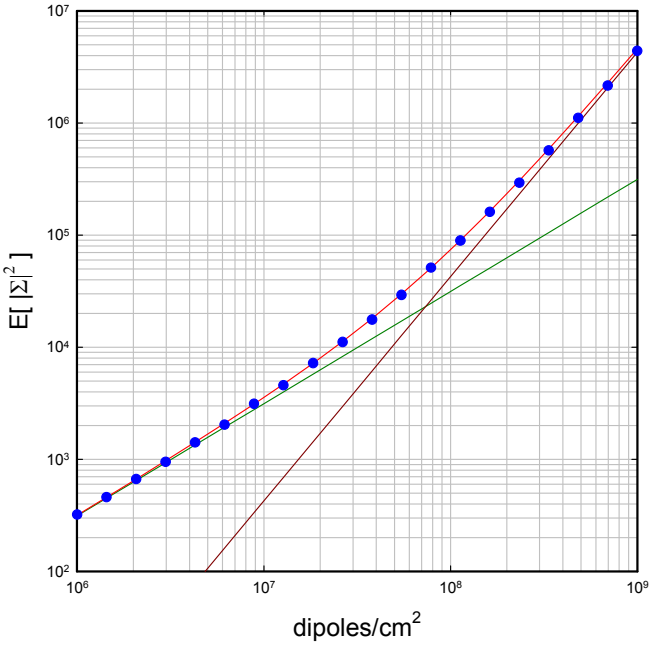


**Figure 3.** Expectation value $\mathrm{E}\left[\left|\sum_j \exp\left\{ik|\mathbf{r}-\mathbf{r}_j|\right\}\right|^2\right]$ as a function of dipole density (*red circles*); low density limit (*blue line*); high density limit (*dark green line*); empirical estimate (*dark green line*).

In this picture we would good expect beam formation when the number of dipoles is larger than $N_0$ by an order of magnitude or more.

Another possibility is that phase coherence is established over only a part of the cathode surface, in which case the critical number of dipoles would be smaller by the square of the ratio of the coherence area to the cathode area.

## 7. Spot Formation

When the dipole density is low we see speckle formation in the image plane, which is a consequence of fluctuations in the intensity. We are interested in the development of a model that we can use to estimate the intensity of a spot given the number of emitting dipoles in a given area.

We recall that the intensity is determined from the random locations of the dipoles according to

$$I(\mathbf{r}) \sim \left|\sum_j \exp\left\{ik|\mathbf{r}-\mathbf{r}_j|\right\}\right|^2 . \tag{23}$$

To form a spot we need for the phases associated with the different dipoles to be nearly the same. In this model we are specifically not interested the phase coherence associated with beam formation, in which the contribution from many

dipoles near a point add coherently. Instead we are interested in spot formation where the contribution from dipoles that are well separated combine randomly.

Since the contribution from each dipole is assumed to be equal in this model, the only difference in the contribution comes from the phase factor. If the dipole positions are random, then we might presume that the associated phases are random as well. Consequently, we might consider the simpler model defined by

$$\theta = \left| \sum_{j=1}^{N} \exp\left\{ i\phi_j \right\} \right|^2 = \sum_{j=1}^{N} \sum_{k=1}^{N} \exp\left\{ i(\phi_j - \phi_k) \right\}. \tag{24}$$

From numerical simulations, the associated probability distribution is exponential in $\theta$ according to

$$f_\Theta(\theta) \to \frac{1}{N} \exp\left\{ -\frac{\theta}{N} \right\}. \tag{25}$$

This result is consistent with a random walk model in two dimensions, and is well known in the literature in the context of speckle [32]. In the event that fewer than the critical number of dipoles emit in this model, then there is little or no beam apparent, but instead individual randomly positioned spots associated with speckle.

According to this model the average intensity will be proportional to $N$

$$\mathrm{E}[I] \sim \mathrm{E}[\theta] = N \tag{26}$$

with spots at higher intensity being rarer exponentially in the intensity. This result is consistent with the low dipole density model discussed briefly above, where

$$\mathrm{E}[I(\mathbf{r})] \sim \mathrm{E}\left[ \left| \sum_j \exp\left\{ ik|\mathbf{r} - \mathbf{r}_j| \right\} \right|^2 \right] = N. \tag{27}$$

In Fig. 4 we show a calculated image of the weak beam and spots under conditions where the density of dipoles is lower, so that the total number of emitting dipoles is a bit less than the critical number. In this case the dipole density is $5 \times 10^7$ cm$^{-2}$, and the critical density needed for beam formation is about $7.4 \times 10^7$ cm$^{-2}$. A histogram of intensities for the speckle pattern and weak beam inside of the indicated circle is shown in Fig. 5, and is seen to be close to exponential consistent with the discussion above, and in this case the number of match dipoles in the circle is a reasonable match to the exponential fall off.

Karabut reported that the "diffuse" spectra that he observed appears when the discharge is running, and that the very intense "sharp" emission could be seen when the discharge was turned off suddenly [8]. In this case there is a large current spike (short in time) which accompanies the turning off of the current. Of interest is how this "sharp" emission might be interpreted. We previously proposed that this effect could be a result of Dicke superradiance from emitting dipoles in a localized region, where the emitting region was thought to be on the order of a square millimeter [33]. In the following section surface deformations will be considered, which will provide a superior interpretation.

We might have conjectured that the very intense spots might be a speckle effect under conditions where the individual dipole emission is stronger than in the case of beam formation. One argument against such a proposal is that individual speckles in this calculation are quite small, with a peak intensity only over a few microns by a few microns. The intense features in Karabut's data are much larger.

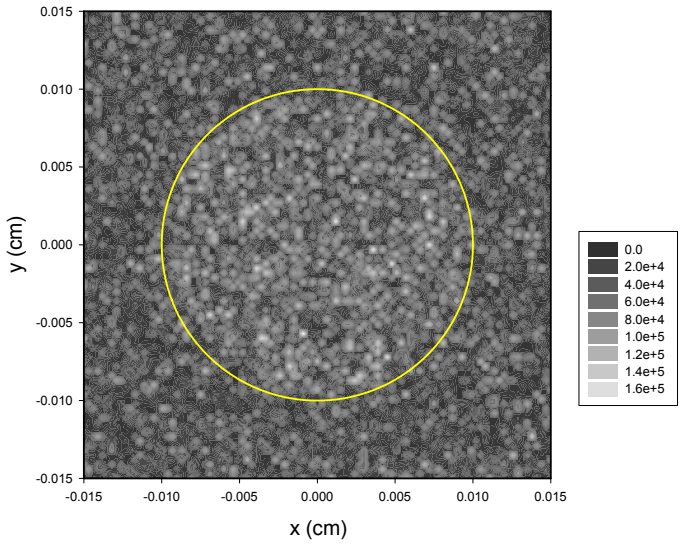


**Figure 4.** Beam at image plane (located at $Z = 25$ cm in the case of a dipole density of $5 \times 10^7$ cm$^{-2}$ localized in a circle of radius 100 $\mu$m. Marked in yellow is a circle of radius 100 $\mu$m).

It is of interest to examine the intensity distribution in the case of beam formation. In Fig. 6 we show a histogram of the intensities when the emitting dipole density is $10^9$ cm$^{-2}$. This intensity distribution corresponds to the beam illustrated in Fig. 2, which shows some diffraction rings inside near the boundary of the circle. The brightest speckles are seen to be associated with the outermost diffraction ring which is on average brightest. Once again the individual speckles in this calculation are very small, and we would not expect them to account for the intense spots seen in Karabut's experiment.

## 8. Surface Deformation Effects

After a number of runs in the glow discharge, the cathode has undergone plastic deformations (as was clear in experiments done at MIT with a copy of Karabut's system in the 1990s prior to the discovery of the collimated X-ray emission effect). Consequently, we would not expect there to be a mathematically flat surface present, even if the cathode somehow started out mathematically flat. There are also transient effects associated with compressional, transverse, and drum head mode excitation. We would expect the largest dynamic effects to be due to excitation of the drum head modes.

It is possible to include these effects in our description by working with a displacement field $\mathbf{u}(x, y, t)$ which keeps track of the amount of displacement in the different directions. The intensity pattern including surface displacement can be written as

$$I(\mathbf{r}, t) \sim \left| \sum_j \exp\left\{ ik|\mathbf{r} - \mathbf{r}_j - \mathbf{u}(\mathbf{r}_j, t)| \right\} \right|^2 . \tag{28}$$

The idea here is that the dipole positions $\mathbf{r}_j$ are specified in the case of a mathematically flat surface. When the surface is displaced, the (slowly varying) displacement is added systematically to the initial positions of the dipoles in the contribution to the phase factors.

Since we expect the largest effect to come from drum head mode displacements and plastic deformations, we can restrict the surface displacement to be normal to the surface

$$\mathbf{u}(\mathbf{r},t) = \hat{\mathbf{i}}_z u(x,y,t). \tag{29}$$

It will be informative to consider the impact of low-order variations in the displacement; consequently, we work with a Taylor series expansion around the origin given by

$$u(x,y,t) = u(0,0,t) + x\frac{\partial u}{\partial x} + y\frac{\partial u}{\partial y} + \frac{1}{2}x^2\frac{\partial^2 u}{\partial x^2} + xy\frac{\partial^2 u}{\partial x \partial y} + \frac{1}{2}y^2\frac{\partial^2 u}{\partial y^2} + \cdots, \tag{30}$$

where the various derivatives are evaluated at $x = 0$ and $y = 0$, and may be oscillatory in time.

### 8.1. Uniform displacement

We consider first the impact of a uniform displacement

$$u(x,y,t) = u(0,0,t) = u_0(t). \tag{31}$$

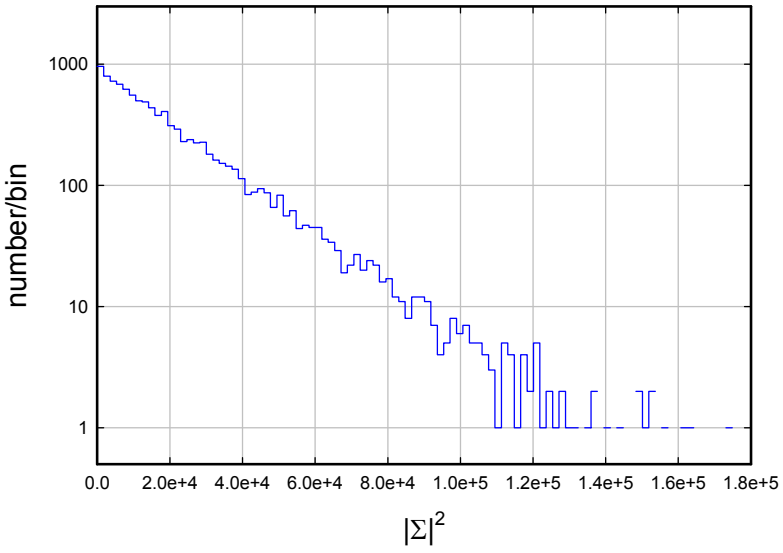


**Figure 5.** Histogram of intensity for speckle pattern with weak beam of Fig. 4.

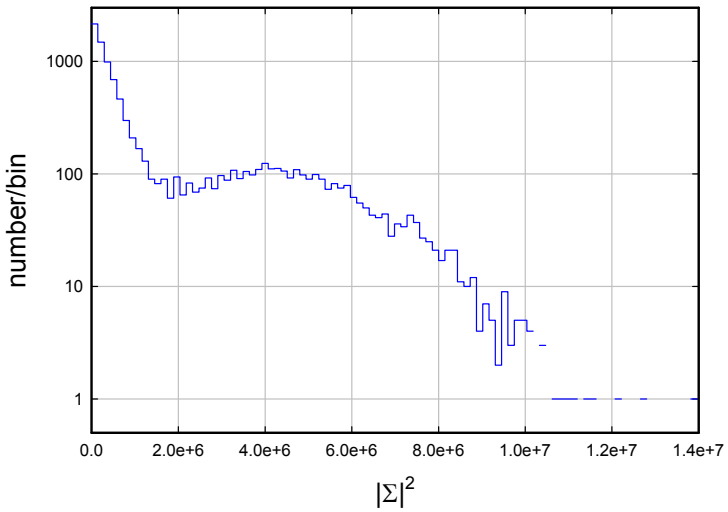


**Figure 6.** Histogram of intensity for speckle pattern with beam of Fig. 2 formed at an emitting dipole density of $10^9$ dipoles/cm$^2$.

In this case we can write for the intensity

$$I(\mathbf{r},t) \sim \left| \sum_j \exp\left\{ ik|\mathbf{r} - \mathbf{r}_j - \hat{\mathbf{i}}_z u_0(t)| \right\} \right|^2$$
$$= \left| \sum_j \exp\left\{ ik\sqrt{(x-x_j)^2 + (y-y_j)^2 + (Z-u_0(t))^2} \right\} \right|^2 . \quad (32)$$

Since we expect the largest displacement to be very small compared to the distance between the cathode and image plane

$$|u_0(t)| \ll Z, \quad (33)$$

we do not anticipate observable effects from uniform surface displacements.

### 8.2. Linear displacements

Next we consider linear displacements of the form

$$u(x,y,t) = a(t)x + b(t)y. \quad (34)$$

In this case we can write

$$I(\mathbf{r},t) \sim \left| \sum_j \exp\left\{ ik\sqrt{(x-x_j)^2+(y-y_j)^2+[Z-a(t)x_j-b(t)y_j]^2} \right\} \right|^2 . \tag{35}$$

We would expect the beam to be offset (in the high dipole density limit) depending on the surface gradient. We can include this effect by writing

$$\begin{aligned} I(\mathbf{r}'(t),t) &= I(\mathbf{r}+\hat{\mathbf{i}}_x\delta x(t)+\mathbf{i}_y\delta y(t),t) \\ &\sim \left| \sum_j \exp\left\{ ik\sqrt{[x+\delta x(t)-x_j]^2+[y+\delta y(t)-y_j]^2+[Z-a(t)x_j-b(t)y_j]^2} \right\} \right|^2 . \end{aligned} \tag{36}$$

We can eliminate some of the low-order terms in the phase by choosing

$$\delta x(t) = -Za(t), \qquad \delta y(t) = -Za(t). \tag{37}$$

If we focus on the beam originally at the origin of the image plane then we can write

$$\begin{aligned} I(\hat{\mathbf{i}}_x\delta x(t)+\mathbf{i}_y\delta y(t),t) &\sim \left| \sum_j \exp\left\{ ik\sqrt{[\delta x(t)-x_j]^2+[\delta y(t)-y_j]^2+[Z-a(t)x_j-b(t)y_j]^2} \right\} \right|^2 \\ &= \left| \sum_j \exp\left\{ ik\sqrt{x_j^2+y_j^2+Z^2+\delta x(t)^2+\delta y(t)^2+[a(t)x_j+b(t)y_j]^2} \right\} \right|^2 . \end{aligned} \tag{38}$$

If the displacements are small, then the higher-order terms can be neglected, and we have the approximate result

$$I(\hat{\mathbf{i}}_x\delta x(t)+\mathbf{i}_y\delta y(t),t) \sim \left| \sum_j \exp\left\{ ik\sqrt{x_j^2+y_j^2+Z^2} \right\} \right|^2 . \tag{39}$$

In this approximation the beam is collimated normal to the displaced surface, which is mathematically flat but not in the $x-y$ plane. The neglected phase factors in this case are present since the image plane is not collinear with the displaced flat surface.

### 8.3. Surface curvature

If the surface is curved, there is the possibility of increasing or reducing the beam intensity, since it may be that phase coherence can be maintained for more emitting dipoles. In general we can describe a curved surface through displacements of the form

$$u(x,y) = c(t)x^2 + d(t)y^2 + f(t)xy. \tag{40}$$

In this case we can write

$$I(\mathbf{r},t) \sim \left| \sum_j \exp\left\{ ik \left| \mathbf{r} - \mathbf{r}_j - \hat{\mathbf{i}}_z [c(t)x_j^2 + d(t)y_j^2 + f(t)x_j y_j] \right| \right\} \right|^2$$
$$= \left| \sum_j \exp\left\{ ik \sqrt{(x-x_j)^2 + (y-y_j)^2 + [Z - c(t)x_j^2 - d(t)y_j^2 - f(t)x_j y_j]^2} \right\} \right|^2 . \quad (41)$$

The intensity at the origin reduces to

$$I(0,0,Z,t) \sim \left| \sum_j \exp\left\{ ik \sqrt{x_j^2 + y_j^2 + [Z - c(t)x_j^2 - d(t)y_j^2 - f(t)x_j y_j]^2} \right\} \right|^2 . \quad (42)$$

Note that it is possible to arrange for cancellation if

$$2Zc(t) = 1, \quad 2Zd(t) = 1, \quad f(t) = 0. \quad (43)$$

In this case we can write

$$I(0,0,Z,t) \sim \left| \sum_j \exp\left\{ ik \sqrt{Z^2 + \frac{(x_j^2 + y_j^2)^2}{4Z^2}} \right\} \right|^2$$
$$= \sum_j \sum_{j'} \exp\left\{ ik \left( \sqrt{Z^2 + \frac{(x_j^2 + y_j^2)^2}{4Z^2}} - \sqrt{Z^2 + \frac{(x_{j'}^2 + y_{j'}^2)^2}{4Z^2}} \right) \right\} . \quad (44)$$

We can make use of a Taylor series expansion in this case to write

$$\sqrt{Z^2 + \frac{\rho_j^4}{4Z^2}} - \sqrt{Z^2 + \frac{\rho_{j'}^4}{4Z^2}} = \frac{\rho_j^4 - \rho_{j'}^4}{8Z^3} + \cdots \quad (45)$$

The intensity in this limit is approximately

$$I(0,0,Z,t) \sim \sum_j \sum_{j'} \exp\left\{ ik \left( \frac{(x_j^2 + y_j^2)^2 - (x_{j'}^2 + y_{j'}^2)^2}{8Z^3} \right) \right\} . \quad (46)$$

It is probably simplest to evaluate the expectation value assuming $N$ emitting dipoles in a circular area with radius $\rho_0$ around the origin, in which case the expectation value of the intensity is

$$\mathrm{E}[I(0,0,Z,t)] \sim \mathrm{E}\left[\sum_j \sum_{j'} \exp\left\{ik\left(\frac{(x_j^2+y_j^2)^2-(x_{j'}^2+y_{j'}^2)^2}{8Z^3}\right)\right\}\right]$$
$$= N^2\left|\mathrm{E}\left[\exp\left\{ik\left(\frac{\rho_j^4}{8Z^3}\right)\right\}\right]\right|^2. \tag{47}$$

To evaluate the expectation value we make use of a radial probability distribution given by

$$f(\rho) = \begin{cases} \dfrac{2\rho}{\rho_0^2}, & 0 \le \rho \le \rho_0, \\ 0, & \text{otherwise.} \end{cases} \tag{48}$$

We can compute

$$\mathrm{E}\left[\exp\left\{ik\left(\frac{\rho_j^4}{8Z^3}\right)\right\}\right] = \frac{2}{\rho_0^2}\int_0^{\rho_0} \rho \exp\left\{ik\left(\frac{\rho^4}{8Z^3}\right)\right\} \mathrm{d}\rho. \tag{49}$$

If the circle is sufficiently large, so that

$$\frac{k\rho_0^4}{8Z^3} = \frac{\pi\rho_0^4}{4\lambda Z^3} \gg 1 \tag{50}$$

(the characteristic value of $\rho_0$ for the numbers under consideration is about 2.5 mm) then we obtain

$$\mathrm{E}\left[\exp\left\{ik\left(\frac{\rho_j^4}{8Z^3}\right)\right\}\right] \to \frac{1}{\sqrt{-i}}\sqrt{\frac{2\pi Z^3}{k\rho_0^4}}. \tag{51}$$

In the end we can write

$$\mathrm{E}\left[\sum_j \sum_{j'} \exp\left\{ik\left(\frac{(x_j^2+y_j^2)^2-(x_{j'}^2+y_{j'}^2)^2}{8Z^3}\right)\right\}\right] = \left(\frac{2\pi Z^3}{k\rho_0^4}\right)N^2 = \left(\frac{\lambda Z^3}{\rho_0^4}\right)N^2. \tag{52}$$

This is a much greater intensity that we obtained with earlier models. Collimated X-ray emission under conditions where the surface is distorted in this way can result in a very intense beam with a corresponding small spot size at the image plane.

We note that surface displacement in this case is a focusing effect, with no enhancement in the area integral of the intensity at the image plane. An example of a focused beam with parameters

$$c(t) = 0.80\,\frac{1}{2Z}, \qquad d(t) = 0.80\,\frac{1}{2Z}, \qquad f(t) = 0 \tag{53}$$

is illustrated in Fig. 7. A beam in the shape of a line longer than the size of the circle containing the emitting dipoles is shown in Fig. 8. In this case the distorted surface parameters are

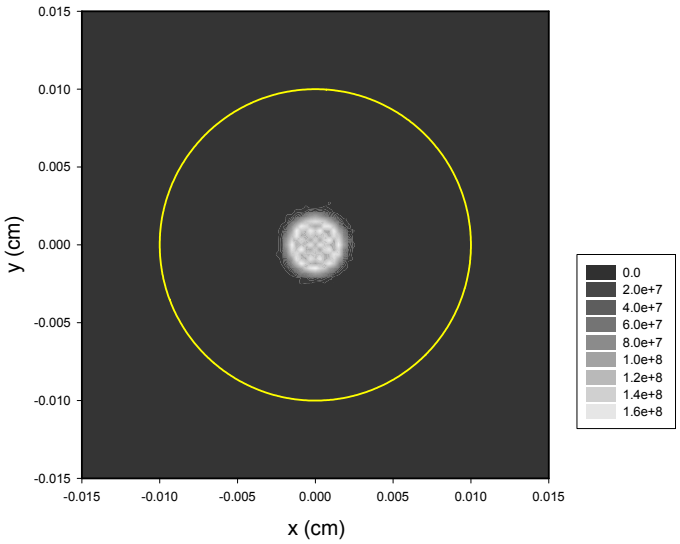


**Figure 7.** Partially focused beam at image plane located at $Z = 25$ cm in the case of a dipole density of $10^9$ cm$^{-2}$. Marked in yellow is a circle of radius 100 $\mu$m.

$$c(t) = -0.30\,\frac{1}{2Z}, \qquad d(t) = 0.90\,\frac{1}{2Z}, \qquad f(t) = 0. \tag{54}$$

## 9. Discussion and Conclusions

Collimated X-ray emission in the Karabut experiment is an anomaly that cannot be understood based on currently accepted solid state and nuclear physics, which provides motivation for seeking an understanding of the effect. There are two possible origins of a collimation effect: either an X-ray laser has been created; or else beam formation is due to phased array emission. We have argued many times against the proposal that an X-ray laser has been created, in part due to the absence of any compelling mechanism to produce a population inversion, in part due to the associated high power density requirement, and in part due to the mismatch between the geometry needed for beam formation and the geometry of the experiment.

Instead we have conjectured that the collimation is a consequence of phased array emission, a proposal which on the one hand is free of the strong objections against an X-ray laser mechanism, but which on the other hand brings new issues to resolve. The two most significant mechanistic issues are how excitation in the keV range can be produced, and how phase coherence might be established. These problems are very serious; however, in our view there are plausible mechanisms for both of these issues.

Independent of Karabut's experiment we have for many years been interested in mechanisms that might down-convert a large nuclear quantum in the Fleischmann–Pons experiment, to account for excess heat as due to nuclear reactions without commensurate energetic nuclear radiation. The big headache in understanding the mechanism through which excess heat is produced is that in a successful experiment one has the possibility of measuring thermal energy and $^4$He in the gas phase, neither of which at this point shed much light on whatever physical mechanism is involved.

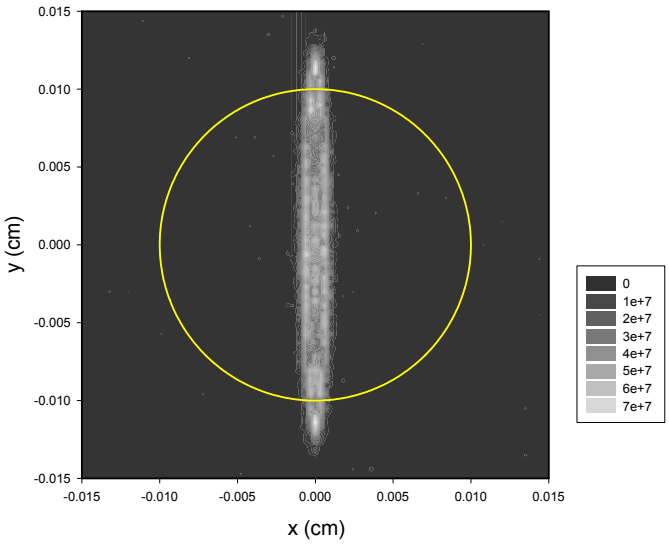


**Figure 8.** Beam partially focused in $x$ and defocused in $y$ at image plane located at $Z = 25$ cm in the case of a dipole density of $10^9$ cm$^{-2}$. Marked in yellow is a circle of radius 100 $\mu$m.

If the large nuclear quantum is being down-converted, then we would want to study the down-conversion mechanism in a different kind of experiment more easily diagnosed and interpreted. Because of the intimate theoretical connection between up-conversion and down-conversion, we have the possibility of understanding how down-conversion works by studying up-conversion. Initially we contemplated a theory-based experiment in which THz vibrations would be up-converted to produce excitation at 1565 eV in $^{201}$Hg nuclei, which has the lowest energy excited state of all the stable nuclei, and which would decay primarily by internal conversion but also in part via X-ray emission. In this proposed theory-based experiment we recognized that the up-conversion of vibrational energy would result in phase coherence, with the possibility of phased array beam formation. The claim of collimated X-ray emission near 1.5 keV in the Karabut experiment drew our attention since it seemed that the up-conversion experiment that we were interested might have already been implemented. From this perspective collimation in the Karabut experiment could be interpreted as an experimental confirmation of the up-conversion mechanism, primarily since there seems to be no other plausible interpretation. Collimated X-ray emission claimed in some cases near 1.5 keV in the water jet experiments of Kornilova, Vysotskii and coworkers [34–37] seems to us to be closely related, and to provide another experiment where up-conversion is observed (a point of view we note that is at odds with the theoretical explanation put forth by Vysotskii in these references).

One motivation for the modeling described in this paper was to see whether we might develop constraints on the number of emitting dipoles involved, which according to our picture would shed light on the number of mercury atoms present on the surface. We had thought initially that low levels of mercury as an impurity in the cathodes or in the gas might be responsible for the collimated emission; however, the spectra published by Karabut shows no indication of edge absorption which favors implantation from mercury contamination in the discharge gas. For example, the K-edge absorption in aluminum starts at 1562 eV, which should be readily apparent if the emission originates in the bulk. The transmission for a 1 $\mu$m Al layer is close to 90% below the K-edge, and near 30% above the K-edge (see

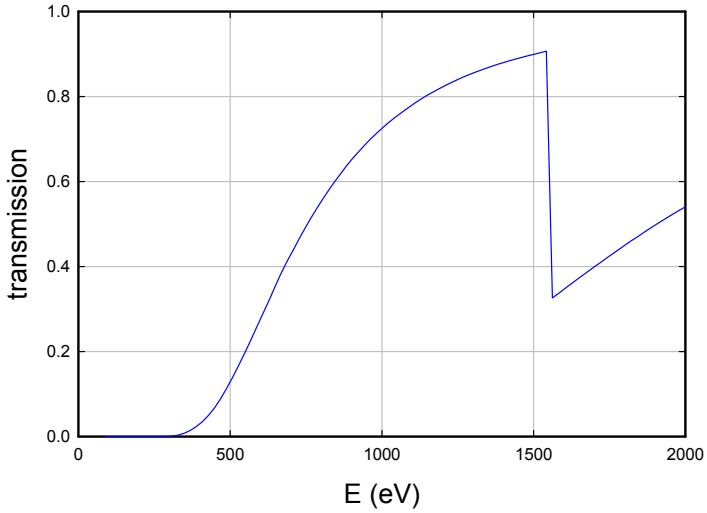


**Figure 9.** Transmission through 1 $\mu$m of Al as a function of the X-ray energy from Henke's online x-ray transmission calculator.

Fig. 9); this difference would be readily apparent in the spectra if the emission was due to bulk radiators. The absence of an observable K-edge absorption feature in the spectrum suggests that the emission is localized to within 0.1 $\mu$m or less from the surface, which is consistent with implantation from the mercury as an impurity in the discharge gas. Beam formation requires a dipole density above a threshold value, and we have estimated the threshold to correspond to about $1.5 \times 10^{11}$ emitting dipoles in the Karabut experiment. Probably the total number of dipoles is on the order of $1.5 \times 10^{12}$ or higher, to be consistent with unambiguous beam formation. Since the natural abundance of $^{201}$Hg is 13.18%, this puts the total number of mercury atoms at or above $10^{13}$.

For beam formation we made use of a model based on emitting dipoles randomly positioned on a mathematical plane within a circle, to match the cathode geometry in Karabut's experiment. Beam formation in this case requires both uniform phase, and for there to be a mathematical plane to restrict random variations in position normal to the surface. In previous work presented at ICCF17 we assumed that the dipoles were randomly spaced in a volume near the surface, which could produce speckles, but we did not appreciate at the time that this model does not produce a beam of about the same size as the cathode. The orientation of the crystal planes aligned with the surface produced by the rolling process used in the fabrication of the foils from which the cathodes are taken is critical for beam formation, based on the model studied in this paper.

We have speculated previously about the origin of the very intense spots and lines that appear on the film (and which produces film damage), including proposals that small fraction of the surface produces a collimated beam to form a spot, and that a line might be produced by a steering effect. Here we have shown that surface deformation can produce a focusing of the beam, both in one dimension to produce a line, and in two dimensions to produce a spot. This new picture provides in our view a much stronger argument than the earlier speculation.

We have previously speculated at ICCF17 that the bursts in emission following the turning off of the discharge was due to nonlinear Rabi oscillations in the donor and receiver model, a proposal strongly criticized by Vysotskii [38] on the grounds that the strong coupling needed to produce such rapid nonlinear Rabi oscillations was unlikely. In

retrospect Vysotskii's argument seems right, and we have subsequently been thinking about new models for the up-conversion which will be discussed elsewhere. However, in these models the burst effect comes about from the basic time dependence of the phonon–nuclear coupling matrix element, which in this case involves two photon exchange since the transition is M1 and the phonon-nuclear interaction is E1, to produce a $\cos^4 \omega_0 t$ time-dependence which is sharpened by a nonlinearity associated with local up-conversion effects. In this picture the excitation of the $^{201}$Hg transition is from excitation transfer from much more strongly coupled transitions in the cathode holder and steel target chamber, and drum head mode excitation of the cathode mediates this excitation transfer.

## References


[1] A.B. Karabut, Ya.R. Kucherov and I. B. Savvatimova, Nuclear product ratio for glow discharge in deuterium, *Phys. Lett. A.* **170** (1992) 265–272.

[2] A.B. Karabut, Research into powerful solid X-ray laser (wave length is 0.8–1.2 nm) with excitation of high current glow discharge ions, *Proc. 11th Int. Conf. on Emerging Nuclear Energy Systems*, 29 September–4 October 2002, Albuquerque, New Mexico, USA, pp. 374–381.

[3] A.B. Karabut, Experimental research into characteristics of X-ray emission from solid-state cathode medium of high-current glow discharge, *Proc. 10th Int. Conf. on Cold Fusion*, August 24–29, 2003, Cambridge, MA, USA.

[4] A.B. Karabut, Research into characteristics of X-ray emission laser beams from solid-state cathode medium of high current glow discharge, *Proc. 11th Int. Conf. on Cold Fusion*, 31 October–5 November, 2004, France, pp. 253–257.

[5] A.B. Karabut, Study of energetic and temporal characteristics of X-ray emission from solid state cathode medium of high current glow discharge, *Proc. 12th Int. Conf. on Cold Fusion*, December 2–7, 2006, Japan, pp. 344–350.

[6] A.B. Karabut and E.A. Karabut, Research into energy spectra of X-ray emission from solid cathode medium during the high current glow discharge operation and after the glow discharge current switch off, *Proc. 14th Int. Conf. on Cold Fusion*, August 10–15, 2008, USA.

[7] A.B. Karabut and E.A. Karabut, Study of deuterium loading into Pd cathode samples of glow discharge, *Proc. 9th Int. Workshop on Anomalies in Hydrogen/Deuterium Gas Loaded Metals*, 6–11 September 2010, Siena, Italy.

[8] A.B. Karabut, E.A. Karabut and P.L. Hagelstein, Spectral and temporal characteristics of X-ray emission from metal electrodes in a high-current glow discharge, *J. Condensed Matter Nucl. Sci.* **6** (2012) 217.

[9] A.B. Karabut and E.A. Karabut, Research into excited 0.6–6.0 keV energy levels in the cathode solid medium of glow discharge by X-ray spectra emission, *J. Condensed Matter Nucl. Sci.* **8** (2012) 159.

[10] A.B. Karabut, Research into excited long lived 0.6–6.0 keV energy levels in the cathode solid medium of glow discharge by X-ray spectra emission, *J. Materials Sci. Eng. B* **3** (2013) 298.

[11] B.I. Ivlev, X-ray laser pulses from solids, *arXiv preprint* arXiv:1512.08504 (2015).

[12] B.I. Ivlev, Conversion of zero point energy into high-energy photons, *Revista Mexicana de Física* **62** (2016) 83–88.

[13] P.L. Hagelstein, Physics of short-wavelength-laser design, Ph.D. Thesis, MIT, 1981.

[14] P.L. Hagelstein and I.U. Chaudhary. Phonon models for anomalies in condensed matter nuclear science, *Current Sci.* **108** (2015) 507.

[15] P.L. Hagelstein, Directional X-ray and gamma emission in experiments in condensed matter nuclear science, *Current Sci.* **108** (2015) 601.

[16] P.L. Hagelstein, Current status of the theory and modeling effort based on fractionation, *J. Condensed Matter Nucl. Sci.* **19** (2016) 98–109.

[17] I.L. Dillamore and W.T. Roberts, Preferred orientation in wrought and annealed metals, *Metallurgical Rev.* **10** (1965) 271–380.

[18] R. Gotthardt, G. Hoschek, O. Reimold and F. Haessner, Topographic arrangement of crystallite orientations in rolled copper, *Texture* **1** (1972) 99–109.

[19] H. Hu, Texture of metals, *Texture* **1** (1974) 233–258.

[20] Y. Lo, A mathematical theory of antenna arrays with randomly spaced elements, *IEEE Trans. Antennas and Propagation* **12** (1964) 257–268.

[21] V.D. Agrawal and Y.T. Lo, Distribution of sidelobe level in random arrays, *Proc. IEEE* **57** (1969) 1764–1765.
[22] B. Steinberg, The peak sidelobe of the phased array having randomly located elements, *IEEE Trans. Antennas and Propagation* **20** (1972) 129–136.
[23] M. Donvito and S. Kassam, Characterization of the random array peak sidelobe, *IEEE Trans. Antennas and Propagation* **27** (1979) 379–385.
[24] H. Ochiai, P. Mitran, H.V. Poor and V. Tarokh, Collaborative beamforming in ad hoc networks, *Information Theory Workshop* IEEE (2004) 396–401.
[25] N.N. Ma, K. Buchanan, J. Jensen and G. Huff, Distributed beamforming from triangular planar random antenna arrays, *Military Commun. Conf. MILCOM*, IEEE (2015) 553–558.
[26] J.V. Thorn, N.O. Booth and J.C. Lockwood, Random and partially random acoustic arrays, *J. Acoustical Soc. Amer.* **67** (1980) 1277–1286.
[27] W.S. Hodgkiss, Random acoustic arrays, *Underwater Acoustics and Signal Processing*, Springer Netherlands, 1981, pp. 327–338.
[28] K.R. Buchanan, Theory and applications of aperiodic (random) phased arrays, Ph.D. dissertation, Texas A&M University, 2014.
[29] J.D. Jackson, *Classical Electrodynamics*, Wiley, New York, 1975.
[30] A.B. Karabut, X-ray emission in the high current density glow discharge experiments, *Proc. ICCF9* (2002) 155–158.
[31] D.H. Johnson and D.E. Dudgeon, *Array Signal Processing*, Prentice-Hall, Upper Saddle River, NJ, 1993. See Section 3.3.6 on Random Arrays.
[32] J.W. Goodman, Some fundamental properties of speckle, *J. Optical Soc. Amer.* **66** (1976) 1145–1150.
[33] P.L. Hagelstein and I.U. Chaudhary, A model for collimated X-ray emission in the Karabut experiment, *Proc. ICCF17* (2013).
[34] A.A. Kornilovaa, V.I. Vysotskii, N.N. Sysoev, N.K. Litvin, V.I. Tomak and A.A. Barzov, Shock cavitational mechanism of X-ray generation during fast water stream cavitation, *Moscow University Physics Bulletin* **65** (2010) 46.
[35] A.A. Kornilova, V.I. Vysotskii, N. N. Sysoev, N.K. Litvin, V.I. Tomak and A.A. Barzov, Generation of intense X-rays during ejection of a fast water jet from a metal channel to atmosphere, *J. Surface Investigation. X-ray, Synchrotron and Neutron Techniques* **4** (2010)1008.
[36] V.I. Vysotskii, A.A. Kornilova, A.O. Vasilenko and V.I. Tomak, Detection and investigation of undamped temperature waves excited under water jet cavitation, *J. Surface Investigation. X-ray, Synchrotron and Neutron Techniques* **8** (2014) 1186–1192.
[37] V.I. Vysotskii, A.A. Kornilova and A.O. Vasilenko, Observation and investigation of anomalous X-ray and thermal effects of cavitation, *Current Sci.* **108** (2015) 608.
[38] V.I. Vysotskii, private communication.